Table of Contents

1. Executive Summary

LCLS-II-HE at SLAC will be a transformative X-ray tool for the scientific mission of DOE Basic Energy Sciences (BES) and for the nation. It represents the vital next step in the ongoing revolution in X-ray lasers, triggered by the world's first demonstration of a hard X-ray free-electron laser (XFEL) by LCLS in 2009. Its capability moves far beyond the present generation of XFELs and the ultimate potential of storage rings, firmly maintaining the U.S. as the international leader in the science enabled by X-ray sources. The unmatched performance of this facility will serve the needs of a broad scientific user community focused on some of the most critical challenges facing our society, while providing extraordinary potential for scientific discovery and attracting the best and brightest scientific talent.

LCLS-II-HE will provide a qualitatively new capability, unique in the world, delivering ultrafast atomic resolution at high average power. The project is a natural extension to LCLS-II, adding known technology and using existing infrastructure. It will extend operation of the high-repetition-rate beam into the critically important "hard X-ray" regime (>5 keV) that has been used in more than 75% of LCLS experiments to date, providing a major leap in performance to the broadest cross-section of the user community.

The energy reach of LCLS-II-HE (stretching from 5 keV to at least 13 keV and likely up to 20 keV) will enable the study of atomic-scale dynamics with the penetrating power and pulse structure needed for *in situ* and *operando* studies of real-world materials, functioning assemblies, and biological systems.

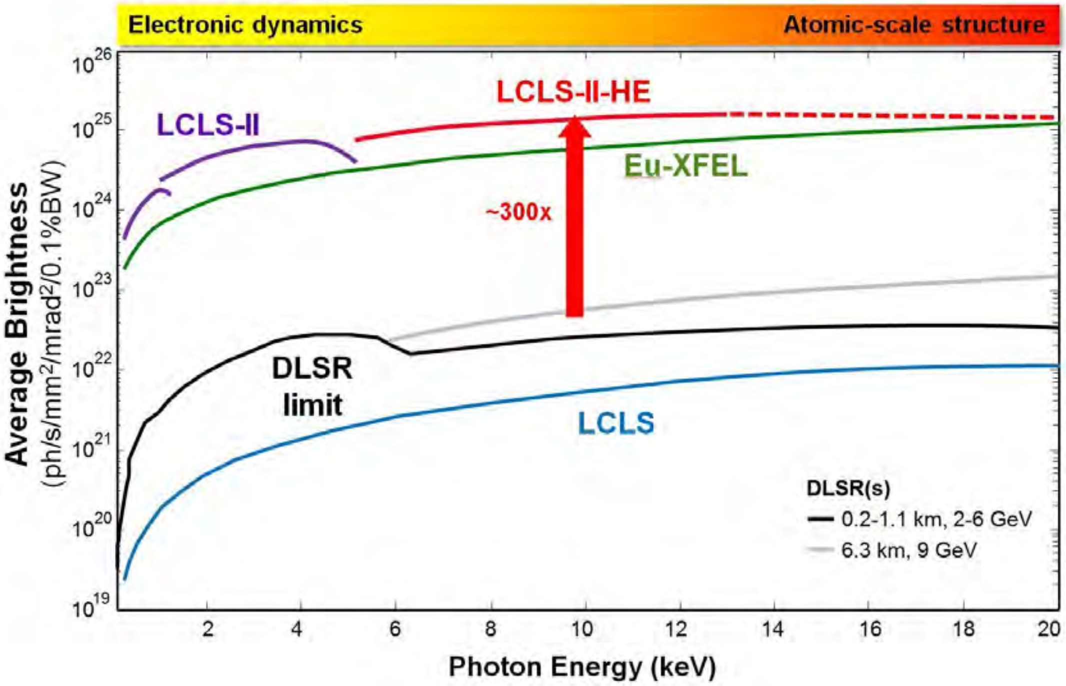

Figure 1.1 The performance of LCLS-II-HE will allow access to the 'hard X-ray' regime, providing atomic resolution capability, with an average brightness roughly 300 times the ultimate capability of a diffraction-limited storage ring (DLSR) [1]. Self-seeding will further increase the average brightness of the XFEL facilities by an additional factor of 20 to 50.

The performance of LCLS-II-HE in comparison to other X-ray sources is shown in Figure 1.1. The facility will:

- Deliver **two to three orders of magnitude increase in average spectral brightness beyond** any proposed or envisioned diffraction-limited storage ring (DLSR), exceeding the anticipated performance of the European-XFEL.
- Provide **temporal coherence** for high-resolution spectroscopy near the Fourier transform limit with more than **300-fold increase in average spectral flux** (ph/s/meV) for high-resolution studies beyond any proposed or envisioned DLSR**.**
- Generate ultrafast hard X-ray pulses in a **uniform (or programmable) time structure** at a repetition rate of up to 1 MHz – a qualitative advance beyond the burst-mode nature of the European-XFEL, and a **100,000-fold improvement in temporal resolution** compared to storage ring sources.
- Combine **three independent accelerators** into a single facility, representing an unprecedented level of flexibility for the user community (a new 8 GeV superconducting linac; a separately tunable 3.6 GeV line for the LCLS-II instruments; and the existing 15 GeV Cu-linac). **No other facility in the world will have this capability.**

The LCLS-II-HE project will add 19 cryomodules of the type already being manufactured for LCLS-II, doubling the electron beam energy from the superconducting accelerator to 8 GeV and making use of the existing cryogenic cooling capacity and space within the linac tunnel.

Therefore, this solution represents a low-risk path with dramatic scientific impact. It will incorporate a linac bypass line to allow simultaneous operation of the soft X-ray and hard X-ray undulator sources with optimum electron beam energies, coupled with myriad beam-sculpting techniques developed on LCLS, including bandwidth control via seeding, multi-pulse operation, and delivery of the 3rd harmonic (opening up new areas of science in the energy range 20 to 50 keV).

This proposal **incorporates all of the elements required for the operating facility**, including accelerator systems, modifications to the instrumentation suite, and all the associated infrastructure. It thus represents a self-contained project, not reliant on subsequent funding of beamlines over an extended period.

The project cost (at $292M in FY17 dollars) includes robust contingency (>30%) and the full project infrastructure and supply chain start-up costs for a stand-alone project. Opportunities for substantial cost savings, risk reduction, and schedule optimization are highlighted in Section 1.3, taking advantage of the ongoing LCLS-II Project supply chain, partnerships, and staff. Furthermore, only a minor (5%) increase to the operations budget is required for this upgraded facility.

The design and implementation path can make use of the annual maintenance periods of the LCLS facility, allowing continuity of scientific exploitation along with flexibility in project scheduling **without any extended downtime**.

1.1 Revolutionary Technical Capabilities of LCLS-II-HE

LCLS-II-HE will lead to significant scientific impact, outlined below, enabled by a suite of unmatched technical attributes:

I. **Access to the energy regime above 5 keV:** This is particularly important because it allows analysis of key chemical elements in addition to providing atomic resolution. For example, this regime encompasses Earth-abundant elements that will be needed for large-scale deployment of photocatalysts for electricity and fuel production; it allows study of strong spin-orbit coupling that underpins many aspects of quantum materials; and it reaches the biologically important selenium K-edge, used for protein crystallography. This is illustrated in Figure 1.2.

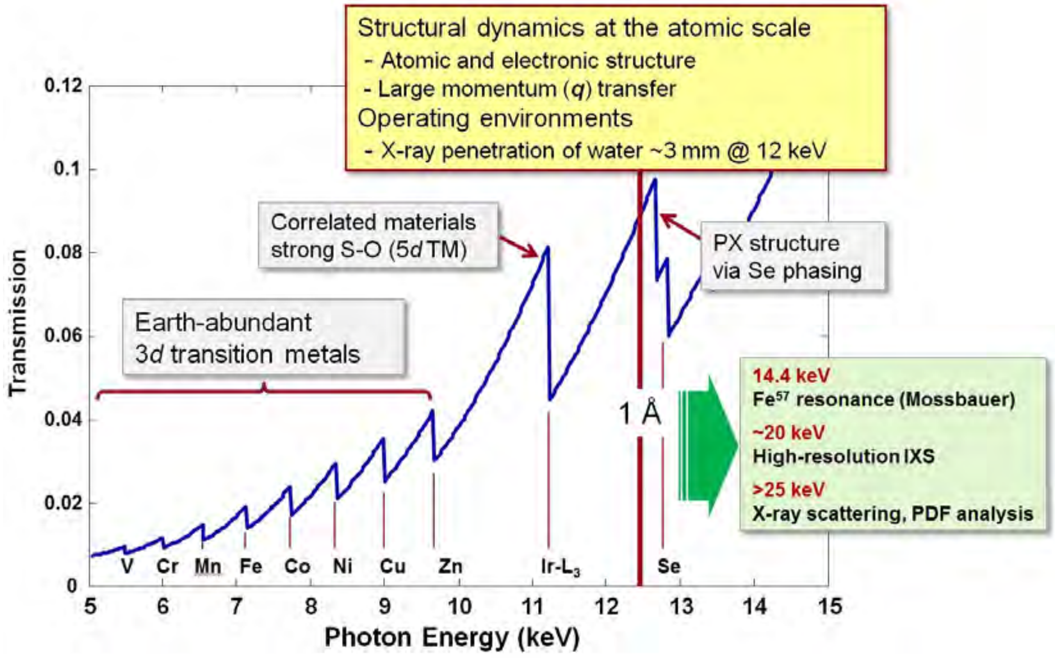

Figure 1.2 The spectral region above 5 keV (the design limit of LCLS-II) is a critical area for many types of measurements. Access to angström wavelength (~12.4 keV) X-rays is a major enabling step for atomic-scale studies, while the ability to probe Earth-abundant elements and access experimental regimes central to biological structure determination and quantum materials studies will provide a fundamentally new capability for discovery science.

II. **High-repetition-rate, ultrafast hard X-rays** from LCLS-II-HE will reveal coupled atomic and electronic dynamics in unprecedented detail. Advanced X-ray techniques will simultaneously measure electronic structure and subtle nuclear displacements at the atomic scale, on fundamental timescales (femtosecond and longer), and in operating environments that require the penetrating capabilities of hard X-rays and the sensitivity provided by high repetition rate.

III. **Temporal resolution:** LCLS-II-HE will deliver coherent X-rays on the fastest timescales, opening up experimental opportunities that were previously unattainable due to low signal-to-noise from LCLS (at 120 Hz) and that are simply not possible on non-laser sources. The typical limit for synchrotron sources is ~100 ps (100,000 fs), whereas the performance of LCLS has progressed from initial pulse durations of 300 fs down to 5 fs, coupled to the capability for double pulses with independent control of energy, bandwidth, and timing. Ongoing development programs offer the potential for 0.5 fs pulses.

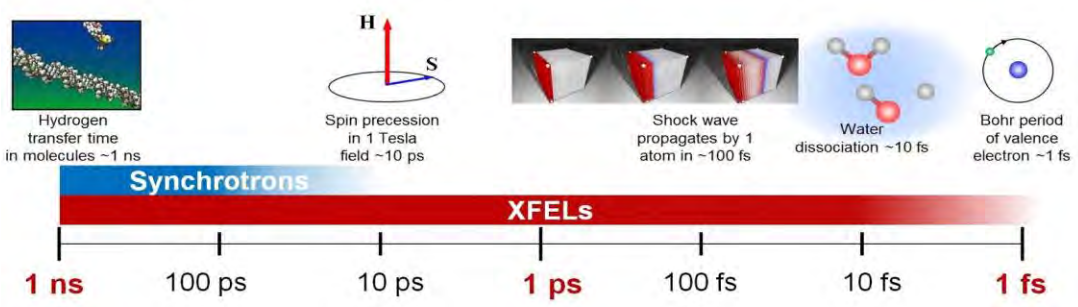

Figure 1.3 A unique feature of X-ray free-electron lasers is the ability to probe the fastest timescales, providing over three orders of magnitude higher temporal resolution than a synchrotron source.

IV. **Temporal coherence**: Control over the XFEL bandwidth will be a major advance for high-resolution inelastic X-ray scattering and spectroscopy in the hard X-ray range (RIXS and IXS). The present scientific impact of RIXS and IXS is substantially limited by the available spectral flux (ph/s/meV) from temporally incoherent synchrotron sources. LCLS-II-HE will provide more than a 300-fold increase in average spectral flux compared to synchrotron sources, opening new areas of science and exploiting high energy resolution and dynamics near the Fourier transform limit.

	Hard X-ray Flux on Sample (photons/second)	
Resolution:	**~100 meV**	**~1 meV**
LCLS-II-HE		**$\sim 10^{13}$**
ESRF	$\sim 10^{13}$ (UPBL6)	$\sim 10^{10}$ (ID28)
SPring-8		$\sim 10^{10}$
APS	$\sim 10^{12}$ (MERIX)	$\sim 10^{10}$
NSLS-II		$\sim 10^{10}$

Table 1.1. Comparison of projected LCLS-II-HE performance for RIXS and IXS, (based on data in reference 2). LCLS-II-HE performance is quoted for a seeded beam -- providing two orders of magnitude improvement in either resolution or in flux at the highest resolution.

V. **Spatial coherence:** The high average coherent power of LCLS-II-HE in the hard X-ray range, with programmable pulses at high repetition rate, will enable studies of spontaneous ground-state fluctuations and heterogeneity at the atomic scale from µs (or longer) down to fundamental femtosecond timescales using powerful time-domain approaches such as X-ray photon correlation spectroscopy (XPCS). LCLS-II-HE capabilities will further provide a qualitative advance for understanding non-equilibrium dynamics and fluctuations via time-domain inelastic X-ray scattering (FT-IXS) and X-ray Fourier-transform spectroscopy approaches using Bragg crystal interferometers.

VI. **Structural dynamics and complete time sequences:** LCLS achieved early success in the determination of high-resolution structures of biological systems and nanoscale matter before the onset of damage. X-ray scattering with ultrashort pulses represents a step-change in the field of protein crystallography. An important scientific challenge is to understand function as determined by structural dynamics – at the atomic scale (requiring ~1Å resolution) and under operating conditions or in physiologically relevant environments (*e.g.* aqueous, room temperature). The potential of dynamic pump-probe structure studies has been demonstrated in model systems, but the much higher repetition rates of LCLS-II-HE are needed in order to extract complete time sequences from biologically relevant complexes. Here, small differential scattering signals that originate from dilute concentrations of active sites and low photolysis levels are essential in order to provide interpretable results.

VII. **Heterogeneous sample ensembles and rare events:** The high repetition rate and uniform time structure of LCLS-II-HE provide a transformational capability to collect 10^8-10^{10} scattering patterns (or spectra) per day with sample replacement between pulses. By exploiting revolutionary advances in data science (*e.g*. Bayesian analysis, pattern recognition, manifold maps, or machine learning algorithms) it will be possible to characterize heterogeneous ensembles of particles or identify and extract new information about rare transient events from comprehensive data sets.

1.2 Scientific Impact

LCLS-II-HE will provide the U.S. with a true "discovery science" facility that leaps far beyond any existing X-ray source, with capabilities that are essential for the science mission of DOE. The development of user facilities within DOE Office of Science is being driven in large part by the urgent need for a deeper understanding of the phenomena underpinning the future of the energy sector, the environment, and biological sciences. New observational tools and facilities are required to address the associated scientific grand challenges, as highlighted in a wide-ranging set of reports from DOE BES [3-7].

In particular, LCLS-II-HE will enable precision measurements of structural dynamics on atomic spatial scales and and fundamental timescales. Such measurements are needed to underpin many of the transformative opportunities identified in the latest report from the Basic Energy Sciences Advisory Committee (BESAC) [3], by providing detailed insight into the behavior of complex matter in real-world heterogeneous samples on fundamental scales of energy, time, and length. The solutions to many important challenges facing humanity, such as developing alternative sources of energy, mitigating environmental and climate problems, developing new "green" technologies, and delivering precision medical tools, depend on an improved understanding and control of matter.

We highlight seven broad classes of science for which LCLS-II-HE will uniquely address critical knowledge gaps that are directly related to DOE BES scientific grand challenges [3, 6], which are indicated in bullets:

Coupled dynamics of energy and charge in atoms and molecules

Flows of energy and charge in molecules are the fundamental processes that drive chemical reactions and store or release energy. They are central to energy processes ranging from combustion to natural and man-made molecular systems that convert sunlight into fuels. Understanding and controlling these processes remains a fundamental science challenge, in large part because the movement of charge is closely coupled to subtle structural changes of the molecule, and conventional chemistry models are inadequate to fully describe this. Sharper experimental tools are needed to probe these processes –

simultaneously at the atomic level and on natural (femtosecond) time scales. LCLS-II-HE will image dynamics at the atomic scale via hard X-ray scattering and coherent diffractive imaging (CDI) to reveal the coupled behavior of electrons and atoms with unprecedented clarity. The combination of hard X-rays with high peak power and high average power will enable new nonlinear spectroscopies that promise important new insights into reactive chemical flows in complex chemical environments such as combustion.

Grand-challenge science areas addressed:

- *Control Matter at the Level of Electrons*
- *Emergent Properties from Complex Electronic and Atomic Correlations*
- *Master Energy and Information on the Nanoscale*

Catalysis, photocatalysis, environmental & coordination chemistry

A deeper understanding of the fundamental processes in catalysis, photocatalysis, and interfacial chemistry is essential for directed design of new systems for chemical transformations, energy storage, and solar energy conversion that are efficient, chemically selective, robust, and based on Earth-abundant elements. LCLS-II-HE will reveal the critical (and often rare) transient events in these multistep processes, from light harvesting to charge separation, migration, and accumulation at catalytically active sites. Time-resolved, high-sensitivity, element-specific scattering and spectroscopy enabled by LCLS-II-HE will provide the first direct view of atomic-scale chemical dynamics at interfaces. The penetrating capability of hard X-rays will probe operating catalytic systems across multiple time and length scales. The unique LCLS-II-HE capability for simultaneous delivery of hard and soft X-ray pulses opens the possibility to follow chemical dynamics (via spectroscopy) concurrent with structural dynamics (substrate scattering) during heterogeneous catalysis. Time-resolved hard X-ray spectroscopy with high fidelity, enabled by LCLS-II-HE, will reveal the fine details of functioning biological catalysts (enzymes) and inform the design of artificial catalysts and networks with targeted functionality.

Grand-challenge science areas addressed:

- *Beyond Ideal Materials and Systems*
- *Mastering Hierarchical Architectures in Matter Beyond Equilibrium*
- *Imaging Matter across Scales*
- *Data, Algorithms and Computing*

Imaging biological function and dynamics

LCLS-II-HE is the ideal, much-desired upgrade to LCLS-II that the structural biology community requires. The combination of high spatial and time resolution with a high repetition rate will make LCLS-II-HE a revolutionary machine for many biological science fields. At high repetition rates, serial femtosecond crystallography (SFX) will advance from successful demonstration experiments to addressing some of the most pressing challenges in structural biology for which only very limited sample volumes are available (e.g. human proteins); or only very small crystal sizes can be achieved (<1 µm); or where current structural information is significantly compromised by damage from conventional X-ray methods (*e.g.* redox effects in metalloproteins). In all of these cases, high throughput and near-physiological conditions of room temperature crystallography will be qualitative advances. X-ray energies spanning the Se K-edge (12.6 keV) will further enable *de novo* phasing via molecular replacement and anomalous scattering. Time-resolved SFX and solution SAXS will advance from present few-time snapshots of model systems at high photolysis levels to full time sequences of molecular dynamics that are most relevant for biology. Hard X-rays and high repetition rates will further enable advanced crystallography methods that exploit diffuse scattering from imperfect crystals, as well as advanced solution scattering and single particle imaging methods to map sample heterogeneity and conformational dynamics in native environments.

Grand-challenge science areas addressed:

- *Imaging Matter across Scales*
- *Characterize & Control Systems away from Equilibrium*
- *Data, Algorithms and Computing*

Materials heterogeneity, fluctuations, and dynamics

Heterogeneity and fluctuations of atoms and charge-carriers – spanning the range from the atomic scale to the mesoscale – underlie the performance and energy efficiency of functional materials and hierarchical devices. Conventional models of ideal materials often break down when trying to describe the properties that arise from these complex, non-equilibrium conditions. Yet, there exists untapped potential to enhance materials performance and create new functionality if we can achieve a much deeper insight into these statistical atomic-scale dynamics. Important examples include: structural dynamics associated with ion transport in materials for energy storage devices and fuel cells; nanostructured materials for manipulating nonequilibrium thermal transport; two-dimensional materials and heterostructures with exotic properties that are strongly influenced by electron-phonon coupling, light-matter interactions, and subtle external stimuli; and perovskite photovoltaics where dynamic structural fluctuations influence power conversion efficiency. LCLS-II-HE will open an entirely new regime for time-domain coherent X-ray scattering of both statistical (*e.g*. XPCS) and triggered (pump-probe) dynamics with high average coherent power and penetrating capability for sensitive real-time, *in situ* probes of atomic-scale structure. This novel class of measurements will lead to new understanding of materials, and, ultimately, device performance, and will couple directly to both theory efforts and next-generation materials design initiatives.

Grand-challenge science areas addressed:

- *Beyond Ideal Materials and Systems*
- *Mastering Hierarchical Architectures in Matter Beyond Equilibrium*
- *Imaging Matter across Scales*

Quantum materials and emergent properties

There is an urgent technological need to understand and ultimately control the exotic quantum-based properties of new materials – ranging from superconductivity to ferroelectricity to magnetism. These properties emerge from the correlated interactions of the constituent matter components of charge, spin, and phonons, and are not well described by conventional band models that underpin present semiconductor technologies. A comprehensive description of the ground-state collective modes that appear at modest energies, 1-100 meV, where modern X-ray sources and spectrometers lack the required combination of photon flux and energy resolution, is critical to understanding quantum materials. High-resolution hard X-ray scattering and spectroscopy at close to the Fourier limit will provide important new insights into the collective modes in 5*d* transition metal oxides – where entirely new phenomena are now being discovered, owing to the combination of strong spin-orbit coupling and strong charge correlation. The ability to apply transient fields and forces (optical, THz, magnetic, pressure) with the time-structure of LCLS-II-HE will be a powerful approach for teasing apart intertwined ordering, and will be a step toward materials control that exploits coherent light-matter interaction. Deeper insight into the coupled electronic and atomic structure in quantum materials will be achieved via simultaneous atomic-resolution scattering and bulk-sensitive photoemission enabled by LCLS-II-HE hard X-rays and high repetition rate.

Grand-challenge science areas addressed:

- *Emergent Properties from Complex Electronic and Atomic Correlations*
- *Harnessing Coherence in Light and Matter*

Materials in extreme environments

LCLS-II-HE studies of extreme materials will be important for fusion and fission materials applications and could lead to important insights into planetary physics and geoscience. The unique combination of capabilities from LCLS-II-HE will enable high-resolution spectroscopic and structural characterization of matter in extreme states that is far beyond what is achievable today. High peak brightness combined with high repetition rates and high X-ray energies are required to: (i) penetrate dynamically heated dense targets and diamond anvil cells (DAC), (ii) achieve high signal-to-noise data above the self-emission bremsstrahlung background, (iii) probe large momentum transfers on atomic scales to reveal structure and material phases, and (iv) measure inelastic X-ray scattering with sufficient energy resolution and sensitivity to determine the physical properties of materials.

Grand-challenge science areas addressed:

- *Characterize & Control Systems away from Equilibrium*
- *Beyond Ideal Materials and Systems*

Nonlinear X-ray matter interactions

A few seminal experiments on the first generation of X-ray free-electron lasers, LCLS and SACLA, have demonstrated new fundamental nonlinear hard X-ray-matter interactions, including phase-matched sum frequency generation, second harmonic generation, and two-photon Compton scattering. While nonlinear X-ray optics is still in the discovery-based science phase, advances in our understanding of these fundamental interactions will lead to powerful new tools for atomic and molecular physics, chemistry, materials science, and biology via measurement of valence charge density at atomic resolution and on the attosecond-to-femtosecond timescale of electron motion. The combination of high repetition rate and high peak intensity pulses from LCLS-II-HE will enable high-sensitivity measurements that exploit subtle nonlinear effects. This will transform the nonlinear X-ray optics field from demonstration experiments to real measurements that utilize the nonlinear interactions of “photon-in, photon-out” to simultaneously access transient spectroscopic and structural information from real materials.

Grand-challenge science areas addressed:

- *Control Matter at the Level of Electrons*
- *Emergent Properties from Complex Electronic and Atomic Correlations*

References

1. DLSR contributions from M. Borland (APS) and C. Steier (ALS)
2. A. Q. R. Baron, "High-Resolution Inelastic X-Ray Scattering II: Scattering Theory, Harmonic Phonons, and Calculations," in *Synchrotron Light Sources and Free-Electron Lasers: Accelerator Physics, Instrumentation and Science Applications*, E. Jaeschke, S. Khan, J. R. Schneider, and J. B. Hastings, eds. (Springer International Publishing, Cham, 2014), pp. 1.
3. J. C. Hemminger, "Challenges at the Frontiers of Matter and Energy: Transformative Opportunities for Discovery Science - BESAC Report U.S. D.O.E.," (http://science.energy.gov/~/media/bes/besac/pdf/Reports/CFME_rpt_print.pdf, 2015).

4. J. Hemminger, G. Crabtree, and M. Kastner, "New Science for a Secure and Sustainable Energy Future - BESAC Report U.S. D.O.E.," (http://science.energy.gov/~/media/bes/pdf/reports/files/nsssef_rpt.pdf, 2008).
5. W. Eberhardt, and F. Himpsel, "Next-Generation Photon Sources for Grand Challenges in Science and Energy - BESAC Report U.S. D.O.E.," (http://science.energy.gov/~/media/bes/pdf/reports/files/ngps_rpt.pdf, 2008).
6. G. Fleming, and M. Ratner, "Directing Matter and Energy: Five Challenges for Science and the Imagination - BESAC Report U.S. D.O.E.," (http://science.energy.gov/bes/news-and-resources/reports/abstracts/#GC, 2007).
7. Report of the BESAC Subcommittee on Future X-ray Light Sources (2013) http://science.energy.gov/~/media/bes/besac/pdf/Reports/Future_Light_Sources_report_BESAC_approved_72513.pdf
8. BESAC Report on Facility Upgrades (2016) http://science.energy.gov/~/media/bes/besac/pdf/Reports/BESAC_Facility_Upgrade_Assessment_Approved_June_9_2016.pdf

2. Background, Science Needs & Capability Gap

A new scientific frontier opened in 2009 when the world's first X-ray free-electron laser (XFEL), the LCLS, began operations at SLAC National Accelerator Laboratory. Initial research relied on the Atomic, Molecular and Optical Science (AMO) end station, followed by a suite of six additional instruments developed over the first few years of operation. The scientific start of LCLS has arguably been one of the most vigorous and successful of any new research facility.

The major scientific accomplishments of LCLS within the first few years of operation are reflected in both the number of total publications (729 papers to date associated with LCLS) and the number of publications in high-impact journals (150 to date, including 28 in *Nature* or *Science*). There have been 328 full-scale user experiments using LCLS (2009-2015), plus 139 in-house and crystal-screening experiments. As such, the scientific productivity of the facility is incredibly high. The scientific output and impact of LCLS during the first five years are summarized in a recently published overview in *Reviews of Modern Physics* [1].

Alongside this, there have been significant efforts to increase the number of experiments performed per year, and to increase the number of users at the facility. Progress to date is shown in Figure 2.1. This has been achieved while reducing the cost of experimental delivery over the past year (to allow a greater fraction of DOE funding to be used to develop the technical capability and robustness of LCLS).

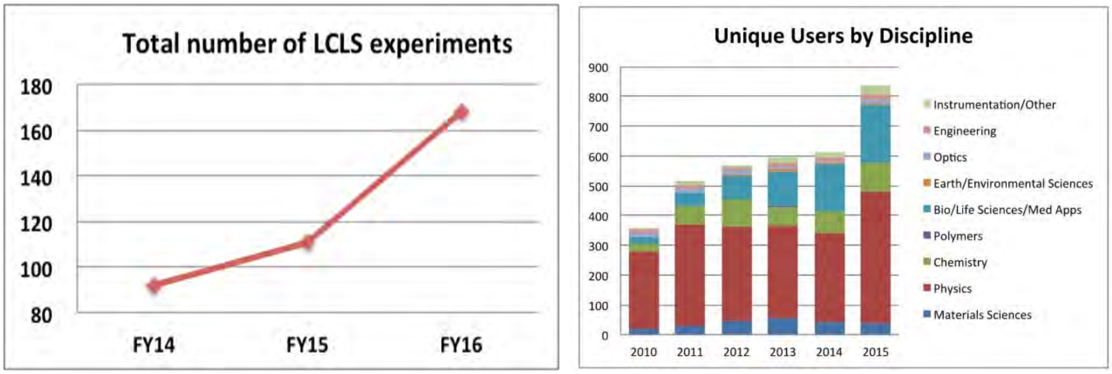

Figure 2.1. The number of experiments and users at LCLS has increased significantly.

LCLS has enabled scientists to study structure and dynamics of matter at atomic size and time scales, taking advantage of the factor 10^9 increase in peak brightness compared to other X-ray sources. The following very brief examples illustrate some of the key early results from LCLS.

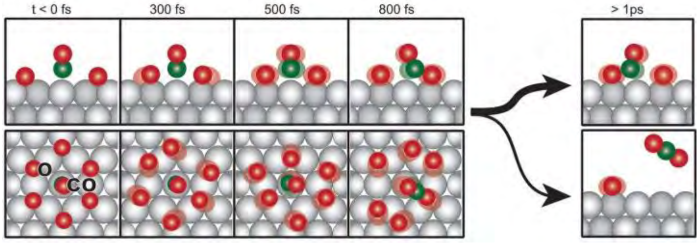

Figure 2.2. Reaction sequence for catalytic Co oxidation on Ru surface [2].

Surface science and catalysis are key to many aspects of life and the economy. LCLS was used to observe sub-picosecond dynamics of catalytic bond formation (Figure 2.2), showing the transient evolution of electronic states over tens of femtoseconds [2].

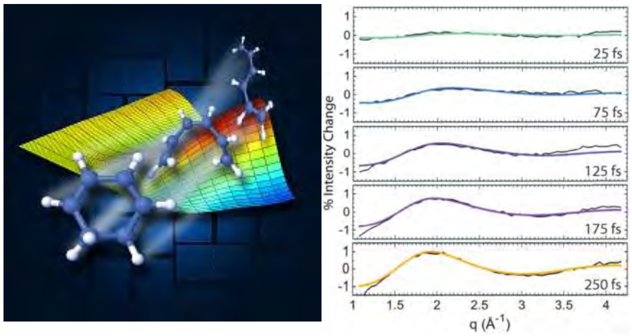

Figure 2.3. Femtosecond electrocyclic ring opening (illustration) and transient X-ray scattering data [3].

In the **chemical sciences**, numerous research groups have used the ultrashort high-brightness LCLS pulses to create various forms of "molecular movies." For example, recent data, featured on the cover of *Physical Review Letters*, measured the opening of molecular rings in the gas phase (Figure 2.3) and their subsequent relaxation to a final conformation with 25 fs resolution [3].

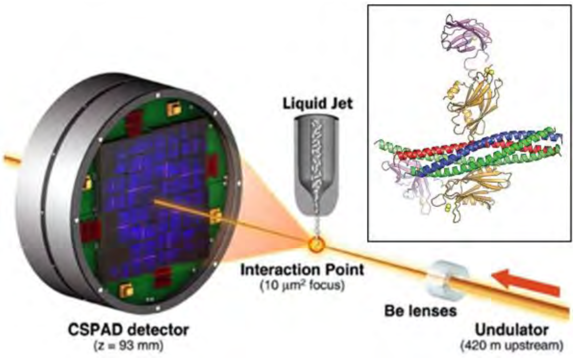

Figure 2.4. LCLS serial crystallography and model of the interface between synaptotagmin-1 and neuronal SNARE complex [4].

In **structural biology**, serial femtosecond crystallography at the LCLS has revolutionized our ability to determine structures of macromolecules that are beyond the reach of synchrotron sources, and has improved the spatial resolution that can be obtained from conventional samples. Furthermore, the dynamics of conformational changes that define how these molecular machines work in living systems can now be probed with sub-picosecond precision. For example, the mechanism for calcium-triggered signaling at neuronal synapses was revealed (Figure 2.4), which could be relevant for a wide range of neurological disorders [4].

Condensed matter physics has benefited immensely from the high brightness and temporal resolution of the LCLS, particularly in unconventional superconductors [5] and magnetic systems [6], where there is a need to understand complex interactions in materials with strong coupling between various quantum degrees of freedom. For example, an important new approach to probing low-energy collective modes in condensed matter was developed using the ultrashort pulses of LCLS to demonstrate Fourier transform inelastic X-ray scattering (FT-IXS), a time-domain probe of the dynamic structure factor in the nonequilibrium regime. Initial experiments yielded new insight into time- and momentum- dependent phonon-phonon correlations in model bulk materials [7]. The high repetition rate of LCLS-II-HE will enable this powerful approach to be applied to functional materials, nanostructures, and assemblies.

While LCLS has delivered unprecedented peak brightness, the average brightness is modest, similar to that of a synchrotron source (Figures 1.1 and 2.5). Furthermore, many experiments require attenuation of the peak intensity in order to avoid perturbation of the sample by the X-ray probe. In these cases, signal accumulation times often become prohibitive at 120 Hz, thus rendering many experiments impractical. While LCLS-II will address this issue at photon energies below 5 keV, LCLS-II-HE will be required to mitigate this issue above 5 keV, the hard X-ray regime where over 75% of LCLS users operate at present.

The early success of LCLS and future potential of XFEL sources have triggered intense development of XFEL capabilities around the world; up to 16 laser sources in six facilities will soon be operational. Chief among these is the European XFEL, scheduled to perform its first experiments in 2017. It will exploit pulsed superconducting accelerator technology (pulsed-SCRF) to deliver an average brightness that will exceed the performance of LCLS at 1 Å by more than 1,000-fold, a capability gap with profound implications for science. Elsewhere in the world, other machines similar in scope to LCLS are appearing in the 2017-18 timeframe (*e.g.* SwissFEL in Switzerland) to complement the dual undulator XFEL facility presently operating in Japan (SACLA), and the PAL XFEL in Korea, which recently reported first lasing operation.

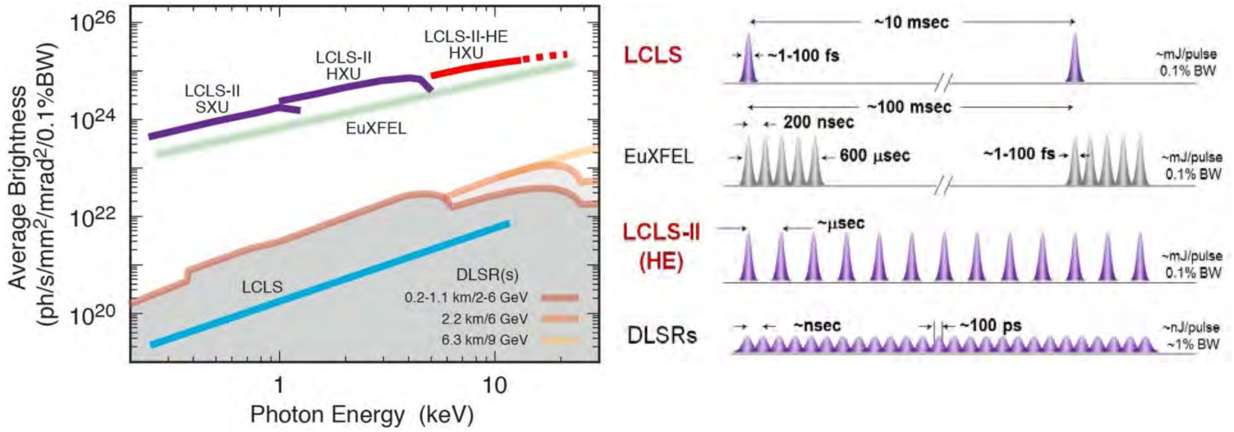

Figure 2.5. Left: Average spectral brightness of current, planned, and potential future X-ray science facilities including diffraction-limited storage rings (DLSRs) [8] and the European XFEL. LCLS-II-HE (dashed line) provides ~1,000-fold increase in average brightness in the fundamental to >12.8 keV. All XFEL curves assume SASE operation. Self-seeding will increase the average brightness of XFELs by an additional factor of 20 to 50, and operation at the 3rd harmonic will push the useful spectral range beyond 30 keV [8]. Right: Pulse structure from LCLS warm Cu-linac at 120 Hz, burst-mode structure from the pulsed SCRF linac of the European XFEL at 5 MHz/10Hz, and the uniform (programmable) bunch structure from the CW-SCRF linac of LCLS-II-HE.

Figure 2.5 shows the average brightness of the extended LCLS facility along with curves characteristic of the limit of high-brightness storage ring sources. Over the spectral range of 0.2 to 5 keV, the average brightness of LCLS-II will be roughly 1,000 times higher than LCLS. LCLS-II-HE will extend this spectral range in the fundamental to at least 12.8 keV (and eventually up to 20 keV), and will reach beyond 30 keV at the 3rd harmonic (with brightness ~1% of the fundamental). LCLS-II-HE will also support self-seeding operation up to ~10 keV (using present-day designs) to further increase the spectral brightness (ph/s/meV) by a factor of 20 to 50.

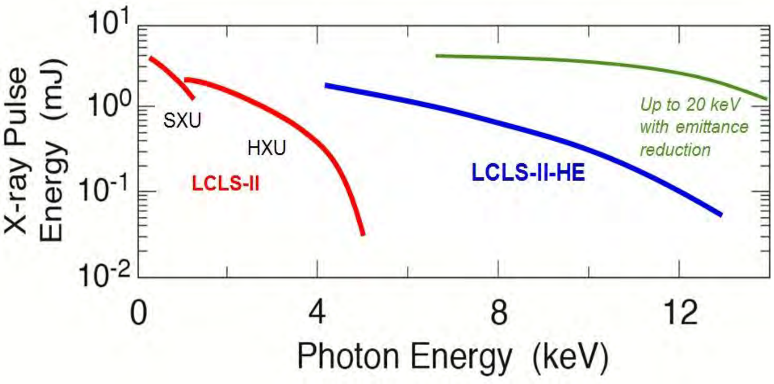

Figure 2.6. Calculated energy per pulse for high-repetition-rate operation from LCLS-II soft X-ray (SXU) and hard X-ray undulator (HXU) at 4 GeV, and proposed LCLS-II-HE (8 GeV). LCLS-II-HE performance is bounded by the blue and green lines, dependent on electron beam emittance (with the resultant highest photon energy being between 12.8 and 20 keV).

LCLS-II-HE will be a transformative X-ray tool that more than bridges the gap between LCLS and the European XFEL, and moves far beyond the other facilities in the world. It will add 19 additional cryomodules to the CW-SCRF linac of LCLS-II to provide hard X-rays (<1Å) at high repetition rates that are essential to reveal structural dynamics on the atomic scale.

XFEL Facility	Number of Undulator Sources	X-ray Energy Range	Repetition Rate	Linac	Status
LCLS-I (U.S.)	1	0.25 to 12.8 keV	120 Hz	warm Cu 15 GeV	operational
LCLS-II (U.S.)	2	0.25 to 5 keV (0.25 to 25 keV)	up to 1 MHz (120 Hz)	CW-SCRF 4 GeV	2020 planned
LCLS-II-HE (U.S.)	2	0.25 to 12.8–20 keV	up to 1 MHz	CW-SCRF 8 GeV	proposed
SACLA (Japan)	2 (3)	5 to 20 keV	60 Hz	warm Cu 8 GeV	operational
PAL-FEL (Republic of Korea)	2	0.3 to 20 keV	60 Hz	warm Cu 10 GeV	2016 first light
Swiss-FEL (Switzerland)	2	0.2 to 12 keV	100 Hz	warm Cu 5.8 GeV	2017 planned
European XFEL (EU / Russia, sited in Germany)	3 (5)	0.2 to 25 keV	28 kHz (effective) in 10 Hz bursts	Pulsed-SCRF 17.5 GeV	2017 planned
FLASH **FLASH-II** (Germany)	2	0.03 to 0.3 keV	5 kHz (effective) in 10 Hz bursts	Pulsed-SCRF 1.2 GeV	operational
FERMI (Italy)	2	0.01 to 0.3 keV	50 Hz	warm Cu 1.5 GeV	operational

Table 2.1. XFEL facilities and capabilities [1]. The number of undulator sources is quoted in terms of initial operation (and in brackets, the achievable number using the installed infrastructure). The proposed upgrade path of the LCLS facility is broken out in the first three rows for clarity, with the performance of the two shaded rows being simultaneously available after LCLS-II-HE is completed. Glossary: CW-SCRF= continuous superconducting RF accelerator, Pulsed-SCRF= pulsed superconducting RF accelerator.

References

1. C. Bostedt*, et al.*, "Linac Coherent Light Source: The first five years", *Reviews of Modern Physics,* **88**, 015007 (2016).
2. H. Öström*, et al.*, "Probing the transition state region in catalytic CO oxidation on Ru", *Science,* **347**, 978 (2015).
3. M. P. Minitti*, et al.*, "Imaging Molecular Motion: Femtosecond X-Ray Scattering of an Electrocyclic Chemical Reaction", *Phys. Rev. Lett.,* **114**, 255501 (2015).
4. Q. J. Zhou*, et al.*, "Architecture of the synaptotagmin-SNARE machinery for neuronal exocytosis", *Nature,* **525**, 62 (2015).
5. S. Gerber*, et al.*, "Three-dimensional charge density wave order in $YBa_2Cu_3O_{6.67}$ at high magnetic fields", *Science,* **350**, 949 (2015).
6. C. E. Graves*, et al.*, "Nanoscale spin reversal by non-local angular momentum transfer following ultrafast laser excitation in ferrimagnetic GdFeCo", *Nat Mater,* **12**, 293 (2013).
7. M. Trigo*, et al.*, "Fourier-transform inelastic X-ray scattering from time- and momentum-dependent phonon-phonon correlations", *Nat Phys,* **9**, 790 (2013).
8. DLSR contributions from M. Borland (APS) and C. Steier (ALS)

3. Revolutionary New Scientific Capabilities

The technical capabilities of LCLS-II-HE will enable new experimental approaches in the hard X-ray range that are qualitatively different from anything available from current sources, or from any other X-ray source in the foreseeable future. Following is a brief introduction to these new scientific methods and tools, and their anticipated impact. Section 4 presents examples of the science opportunities that will exploit these new measurement methods and the capabilities of LCLS-II-HE.

3.1 Coupled atomic and electronic structure of real systems on fundamental time and length scales

High-repetition-rate, ultrafast hard X-rays from LCLS-II-HE will enable advanced X-ray techniques that simultaneously measure electronic structure and subtle nuclear displacements at the atomic scale, on fundamental timescales (femtoseconds and longer), and in operating environments that require the penetrating capabilities of hard X-rays. The power of this approach has been demonstrated in recent experiments at LCLS, in which hard X-ray scattering and X-ray emission from a model transition-metal charge-transfer complex in solution have been measured simultaneously. These experiments revealed the coupling of charge dynamics and atomic structure on the sub-Å scale and on the 100 fs timescale for the first time.[1]

Applying these techniques to much more complex assemblies (*e.g.* light-harvesting and photosynthetic complexes) will require a much higher repetition rate to extract quantitative information that can be used to inform design and synthesis. For example, studies to date at 120 Hz have been limited to relatively simple molecules in high concentrations with high photolysis yields, whereas functioning assemblies typically have low concentrations of active sites and must be investigated at low photolysis levels to properly understand how they operate.

LCLS-II-HE will enable element-specific probing of the fine details of the chemical structure, such as valence excited-state charge dynamics, by exploiting sensitive valence-to-core ($K_{\beta2,5}$) X-ray emission spectroscopy (XES) and resonant inelastic X-ray scattering (RIXS) in the 5-12 keV range, as illustrated in Figure 3.1. Time-resolved XFEL studies to date have been limited by the average spectral flux (ph/s/meV) to less informative X-ray emission lines (K_{α}, $K_{\beta1,3}$), and to RIXS probing at single time snapshots of large chemical changes in simple molecules at high concentration [2, 3].

LCLS-II-HE will provide a similarly dramatic advance for powerful differential extended X-ray absorption fine structure (EXAFS) studies of changes in local structure at the 0.01 Å scale. The 5-12 keV range spans the core resonances of the Earth-abundant 3*d* transition metals (*e.g.* Fe and Cu K-edges at 7.1 and 9 keV) that are the basis for many biological enzymes and photocatalysts, and the 4*d* and 5*d* metals (*e.g.* Pt L_3-edge at 11.6 keV) commonly used in man-made catalysts and photosynthetic assemblies.

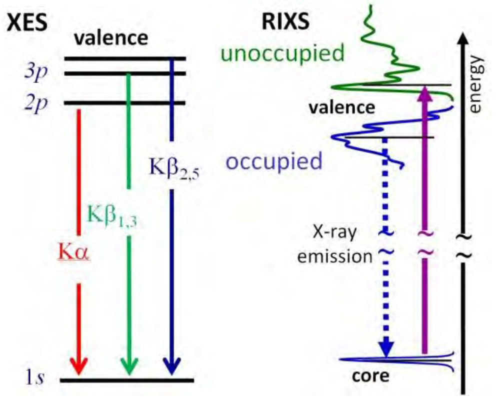

Figure 3.1. Left: X-ray emission spectroscopy (XES). Right: Resonant inelastic X-ray scattering (RIXS).

3.2 Temporal coherence: Dynamics, and high-resolution X-ray spectroscopy at the Fourier limit

The >300-fold increase in average spectral flux (ph/s/meV) via self-seeding will be a major advance for high-resolution inelastic X-ray scattering and spectroscopy in the hard X-ray range (both resonant, RIXS, and non-resonant, IXS), where the available spectral flux from temporally incoherent sources substantially limits the scientific impact. LCLS-II-HE will support novel instrumentation designs for ultra-high-resolution (sub-meV) IXS [4, 5] (Figure 3.2 right), will enable the use of quartz- and sapphire-based analyzers for hard X-ray RIXS at the few meV scale [6], and will make possible entirely new approaches for time-resolved resonant inelastic scattering.

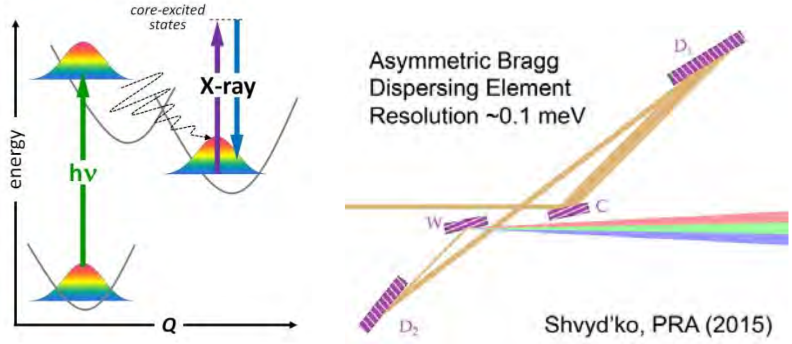

Shvyd'ko, PRA (2015)

Figure 3.2. Element-specific excited-state RIXS (left) and example of high-resolution spectrograph design (right) [4].

For example, element-specific mapping of the excited-state potential energy surfaces of reactive molecular complexes (Figure 3.2 left) will provide entirely new scientific insight for chemistry, materials science, and biology. Time-resolved RIXS is the X-ray analog of powerful femtosecond visible Raman spectroscopy [7], with tunable ultrafast X-rays providing element specificity [8, 9] along with dynamics. LCLS-II-HE capabilities, combined with advanced spectrometer designs [6, 10, 11], will enable this approach to be applied to complex reactive systems for the first time. Of particular interest is the opportunity to distinguish local bonding environments of complex molecular assemblies targeting the metal-ligand fingerprint region (200-500 cm^{-1}, 24-60 meV). This requires high average spectral flux to distinguish weak signals, with <10 meV resolution at close to the Fourier transform limit at photon energies resonant with transition-metal K–edges and L-edges (up to 12 keV) [6].

Inelastic X-ray scattering also has tremendous potential for characterizing ground-state and low-energy collective modes that are hallmarks of complex matter. For example, in strongly correlated materials, collective modes of the electronic continuum determine the material properties and are described by the momentum-dependent dynamic structure factor $S_e(\boldsymbol{q},\omega)\sim\chi(\boldsymbol{q},\omega)$. However, comprehensive direct measurements of this fundamental description of quantum matter at meV energy resolution that spans the entire Brillouin zone have remained largely inaccessible. In soft matter and biological systems, low-energy collective dynamics mediate self-assembly and the development of non-equilibrium forms of matter. Our ability to understand and ultimately control such processes relies on developing much deeper insight into the low-energy potential landscape.

The full scientific potential of inelastic X-ray scattering (both resonant and non-resonant) has yet to be realized, owing to the low average spectral flux of present hard X-ray sources. The high spectral flux from LCLS-II-HE, at close to the transform limit and in a uniform pulse structure to facilitate sample replacement/recovery, will transform this field (see Section 5.1 for a comparison of LCLS-II-HE capabilities in this area with those of existing facilities). Importantly, the hard X-ray regime provides bulk sensitivity and access to sub-nm length scales (large momentum transfer), and is compatible with diamond anvil cells for pressure-dependent studies. LCLS-II-HE capabilities will support the highest-resolution spectrometer designs [4] with unprecedented throughput.

3.3 Coherent hard X-ray scattering: Materials heterogeneity and spontaneous fluctuations

Spontaneous fluctuations and heterogeneity are pervasive in complex matter, and are often central to their functional properties. X-ray photon correlation spectroscopy (XPCS) is a powerful time-domain approach for characterizing ground-state fluctuations and heterogeneity, as illustrated in Figure 3.3. The coherent X-ray analogue of dynamic light scattering, XPCS produces a speckle pattern that is a Fourier projection of the material structure. Changes in the speckle pattern map the evolving material structure in momentum space ($\boldsymbol{q}$) through the dynamic structure factor $S(\boldsymbol{q},t)$. At a fundamental level, the ability to discern structural changes at short time intervals scales inversely with the square of the X-ray source brightness ($\Delta t \sim B^{-2}$). At a practical level, accessing these timescales depends on multiple-pulse measurement schemes (with moderate peak brightness and high average brightness) and/or detector speed and sensitivity. The high average coherent power of LCLS-II-HE, with programmable pulses at high repetition rate, will enable studies of spontaneous fluctuations at the atomic scale from µs (or longer) down to fundamental femtosecond timescales, thus opening up whole new areas of science.

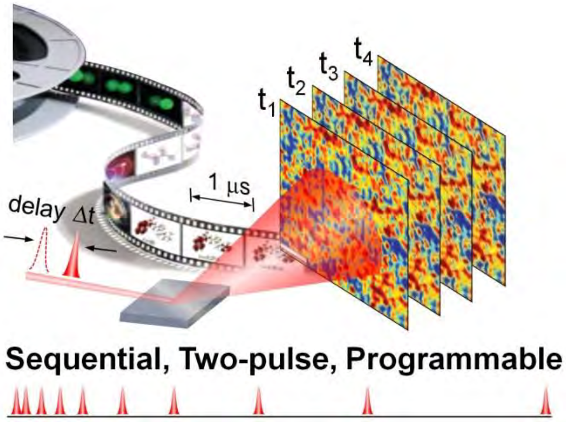

Figure 3.3. Multi-pulse X-ray photon correlation spectroscopy of materials heterogeneity and fluctuations.

XPCS approaches at LCLS-II-HE include the following:

- "Sequential" XPCS measures a real-time sequence of individual speckle patterns, limited either by the repetition rate of the XFEL or by the 2D detector readout rate (see Section 5.5.3. and recent advances in time-stamping detectors [12]).
- "Two-pulse" XPCS [13, 14] relies on superimposed pairs of speckle patterns created by time-delayed X-ray pulses. The decay in speckle visibility as a function of pulse delay is directly related to $S(\boldsymbol{q},t)$. This approach will probe ultrafast atomic-scale statistical dynamics in materials for the first time, with a time resolution limited only by the X-ray pulse delay.
- A "programmable" XPCS mode is uniquely enabled by the CW-SCRF linac of LCLS-II-HE. In the simplest configuration, X-ray pulse pairs can be generated directly from the XFEL with time delays of <100 fs up to milliseconds or longer. In addition, potentially much more powerful XPCS schemes are enabled, in which the entire time structure is encoded in the X-ray pulse sequence (*e.g.* in a logarithmic distribution of time intervals).

LCLS-II-HE capabilities will enable qualitative advances in emerging approaches such as time-domain inelastic X-ray scattering [15] and X-ray Fourier-transform spectroscopy using Bragg crystal interferometers [16], which are potentially powerful complements to IXS and XPCS. For example, FT-IXS is an important new approach for probing low-energy collective modes in condensed matter that exploits the information content of diffuse scattering and the ultrashort pulses of LCLS to map the dynamic structure factor in the non-equilibrium regime. Initial LCLS experiments using FT-IXS yielded new insight into time- and momentum- dependent phonon-phonon correlations in model bulk materials [15] (Figure 3.4). The high repetition rate of LCLS-II-HE will enable this powerful approach to be applied to functional materials, nanostructures, and assemblies.

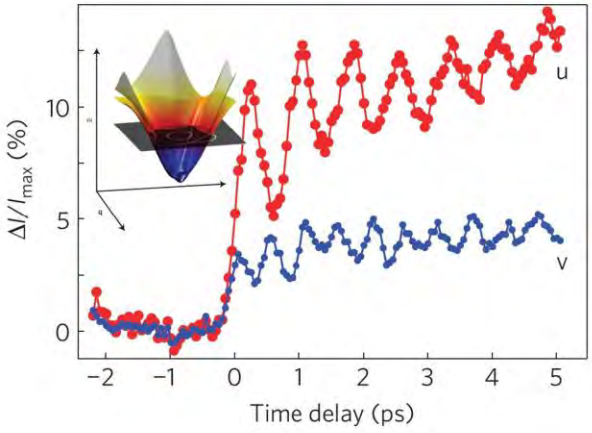

Figure 3.4. Coherent phonon-phonon correlations and acoustic phonon dispersion function (inset) measured in bulk Ge via Fourier-transform inelastic X-ray scattering (FT-IXS) [15].

3.4 Coherent X-ray scattering: Complete time sequences of structural dynamics at the atomic scale

A major early success of LCLS is the determination of high-resolution structures of biological systems and nanoscale matter before the onset of damage. The combination of serial femtosecond crystallography (SFX) and "diffraction before destruction" [17] has provided atomic-resolution structures of clusters, nanomaterials, and many biologically important classes of molecules [18], often from micro- to nano-sized crystals that are unsuitable for study with the best conventional synchrotron X-ray sources, and with higher resolution or with structural details more representative of the room-temperature native state. However, studies to date have been limited largely to a few snapshots of static structures.

An important scientific challenge for structural biology and the broader area of functional nanomaterials and self-assembly is the ability to study structural *dynamics* – at the atomic scale, and under operating conditions or in environments that are more physiologically relevant (*e.g.* aqueous, room temperature). Dynamics is an important key to understanding the function of macromolecular complexes and nanomachines whose structures change over a range of time and length scales, often in response to changes in local environment (temperature, pH) or interaction with small molecules. Determining the conformational states of molecular machines and the low-energy landscape that determines their function are important new frontiers for both biology and nanomaterial self-assembly.

Recent LCLS time-resolved SFX studies of photo-detachment dynamics in CO-myoglobin [19] and isomerization dynamics in photoactive yellow protein [20] illustrate the potential of dynamic pump-probe structure studies. However, these results are limited to just a few time snapshots of model systems at high concentration and at very high excitation fluences. Hard X-rays at much higher repetition rate are needed in order to extract complete time sequences from small differential scattering signals that originate from more relevant complexes, where active sites are often in dilute concentrations and where low photolysis levels are essential in order to provide interpretable results.

While crystallography is an extremely powerful tool for elucidating atomic structures, many complex biological machines defy crystallization due to weak interactions among constituent components and their intrinsic flexibility. Time-resolved solution X-ray scattering [21], fluctuation X-ray scattering (fSAXS), and single particle imaging (SPI) [17, 22, 23] can provide alternative paths toward understanding dynamics of non-crystalline samples at low to medium resolution. SPI continues to evolve toward higher resolution along the paths defined in the LCLS SPI roadmap [24]. Fluctuation X-ray scattering [25-28] is a multi-particle scattering approach based on a limited ensemble of particles that is enabled by the combination of ultrafast X-ray pulses and high repetition rate. It potentially provides ~100 times more information than conventional SAXS – sufficient for 3D reconstruction. It has emerged as a method bridging SPI and crystallography, and is potentially powerful for understanding material dynamics and protein interactions in native environments.

3.5 High repetition rate, heterogeneous sample ensembles, and rare events

The high repetition rate and uniform time structure of LCLS-II-HE provides a transformational capability to collect 10^8-10^{10} scattering patterns (or spectra) per day with sample replacement between pulses. By exploiting revolutionary advances in data science (*e.g.* Bayesian analysis, pattern recognition, manifold maps, and machine learning algorithms as outlined below) it should be possible to characterize heterogeneous ensembles of particles or extract new information about rare transient events from comprehensive data sets of X-ray scattering patterns and/or spectra.

For fluctuation X-ray scattering and single particle imaging, high-intensity pulses in the 5-10 keV range hold tremendous promise for characterizing conformational heterogeneity or biological machines at different stages in their work cycle. For example, recent cryo-EM studies of the ribosome have demonstrated that it is possible to extract conformational movies from a sufficient number of snapshots of non-identical, unoriented biomolecules cryo-trapped at random points in their work cycle [29]. This approach of inferring a movie from static snapshots is directly applicable to XFEL studies, with the significance and impact determined by how finely the conformations are sampled with respect to the underlying conformational heterogeneity (*i.e.* a large number of snapshots are required). Among the hybrid approaches that are increasingly important for biology, the key advantages provided by XFELs include access to dynamics in near-native environments (room temperature, liquid); the ability to probe thick samples or dense media; and an unprecedented number of independent snapshots provided by high repetition rate.

3.6 Advanced computation, data science, and synergy with LCLS-II-HE

Dramatic advances in computational capability and advanced algorithms, coupled with massive data sets, are creating profound opportunities for *data science*, *i.e.* for scientific extraction of new knowledge and insight from data that goes far beyond what was previously possible. This is not simply doing the same analysis faster or on a larger scale, but spawning entirely new methods and establishing new paradigms for analysis. Advanced computation and data science will be integral to LCLS-II-HE, and high-repetition-rate X-ray pulses and massive data sets will further fuel advances in new algorithms and computational approaches. This powerful combination will allow scientists to envision entirely new experiments and analysis methods that will accelerate many fields. Here we highlight just three of many classes of computational techniques that LCLS-II-HE will enable and exploit.

3.6.1 Mapping reaction landscapes and kinetic relationships between conformations

A sufficiently fine-grained statistical sampling of configurational space can be used to map the kinetic topology or reaction pathways of a dynamic system. By analogy, measurement of the GPS locations of an ensemble of cars every minute as they randomly traverse the interstate highway system will provide a good representation of the metropolitan layout of the United States – where cities are and how they are connected. GPS measurements at much less frequent intervals (*e.g.* every day) would not provide the same insight. Similarly, the high repetition rate of LCLS-II-HE will enable the mapping of the configurational space of complex systems such as proteins, viruses, or chemical reactions. For instance, extensive sampling will enable researchers to determine the energy landscape of a protein (*i.e.* the local potential energy minima and the connecting transition states) by analyzing the mutual information content between proximate samples. Because protein systems are high dimensional, consisting of many thousands of atoms (each with multiple degrees of freedom), it will be necessary to develop techniques for inferring lower dimensional representations of protein motion on which to map these dynamics [30]. Manifold embedding, diffusion maps, kernel methods and other dimensionality reduction techniques are under intense development for application in a broad range of data science tasks, and LCLS-II-HE will make direct use of these methods and continue to drive their development. These methods will be of particular importance in the study of the structure and dynamics of molecular complexes, exploiting large datasets of scattering patterns or spectra.

3.6.2 Automatic pattern recognition for distinguishing groups of data or events

Large datasets will enable users to rapidly and robustly identify what features of their data distinguish two or more sample configurations or experimental conditions – *e.g.* single-particle versus many-particle hits. Such approaches are already being employed at LCLS, for example to exploit the two-color SASE operating mode where the presence of either X-ray color from LCLS is a stochastic process (output may consist of either pulse-color individually or both together). Neural networks have been employed to learn to distinguish between the two single-color and two-color events (Figure 3.5). The result is a model capable of both classifying events by the X-ray FEL colors present, and understanding the patterns within the data that reveal the temporal and spectral content of the X-ray FEL beam. The data rate and volume from LCLS-II-HE will make manual analysis increasingly burdensome and increase the need for high-performance machine learning algorithms that perform robustly in the presence of large datasets. Similar machine learning concepts will be required for the analysis of large X-ray data sets.

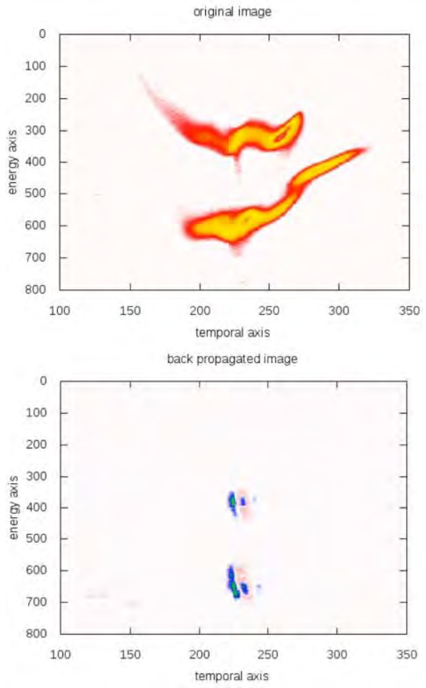

Figure 3.5. Neural networks are employed to discover new structure within LCLS data. Left: Raw output image of an electron-beam diagnostic, the X-ray transverse cavity (XTCAV), which fluctuates substantially from shot to shot. Images such as these are analyzed to determine if one or both of two electron beams contribute to X-ray lasing. Right: By starting from known results, the neural network algorithm was able learn and discover this subtle pattern within the raw XTCAV image. This pattern highlights the specific regions that reveal the lasing conditions for that X-ray shot. The result is sufficiently non-trivial that discovery of this subtle pattern was only possible through machine learning.

3.6.3 Adaptive scanning of higher-dimensional parameter spaces

The experiments enabled by LCLS have grown increasingly complex over the course of the first few years of operation, and this trend will accelerate with LCLS-II and LCLS-II-HE. For instance, LCLS researchers conducted pump-probe experiments involving three different pump pulses prior to the X-ray FEL probe to study photosystem-II [31, 32]. LCLS-II-HE will enable experiments where scanning combinations of many controlled parameters – *e.g.* pump laser or FEL delays, polarizations, intensities, perhaps multiplied by many perturbations and samples – are necessary for success. Each additional experimental variable increases the required data size exponentially (for a fixed statistical power). Advanced computational techniques will not only be necessary for inference in the high-dimensional parameter spaces that result from such experiments, but will further allow closed feedback-loops to drive these experiments to combinations of input parameters the provide the greatest scientific insight.

References

1. K. Kjaer, and K. Gaffney, *et al., in preparation*.
2. W. Zhang*, et al.*, "Tracking excited-state charge and spin dynamics in iron coordination complexes", *Nature,* **509**, 345 (2014).
3. P. Wernet*, et al.*, "Orbital-specific mapping of the ligand exchange dynamics of Fe(CO)$_5$ in solution", *Nature,* **520**, 78 (2015).
4. Y. Shvyd'ko, "Theory of angular-dispersive, imaging hard-x-ray spectrographs", *Phys. Rev. A,* **91**, 053817 (2015).
5. Y. Shvyd’ko*, et al.*, "High-contrast sub-millivolt inelastic X-ray scattering for nano- and mesoscale science", *Nat Commun,* **5**, 4219 (2014).
6. J. P. Sutter*, et al.*, "Examination of Bragg backscattering from crystalline quartz", *JPCS,* **66**, 2306 (2005).
7. P. Kukura, D. W. McCamant, and R. A. Mathies, "Femtosecond Stimulated Raman Spectroscopy", *ARPC,* **58**, 461 (2007).

8. Y. Harada*, et al.*, "Selective Probing of the OH or OD Stretch Vibration in Liquid Water Using Resonant Inelastic Soft-X-Ray Scattering", *Phys. Rev. Lett.,* **111**, 193001 (2013).
9. F. Hennies*, et al.*, "Resonant Inelastic Scattering Spectra of Free Molecules with Vibrational Resolution", *Phys. Rev. Lett.,* **104**, 193002 (2010).
10. H. Yavaş*, et al.*, "Sapphire analyzers for high-resolution X-ray spectroscopy", *Nucl. Instrum. Methods A,* **582**, 149 (2007).
11. S. Harald, "Spectroscopy with meV energy resolution", *J. Phys.: Condens. Matter,* **13**, 7525 (2001).
12. A. K. Rumaiz*, et al.*, "First experimental feasibility study of VIPIC: a custom-made detector for X-ray speckle measurements", *Journal of Synchrotron Radiation,* **23**, 404 (2016).
13. C. Gutt*, et al.*, "Measuring temporal speckle correlations at ultrafast x-ray sources", *Opt. Express,* **17**, 55 (2009).
14. G. Grübel*, et al.*, "XPCS at the European X-ray free electron laser facility", *Nucl. Instrum. Methods B,* **262**, 357 (2007).
15. M. Trigo*, et al.*, "Fourier-transform inelastic X-ray scattering from time- and momentum-dependent phonon-phonon correlations", *Nat Phys,* **9**, 790 (2013).
16. K. Tamasaku, T. Ishikawa, and M. Yabashi, "High-resolution Fourier transform x-ray spectroscopy", *ApPhL,* **83**, 2994 (2003).
17. R. Neutze*, et al.*, "Potential for biomolecular imaging with femtosecond X-ray pulses", *Nature,* **406**, 752 (2000).
18. C. Bostedt*, et al.*, "Linac Coherent Light Source: The first five years", *Reviews of Modern Physics,* **88**, 015007 (2016).
19. T. R. M. Barends*, et al.*, "Direct observation of ultrafast collective motions in CO myoglobin upon ligand dissociation", *Science,* **350**, 445 (2015).
20. J. Tenboer*, et al.*, "Time-resolved serial crystallography captures high-resolution intermediates of photoactive yellow protein", *Science,* **346**, 1242 (2014).
21. D. Arnlund*, et al.*, "Visualizing a protein quake with time-resolved X-ray scattering at a free-electron laser", *Nat Meth,* **11**, 923 (2014).
22. M. Bergh*, et al.*, "Feasibility of imaging living cells at subnanometer resolutions by ultrafast X-ray diffraction", *QRBio,* **41**, 181 (2008).
23. G. Huldt, A. Szőke, and J. Hajdu, "Diffraction imaging of single particles and biomolecules", *Journal of Structural Biology,* **144**, 219 (2003).
24. A. Aquila*, et al.*, "The linac coherent light source single particle imaging road map", *Struct. Dyn.,* **2**, 041701 (2015).
25. Z. Kam, "Determination of Macromolecular Structure in Solution by Spatial Correlation of Scattering Fluctuations", *Macromolecules,* **10**, 927 (1977).
26. Z. Kam, M. H. Koch, and J. Bordas, "Fluctuation x-ray scattering from biological particles in frozen solution by using synchrotron radiation", *Proc. Natl. Acad, Sci. USA,* **78**, 3559 (1981).
27. D. K. Saldin*, et al.*, "Structure of a single particle from scattering by many particles randomly oriented about an axis: toward structure solution without crystallization", *NJPh,* **12**, 14 (2010).
28. E. Malmerberg, C. A. Kerfeld, and P. H. Zwart, "Operational properties of fluctuation X-ray scattering data", *IUCrJ,* **2**, 309 (2015).
29. A. Hosseinizadeh*, et al.*, "High-resolution structure of viruses from random diffraction snapshots", *Phil. Trans. Royal Soc. B,* **369** (2014).
30. A. Dashti*, et al.*, "Trajectories of the ribosome as a Brownian nanomachine", *Proceedings of the National Academy of Sciences of the United States of America,* **111**, 17492 (2014).
31. J. Kern*, et al.*, "Taking snapshots of photosynthetic water oxidation using femtosecond X-ray diffraction and spectroscopy", *Nat Commun,* **5**, 4371 (2014).
32. C. Kupitz*, et al.*, "Serial time-resolved crystallography of photosystem II using a femtosecond X-ray laser", *Nature,* **513**, 261 (2014).

4. LCLS-II-HE Science Opportunities

4.1 Fundamental Dynamics of Energy and Charge in Atoms and Molecules

4.1.1 Electronic and atomic structural dynamics in isolated molecules

The determination of molecular structures in the 20th century has provided a broad foundation for many scientific fields, including chemistry, molecular biology, and materials science. Applications in medicine, drug design, information storage, communication devices, and many other areas have immeasurable benefits for modern society. The determination of molecular structures far from equilibrium and the associated electron motions will drive progress in the current century: Knowledge of those coupled motions will enable the directed manipulation of chemical reactions, the synthesis of yet-unknown materials, and the exploitation of new molecular properties. They will also serve to calibrate computational codes with widespread applications across the sciences, engineering, and medicine.

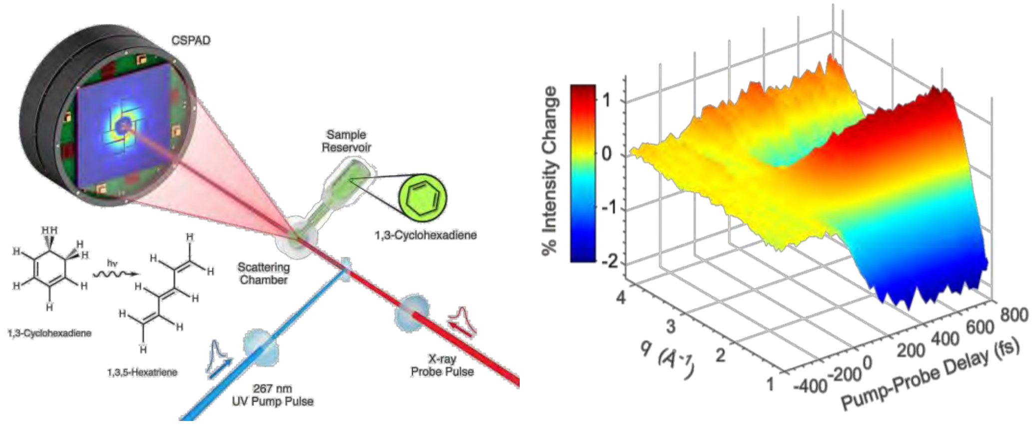

Figure 4.1.1. Left: Experimental setup for the measurement of molecular photoexcited dynamics using hard X-ray scattering: An ultrafast laser pulse creates an electronically excited state in the gas phase molecular sample and launches a molecular reaction. An X-ray probe pulse scatters off the molecular sample, as a function of an adjustable delay, creating a diffraction pattern that encodes the transient molecular structure. Right: The differential transient X-ray diffraction pattern of 1,3-cyclohexadiene as a function of delay time and scattering angle, $\boldsymbol{q}=4\pi/\lambda \sin(\theta)$ following excitation at 267 nm.

Pioneering explorations at LCLS have shown that it is possible to capture time-resolved hard X-ray scattering signals that reveal molecular structures even while ultrafast chemical reactions unfold [1], as illustrated in Figure 4.1.1. By comparing time-resolved X-ray scattering data to a multitude of computational trajectories, the time-dependent molecular structures and reaction pathways can be retrieved [2].

While these groundbreaking LCLS experiments have demonstrated the feasibility of determining the dynamics of molecular photoexcited states, the technique is still in its infancy. Furthermore, determination of the concomitant electronic dynamics has not been possible for gas-phase molecules at dilute concentrations. One significant limitation is the restricted range of scattering angles that can be accessed with the currently available fundamental beam of LCLS (see Figure 4.1.1; the scattering vector extends only to ~4 Å^{-1}). This greatly limits the structural detail that can be resolved as the chemical reaction progresses. Achieving a spatial resolution of one angstrom or better (scattering vector of ~6 $Å^{-1}$) will provide much deeper insight. However, given the current 120 Hz rate of LCLS, data beyond 5 $Å^{-1}$ is inaccessible, as the signal levels are very low in these higher ***q*** regions.

One advantage of gas-phase studies of chemical reactions is the lack of interaction with surrounding molecules, which facilitates the interpretation of results and comparison with theoretical models. It is very challenging, however, to create sufficiently dense molecular targets. As the chemical complexity increases, *e.g.* larger atoms with multiple reaction pathways, the target densities often must be more dilute in order to create and maintain stable samples.

The high-repetition-rate capabilities of LCLS-II-HE will be a qualitative advance, providing ~1,000-fold improvement in data acquisition times and potentially increasing signal-to-noise ratios, even in regions where data are sparse. Combined with 12 keV photon energies, this will more than double the range of observable scattering to nearly 10 $Å^{-1}$. Furthermore, as future LCLS-II-HE performance reaches to 20 keV or beyond (see Section 6), experiments will be able to reach up to 15 $Å^{-1}$. This will transform our ability to determine the transient structures of complex molecules at extremely high accuracy for comparison with theory.

LCLS-II-HE will enable researchers to probe electron and nuclear dynamics with unprecedented clarity. Many of the phenomena at the frontiers of time, in the range of 1-50 fs, remain obscured. For example, despite intense investigations over many decades, the early-time dynamics of photoexcited 1,3-cyclohexadiene continues to be debated [3]. Yet this reaction is a prototypical, textbook organic process that finds myriad applications in synthesis, natural products biology, medicine, and photonic engineering. The high X-ray photon energies, high flux, short pulses, and high repetition rate of LCLS-II-HE will make it possible to image the molecular structural motions and the electron dynamics during the <50 fs time frame that determines the stereospecificity of the reaction [4].

Charge transfer processes play important roles in the conversion of solar energy and in photonic devices. LCLS-II-HE will reveal subtle atomic structural dynamics associated with the very early steps of charge transfer reactions (as discussed in Section 4.2). For example, the coupling of conformational motions to charge transfer processes is particularly relevant in cases where the molecular backbone has multiple vibrational degrees of freedom. Deeper understanding of the role of symmetry breaking in photochemical reactions may open new opportunities for control of chemical reactions by differentially affecting competing chemical reaction pathways. The extremely high photon flux and high repetition rate of LCLS-II-HE will also enable the study of structural dynamics of bimolecular reactions by selectively observing the reacting partners at a particular point in their approach. This will open the door to study the dynamics of a very large class of chemical reactions that remains largely unexplored. Most likely, such an approach would require investigations at the single-molecule level, a frontier that LCLS-II-HE is uniquely suited to conquer.

Self-referenced heterodyne ultrafast time-resolved nanoscale imaging at X-ray FELs

Time-resolved sub-nanometer *coherent* X-ray diffractive imaging was one of the early science drivers identified for XFELs, and this section illustrates the qualitative scientific advances in this area that will be enabled by high-brightness, ultrafast hard X-rays from LCLS-II HE.

Several recent demonstrations of time-resolved X-ray crystallography and time-resolved coherent diffractive imaging of non-periodic objects illustrate the power of XFELs to track both structure and motion in nanometer-scale particles, in nanocrystals of biomolecules, in photoexcited crystalline solids, and in explosions of nanoclusters (as illustrated in Figure 4.1.2) [5-7].

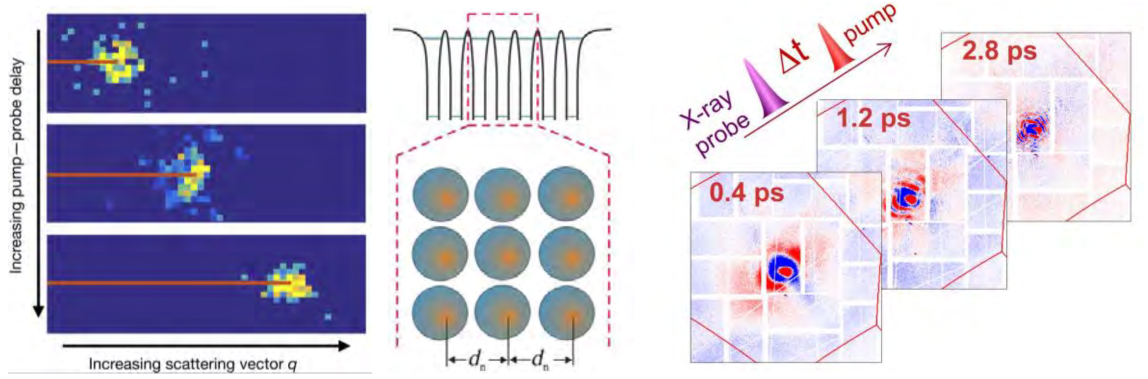

Figure 4.1.2. Left: Time resolved diffraction showing the unexpected contraction of xenon clusters (middle) following laser excitation at delays of up to 80 fs [6]. Right: Time-resolved phonon waves in a solid observed with sub-100fs resolution [7]. Here the solid density overcomes the weak scattering limitations of the gas phase experiments.

These diverse examples have spurred new insights in broad areas of science, but they do not yet achieve the ultimate promise of ultrafast XFELs: to image atoms moving within a single molecular bond in isolated molecules or liquids, with simultaneous sub-Å and few-fs resolution.

Recently, a new approach to X-ray diffractive imaging has been demonstrated at LCLS: ***self-referenced heterodyne imaging***. This method exploits the heterodyne interference between X-rays scattered from the laser-induced moving charge distribution in a molecule and X-rays scattered from the original molecular ground state. This is a nearly universal effect in pump-probe studies of gas phase dynamics, but previously has been nearly unusable owing to the small signal levels. The high repetition rate and hard X-rays from LCLS-II-HE will provide the required signal levels to advance this approach far beyond the simple (diatomic) model system demonstrated to date and will dramatically improve the fidelity of the reconstructed images of charge motion, possibly enabling femtosecond or even sub-femtosecond X-ray movie images of atoms moving in complex molecules.

The self-referencing holographic method exploits the fact that in pump-probe studies typically only a fraction of the molecules in the sample volume are excited, while the rest remain in the ground state. As a result, the X-ray scattering signals from the charge distribution in the initial state and the excited state interfere coherently to produce moving holographic fringes. The sensitivity provided by heterodyne detection means that even if only 1-10% of the ensemble is excited, these fringes have more than sufficient visibility to be seen in the raw data after negative pump-probe delay signals are subtracted.

A recent LCLS experiment provides a striking example of a *de novo* atomic-scale movie. In this work, hard X-rays were scattered from iodine molecules following excitation to vibrationally excited and pre-dissociating states [8]. The fringes in the X-ray scattering (Figure 4.1.3) are due to the cross-correlation between the initial charge distribution and the moving charges, and images of the latter can be extracted by simple heterodyne deconvolution methods. The deconvolved signal is a real-space *de novo* molecular movie.

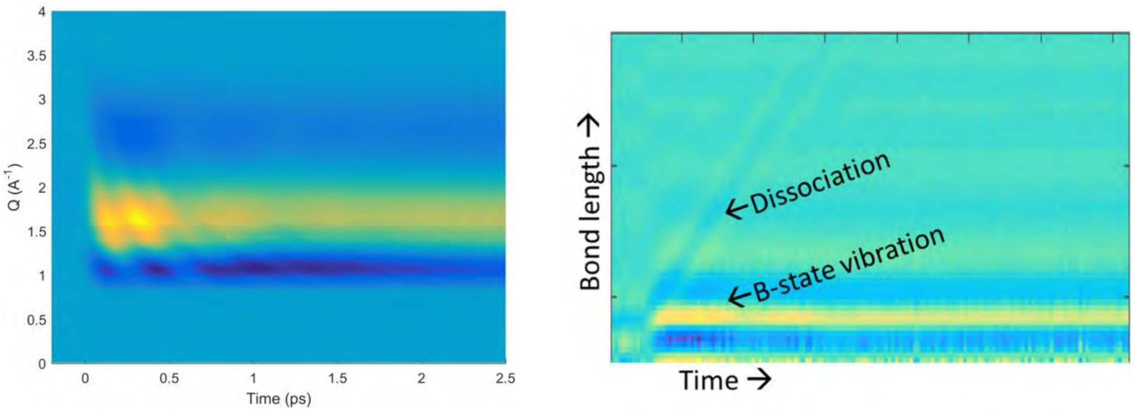

Figure 4.1.3. Laser pump, X-ray probe in I_2. Left: The time-resolved scattering data shows moving fringes due to interference between the ground X-state and photoexcited fractions of the molecule in the B and A excited states. Right: Standard heterodyne deconvolution methods reveal a molecular movie of the excitation, where the scattering fringes seen in the left figure contribute to clear straight tracks of dissociation of the molecule into atomic fragments, as well as oscillations on the excited B-state of the molecule [8].

This direct atomic-scale positional information, delivered in the form of an image, promises to provide a qualitative advance in our understanding of a broad range of complex photochemistry. One important example is the well-studied problem of photoprotection in DNA bases such as thymine (Figure 4.1.4). In the past few years, experiments at LCLS have helped to resolve a longstanding controversy over the physical mechanism by which the energy from UV excitation in this critical DNA base dissipates harmlessly, rather than breaking the molecule apart. The photoabsorption promotes one of the C-C bonding electrons to a dissociative state, but destruction of the molecule is avoided through rapid nonradiative relaxation. But how is this done? Time-resolved spectroscopy at LCLS has shown that the molecule avoids the catastrophe of breaking apart by rapidly donating one of its own electrons from a non-binding position to form a vacancy in a lone-pair orbital near an outlying oxygen atom.

Indirect evidence for this rapid electron motion (through a conical intersection, CI) was first seen in transient Auger spectroscopy following X-ray ionization of the oxygen core level [9]. More recently, time-resolved X-ray photoabsorption from the core levels of the oxygen atom has been used to directly probe the changes in occupancy of the valence orbitals to reveal the charge transfer.

This evolving story of the photoprotection dynamics of thymine has been exciting to observe at LCLS, but something is missing: No one has ever seen how the molecule moves internally to accommodate these changes in the bonding electrons. Self-referencing hard X-ray diffraction using the capabilities of LCLS-II-HE can resolve this puzzle – not only in thymine, but in broad classes of molecules where close coupling of electronic and atomic structure gives rise to conical intersections.

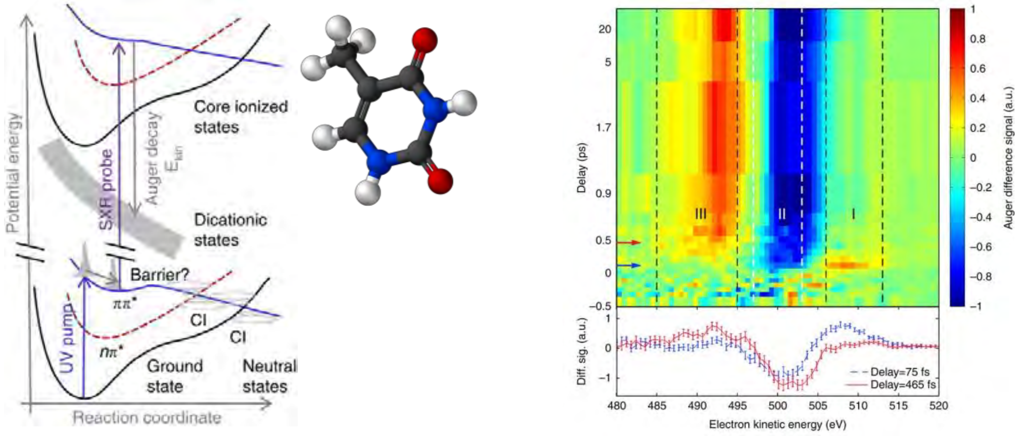

Figure 4.1.4. Left: Thymine potential energy surfaces and conical intersections (CI). Right: The transient oxygen Auger spectrum [9].

4.1.2 Advanced combustion and aerosol chemistry

Understanding the electronic and atomic structural dynamics of isolated molecules, as described above, provides an essential knowledge base for understanding and ultimately controlling more complex chemical reactions. One important example is combustion – which is now, and will remain for many decades, the most important means of energy utilization on Earth. The enormous benefits of modern combustion technologies (*e.g.* reliable electricity, rapid transportation, etc.) are accompanied by negative consequences, such as combustion particulates, photochemical smog, and anthropogenic climate change. It is increasingly important to utilize combustion with greater efficiency and fewer harmful impacts. For example, in the transportation sector, new energy sources such as biomass-derived fuels offer an opportunity to optimize the fuel stream for new, highly efficient engines, and to develop novel fuels that will help reduce greenhouse gas emissions. Climate change concerns create an urgent need for these solutions, reflected in the goal of 80% greenhouse gas emission reductions in the U.S. by 2050. Because of the inherent advantages of liquid hydrocarbons in transportability and energy density, it is likely that they will continue to be used as energy carriers via future energy technologies such as solar fuels. Accordingly, there is an increasing need for predictive models of engine combustion that are accurate from the scale of molecules and electrons through the macroscopic scale of engine cylinders.

The unique capabilities of LCLS-II-HE will be instrumental in creating the science base for predictive combustion models. New, detailed experiments and astonishing advances in computation will combine to deliver truly rigorous science-based models of combustion, with genuine predictive power even for unexplored fuels and combustion strategies. Validating such models will require groundbreaking experimental probes of combustion chemistry and physics, many of which could be realized with the high repetition rate, high average power, and coherent hard X-rays promised by LCLS-II-HE.

Challenges and opportunities in combustion science

Because combustion relies on a complex interrelationship of chemistry and turbulent fluid mechanics, it exhibits inhomogeneities and correlations across a wide range of length and time scales, as illustrated in Figure 4.1.5. These arise from coupling of chemical and fluid-dynamical phenomena. Thus, *chemically specific* dynamic imaging in *dense media* is key for combustion investigations. Hard X-rays from

LCLS-II-HE lasers will image the fundamental chemistry and physics that govern the entire process of combustion, from fuel sprays to gas-phase combustion to particulate formation and evolution. The following presents two critical areas in combustion science (fuel sprays, and particulate formation and oxidation) where these breakthrough capabilities can address problems that remain difficult or impossible to solve with other techniques.

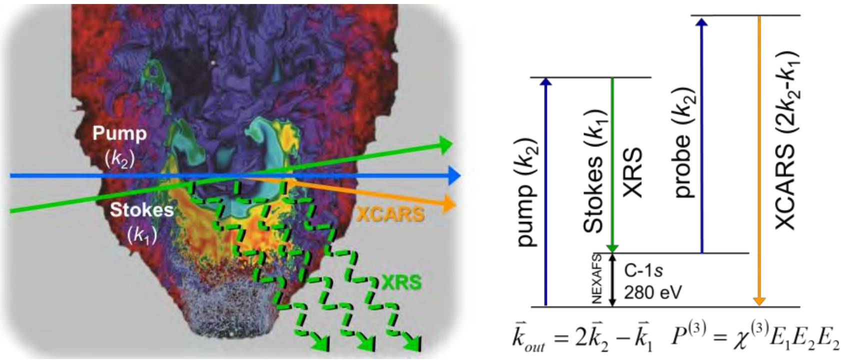

Figure 4.1.5. Illustration of the complexity of the combustion environment. Left: Computer simulations of N_2O, NO, and OH species concentrations in a hydrogen flame (central radius ~2.5 cm) [10]. Right: Diagram for XCARS approach to probe the C-1*s* transition with hard X-rays. While spontaneous X-ray Raman spectroscopy (XRS, dashed green lines) with hard X-rays can probe the C-1*s* transition in dense media, the signals are weak and are not spatially localized, as they originate over the entire X-ray beam path (blue line). XCARS provides a stimulated background-free signal with spatial resolution determined by the crossing point of the k_2 (blue) and k_1 (green) X-ray beams.

Chemistry and physics of fuel sprays

Combustion engines are undergoing radical changes, driven largely by new scientific and technological discoveries, and it is clear that most emerging engine technologies will use direct injection of liquid fuel into the combustion chamber. It is imperative to understand the entire spray – how it breaks up, mixes, vaporizes, and burns – in order to develop fully predictive models for engine combustion. Although these processes control combustion efficiency and emissions formation in every type of direct-injected engine, they remain poorly understood, even at the level of fundamental fluid mechanics. Furthermore, many potentially important couplings of the spray fluid mechanics and chemical environment have simply not been explored. In order to make further progress, significant leaps are required.

As a simple example, it is speculated that under normal diesel engine operating conditions, a small, fuel-rich flame is stabilized just downstream of the liquid jet, leading to soot formation at the tip of the flame [11]. However, in this region, the fuel/air ratio and the existence of a flame have never been measured. Furthermore, under very high levels of exhaust gas recirculation (EGR), which is used to lower NO production, this region of the spray appears to be completely changed, especially as it evolves downstream [12]. Again, the fuel/air ratio is unknown, as is the chemical effect of EGR entrainment, or the differing effects of fuel-bound or free oxygen. Exploring these issues requires information about the interior of sprays, with chemical detail never before available. In the combusting spray, the chemical bonding environment of carbon, for example, moves from liquid fuel to vaporized fuel through the combustion process to carbon monoxide, carbon dioxide, or particulate carbon (soot). Correlation of these chemical transformations with the physics of the spray will be a tremendous breakthrough that will become possible with LCLS-II-HE.

Probing the mass transport, differential evaporation, and oxidative chemistry of fuel flows at the high pressures (~30 atm) and temperatures (~1,000K) that are directly relevant to next-generation engine designs is extremely challenging. Light scattering in a dense spray can confound optical methods, requiring strategies such as ultrafast ballistic imaging [13, 14] and X-ray absorption [15] to probe the critical spray formation region. In fact, even with the current state of the art, spatial and temporal imaging of the fluid structures is at best incomplete. Imaging the interior of the spray with chemical specificity is essentially impossible at present.

The truly transformational aspects of LCLS-II-HE are in the ability to *chemically* resolve spatio-temporal structures of multiphase reacting flows. In principle, hard X-ray Raman scattering can provide similar chemical information to near-edge absorption spectroscopy for dense media, but cross sections for spontaneous X-ray Raman scattering are low. Here, the high power, coherence, and narrow bandwidth of LCLS-II-HE pulses will enable *stimulated* X-ray Raman spectroscopies (SXRS) [16] that can bring many orders of magnitude increase in efficiency over spontaneous Raman. X-ray coherent anti-Stokes Raman spectroscopy (XCARS), a version of SXRS shown in Figure 4.1.5, is a possible way to spatially resolve the changes in chemical bonding across the reacting spray, even for highly scattering environments. The changes in the molecular K-edge spectra are mapped onto the frequency offset of the XCARS signal. The temporal resolution will be determined by the amount of averaging required (as dictated by the available average power), but stimulated coherent X-ray Raman spectroscopy opens a unique window into the interior chemistry of a fuel spray in operating conditions. Because hard X-ray wavelengths can be chosen to transmit through the spray, and because the XCARS signal arises only from the area where the beams cross, chemical information is obtained at chosen locations within even a dense spray.

Importantly, LCLS-II-HE will have a unique capability for two-color nonlinear X-ray methods exploiting two independently tunable hard X-ray beams generated by two successive bunches from the CW-SCRF linac. A Bragg optic delay line compensates the ~10 ns delay between the bunches, allowing the two X-ray pulses to be delivered coincident in time to a single end station. Instrument NEH 1.2 (TXI) [17] is presently under development for LCLS-II, and LCL-II-HE will extend the operation of this two-beam instrument to the hard X-ray range (see Section 5.3).

Aerosol chemistry and soot formation

The growing concern over adverse health effects [18-20] and environmental effects [20-22] of small particles has prompted strict regulation of fine particulate emissions [23], and has intensified research on the control and impact of combustion-generated particles. However, there are significant limitations on our ability to control soot emissions or develop mitigation strategies, and overcoming these limitations will require addressing severe deficiencies in our understanding of particle formation and evolution during combustion [24].

Figure 4.1.6 summarizes the complex chemistry of soot formation and evolution in a flame, starting from the production of hydrocarbon radicals during initial fuel oxidation [25-27] that grow to form incipient nanoparticles (2-10 nm size, shown in red in Figure 4.1.6) [28, 29]. Eventually agglomerated particles become covalently bound aggregates (at ~100 nm scale) with a fine structure resembling polycrystalline graphite (shown in green in Figure 4.1.6) [27]. Subsequent oxidation of these graphitic particles [30] leads to the formation of CO and CO_2 [31].

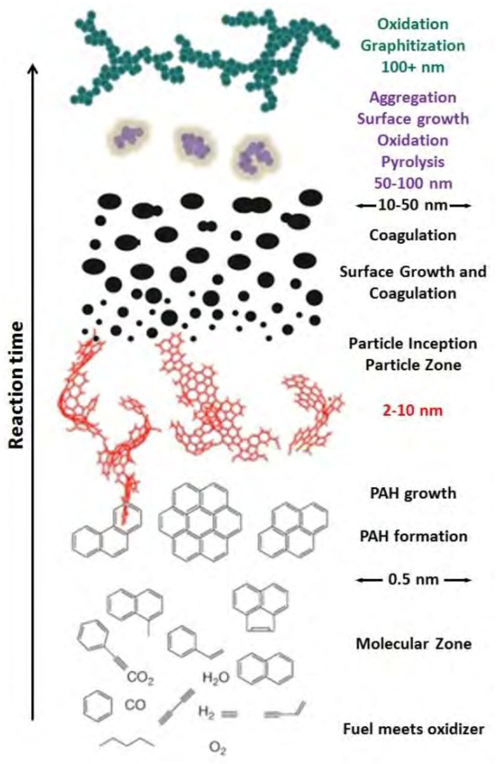

Figure 4.1.6. Schematic of soot formation and evolution in a flame starting from the production of hydrocarbon radicals during initial fuel oxidation [25-27]. These radicals lead to higher molecular-weight growth and polycyclic aromatic hydrocarbons (PAH) [26] that grow to form incipient nanoparticles in the size range of 2-10 nm (red) [28, 29]. Coagulation, hydrogen loss and surface growth continue until these agglomerated particles become covalently bound aggregates of mostly carbonaceous particles with a fine structure resembling polycrystalline graphite (green) [27]. Subsequent oxidation of these graphitic particles proceeds at "active" sites [30] on the graphitic surface to form CO and CO_2 [31] Molecular structures and particles are not drawn to scale. This figure is an update of a figure from Bockhorn [25], modified with molecular species predicted to initiate soot formation (Violi, personal communication) and extended to include aggregation, graphitization, and oxidation of mature graphitic soot.

Studies of soot chemistry require measurements of soot composition, size, morphology, and volume fraction. A wide range of *ex situ* techniques have been employed to date, and these are extremely valuable in providing information about particle composition, size, and morphology. Unfortunately, they rely on extractive sampling, which (i) causes significant perturbations to the combustion system and (ii) leads to condensation of gas-phase species onto the particles, complicating interpretation of the results. *In situ* techniques, on the other hand, avoid complications associated with extractive sampling and are much less invasive, but viable *in situ* techniques for studies of soot in combustors are sorely lacking.

X-ray diagnostics can provide considerable information about the chemical and physical characteristics of particles. Hard X-ray techniques are particularly appealing because they may allow *in situ* measurements of combustion systems at elevated pressures, which is necessary for understanding combustion under engine-relevant conditions. Measurements made at LCLS-II-HE will be transformational in advancing our understanding of combustion chemistry, particularly when coupled with theory and combustion modeling.

Probing particle composition

Near-edge X-ray absorption fine structure (NEXAFS) spectroscopy is a powerful tool for probing particle composition and carbon electronic structure [32-34]. Figure 4.1.7 shows examples of NEXAFS spectra recorded on soot samples extracted from selected locations in a premixed flat flame. This figure demonstrates signatures of functional groups and carbon hybridization that change with particle evolution in the flame and can be used to study formation, oxidation, and graphitization in the flame. However, the spectra were recorded *ex situ*. Previous work by Frank *et al.* [35] has demonstrated that NEXAFS spectra can be collected *in situ* in a flame, but the flame must be under vacuum to allow sufficient soft X-ray transmission at the carbon K-edge of ~285 eV.

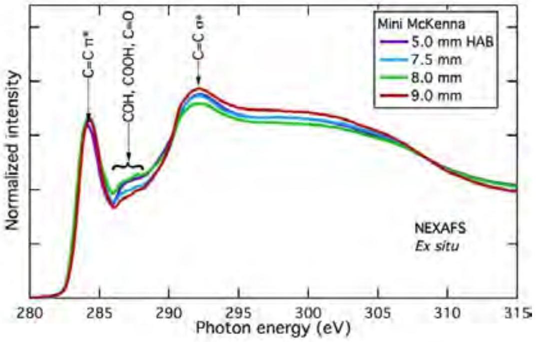

Figure 4.1.7. NEXAFS spectra recorded at the carbon K-edge. Spectra were recorded on soot samples collected from an atmospheric ethylene-air premixed flat flame at selected heights above the burner (HABs). Signatures of functional groups are labeled (H. Michelsen *et al.* unpublished).

Spontaneous X-ray Raman spectroscopy (XRS) offers the ability to probe the carbon K-edge using hard X-rays under normal operating conditions and pressures. Figure 4.1.5 shows an energy-level diagram that compares XRS transitions with those of NEXAFS. Whereas NEXAFS is a direct transition from the 1*s* orbital to the LUMO at ~285 eV, the same transition is probed in XRS using a hard X-ray, non-resonant-probe photon energy and detecting the hard X-ray inelastically scattered Stokes signal.

Figure 4.1.8 shows *in situ* XRS spectra recorded with the same flame configuration used to generate the soot probed by the NEXAFS spectra shown in Figure 4.1.7. These XRS spectra were recorded on Beam Line 6-2 at the Stanford Synchrotron Radiation Lightsource (SSRL) using the Si(111) monochromator, which delivered photons at ~6.5 keV with a flux of $2{\cdot}10^{13}$ photons/s and energy resolution of 0.85 eV [36]. Because both the incident beam and signal were in the hard X-ray regime, the experiment could be performed at atmospheric pressure without excessive loss of signal.

The most striking features in the spectra shown in Figure 4.1.8 are those attributable to gas-phase CO and CO_2 in the flame. The underlying features of the soot particles and precursors are difficult to discern in these spectra, and extracting them from the gas-phase interference is beyond the capabilities of present X-ray sources (given the extremely low XRS cross section). The high repetition rate of LCLS-II-HE, and its associated increase in average flux, will reveal these subtle features of *in situ* XRS spectra and will open the door for pump-probe experiments, *e.g.* for isolating the signals of the soot particles from the gas-phase species. Another advantage is that XRS can be performed simultaneously with hard X-ray techniques to probe soot particle size and morphology, as discussed in the following section.

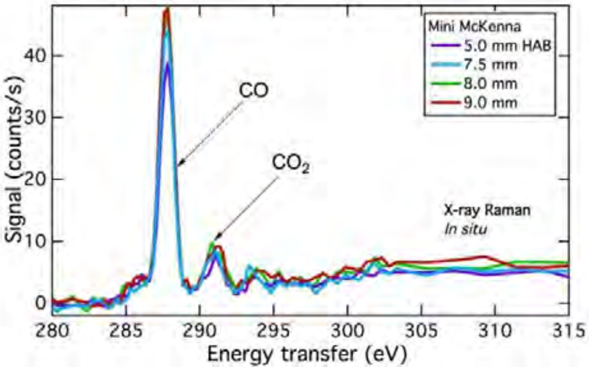

Figure 4.1.8. XRS spectra recorded at the carbon K-edge using photons in the 6.5 keV range. Spectra were recorded *in situ* in the flame produced by the same burner as used for the NEXAFS spectra in Figure 4.1.7 (H. Michelsen *et al.* unpublished).

The results displayed in Figure 4.1.8 demonstrate the feasibility of probing these transitions using XCARS, which can offer orders of magnitude more signal than XRS [16]. This increase in signal is attributable to the spatial coherence of the XCARS photons, which are scattered into a small solid angle rather than the 4π emission of XRS photons. In addition, XRS depends linearly on incident photon flux, whereas XCARS depends on the third order susceptibility and is nonlinearly dependent on photon flux. LCLS-II-HE will provide high photon flux and phase coherence to enable implementation of XCARS.

Probing particle size and morphology

Particle formation chemistry controls incipient particle size and morphology. These characteristics are not readily measurable; the particles are too small to be measured at laser wavelengths and too easily perturbed by probes to be measured by *ex situ* techniques. Loh *et al.* [37] used coherent diffractive imaging to produce images of isolated particles at LCLS in order to probe the morphology and fractal dimension of individual artificial soot particles. The high repetition rate and hard X-rays from LCLS-II-HE will enable us to probe the morphology of individual incipient particles *in situ* in a flame for the first time. The low density of incipient particles will allow us to sample continuously to generate statistics on these ensemble distributions. These measurements will be complemented by *in situ* measurements of particle size using small-angle X-ray scattering (SAXS) [38-41] and particle fine structure using wide-angle X-ray scattering (WAXS) [40]. The LCLS-II-HE upgrade will also provide the ability to shrink the incident X-ray beam spot and hence increase the spatial resolution of the *in situ* SAXS measurements in different regions of the flame for studies of combustion chemistry. The truly unique aspect of this work is that multiple photon energies at the LCLS-II-HE may allow the simultaneous combination of *in situ* spectroscopy (X-ray Raman) and *in situ* scattering/imaging of soot to get information on both the structure and the chemistry at the same position in the flame.

References

1. M. P. Minitti, *et al.*, "Imaging Molecular Motion: Femtosecond X-Ray Scattering of an Electrocyclic Chemical Reaction", *Phys. Rev. Lett.,* **114**, 255501 (2015).
2. M. P. Minitti, *et al.*, "Toward structural femtosecond chemical dynamics: imaging chemistry in space and time", *Faraday Discuss.,* **171**, 81 (2014).
3. S. Deb, and P. M. Weber, "The Ultrafast Pathway of Photon-Induced Electrocyclic Ring-Opening Reactions: The Case of 1,3-Cyclohexadiene", *ARPC,* **62**, 19 (2011).
4. R. B. Woodward, and R. Hoffmann, "The Conservation of Orbital Symmetry", *Angewandte Chemie International,* **8**, 781 (1969).
5. C. Kupitz, *et al.*, "Serial time-resolved crystallography of photosystem II using a femtosecond X-ray laser", *Nature,* **513**, 261 (2014).
6. K. R. Ferguson, *et al.*, "Transient lattice contraction in the solid-to-plasma transition", *Science Advances,* **2** (2016).
7. M. Trigo, *et al.*, "Fourier-transform inelastic X-ray scattering from time- and momentum-dependent phonon-phonon correlations", *Nat Phys,* **9**, 790 (2013).
8. J. M. Glownia, *et al.*, "Self-referenced coherent diffraction x-ray movie of Angstrom- and femtosecond-scale atomic motion", *arXiv: (to be posted),* (2016).
9. B. K. McFarland, *et al.*, "Ultrafast X-ray Auger probing of photoexcited molecular dynamics", *Nature Communications,* **5**, 4235 (2014).
10. J. B. Bell, M. S. Day, and M. J. Lijewski, "Simulation of nitrogen emissions in a premixed hydrogen flame stabilized on a low swirl burner", *Proceedings of the Combustion Institute,* **34**, 1173 (2013).
11. J.E. Dec, "A Conceptual Model of DI Diesel Combustion Based on Laser-Sheet Imaging," in *SAE Technical Paper 970873*(1997), p. DOI: 10.4271/970873.
12. M. Musculus, and L. Pickett, "Chapter 33: In-cylinder spray, mixing, combustion, and pollutant-formation processes in conventional and low-temperature-combustion diesel engines," in *Advanced Direct Injection Combustion Engine Technologies and Development: Volume : Diesel Engines*, H. Zhao, ed. (Woodhead Publishing Ltd., Cambridge, UK, 2009).
13. J. B. Schmidt, *et al.*, "Ultrafast time-gated ballistic-photon imaging and shadowgraphy in optically dense rocket sprays", *Appl Optics,* **48**, B137 (2009).
14. M. A. Linne, *et al.*, "Ballistic imaging of liquid breakup processes in dense sprays", *Proc. Combust. Inst.,* **32**, 2147 (2009).

15. Wang Y, *et al.*, "Ultrafast X-ray study of dense-liquid-jet flow dynamics using structure-tracking velocimetry", *Nature Phys,* **4**, 305 (2008).
16. S. Tanaka, and S. Mukamel, "Coherent X-ray Raman spectroscopy: A nonlinear local probe for electronic excitations", *Phys. Rev. Lett.,* **89**, 043001 (2002).
17. "APEX Experimental Results and Simulation Comparison," https://docs.slac.stanford.edu/sites/pub/Publications/APEX_Experimental_Results and_Simulation_Comparison.pdf.
18. J. S. Lighty, J. M. Veranth, and A. F. Sarofim, "Combustion aerosols: Factors governing their size and composition and implications for human health", *J. Air Waste Manage. Assoc.,* **50**, 1565 (2000).
19. N. A. H. Janssen, *et al.*, "Black carbon as an additional indicator of the adverse health effects of airborne particles compared with PM10 and PM2.5", *Environ. Health Perspect.,* **119**, 1691 (2011).
20. E. J. Highwood, and R. P. Kinnersley, "When smoke gets in our eyes: The multiple impacts of atmospheric black carbon on climate, air quality, and health", *Environ. Int.,* **32**, 560 (2006).
21. IPCC, *Climate Change 2013: The Physical Science Basis. Working Group I Contribution to the Fifth Assessment Report of the Intergovernmental Panel on Climate Change* (Cambridge University Press, Cambridge, UK and New York, NY, 2013).
22. T. C. Bond, *et al.*, "Bounding the role of black carbon in the climate system: A scientific assessment", *JGR,* **118**, 5380 (2013).
23. Executive_Office_of_the_President, "The President's Climate Action Plan," (http://www.whitehouse.gov/sites/default/files/image/president27sclimateactionplan.pdf, June 2013).
24. DOE, "Report of the Basic Energy Sciences Workshop on Basic Research Needs for Clean and Efficient Combustion of 21st Century Transportation Fuels ", Office_of_Science, ed. (2006).
25. H. Bockhorn, *Soot Formation in Combustion: Mechanisms and Models* (Springer-Verlag, Berlin, 1994).
26. H. Richter, and J. B. Howard, "Formation of polycyclic aromatic hydrocarbons and their growth to soot - a review of chemical reaction pathways", *PrECS,* **26**, 565 (2000).
27. K.-H. Homann, "Fullerenes and soot formation - New pathways to large particles in flames", *Angew. Chem. Int. Ed.*, 2434 (1998).
28. H. Wang, "Formation of nascent soot and other condensed-phase materials in flames", *Proceedings of the Combustion Institute,* **33**, 41 (2011).
29. A. Violi, "Modeling of soot particle inception in aromatic and aliphatic premixed flames", *CoFl,* **139**, 279 (2004).
30. J. R. Hahn, *et al.*, "Mechanistic study of defect-induced oxidation of graphite", *JPhCh,* **103**, 9944 (1999).
31. B. R. Stanmore, J. F. Brilhac, and P. Gilot, "The oxidation of soot: A review of experiments, mechanisms, and models", *Carbon,* **39**, 2247 (2001).
32. S. di Stasio, and A. Braun, "Comparative NEXAFS study on soot obtained from an ethylene/air flame, a Diesel engine, and graphite", *Energy & Fuels,* **20**, 187 (2006).
33. H. A. Michelsen, *et al.*, "Particle formation from pulsed laser irradiation of soot aggregates studied with a scanning mobility particle sizer, a transmission electron microscope, and a scanning transmission x-ray microscope", *ApOpt,* **46**, 959 (2007).
34. A. Braun, *et al.*, "Radiation damage from EELS and NEXAFS in diesel soot and diesel soot extracts", *JESRP,* **170**, 42 (2009).
35. J. H. Frank, *et al.*, "In situ soft X-ray absorption spectroscopy of flames", *ApPhB,* **117**, 493 (2014).
36. D. Sokaras, *et al.*, "A high resolution and large solid angle x-ray Raman spectroscopy end-station at the Stanford Synchrotron Radiation Lightsource", *Rev. Sci. Instrum.,* **83**, 043112 (2012).
37. N. D. Loh, *et al.*, "Fractal morphology, imaging and mass spectrometry of single aerosol particles in flight", *Nature,* **486**, 513 (2012).
38. J. P. Hessler, S. Seifert, and R. E. Winans, "Spatially resolved small-angle x-ray scattering studies of soot inception and growth", *Proceedings of the Combustion Institute,* **29**, 2743 (2002).
39. J. B. A. Mitchell, *et al.*, "Small angle x-ray scattering study of flame soot nanoparticle aggregation and restructuring", *JAP,* **105**, 124904 (2009).
40. F. Ossler, *et al.*, "Dynamics of incipient carbon particle formation in a stabilized ethylene flame by in situ extended-small-angle- and wide-angle X-ray scattering", *Carbon,* **51**, 1 (2013).
41. A. W. Kandas, *et al.*, "Soot surface area evolution during air oxidation as evaluated by small angle X-ray scattering and CO_2 adsorption", *Carbon*, 241 (2005).

4.2 Catalysis, Photocatalysis, Environmental & Coordination Chemistry

4.2.1 Coupled dynamics of energy flow: molecular structure and charge

Charge separation, migration, redistribution, and localization are central to efficient and robust energy storage and retrieval from chemical bonds through complex processes such as photosynthesis and catalysis. Indirect evidence points to the importance of the coupled evolution of electronic and nuclear wave functions in many molecular systems. However, they are not well understood at the quantum level, even in simple molecules. We have not been able to directly observe these processes to date, and they are beyond the description of conventional models.

Of particular interest are light-driven reactions that can be initiated by photon absorption in either solid state materials or molecular light harvesting systems connected to catalytic centers. In molecular light harvesters, photoexcitation generates an excited state electron and an electronic vacancy (hole). The energetic electrons can be used to drive reductive catalytic reactions, and the holes can be used to drive oxidative catalytic reactions. The electron transfer between light harvester and catalytic site can be mediated either by direct chemical bonding (*e.g.* in a molecular photocatalytic assembly) or through semiconductor and redox relays. The following sections will describe how experiments conducted at LCLS-II-HE will facilitate the development of systems for artificial photocatalysis and provide novel insights into natural photocatalysts.

High-repetition-rate, ultrafast hard X-rays from LCLS-II-HE will enable advanced X-ray techniques that simultaneously measure electronic structure and subtle nuclear displacements at the atomic scale, on fundamental timescales (femtoseconds and longer), and in operating environments requiring the penetrating capabilities of hard X-rays. The power of this approach (illustrated in Figure 4.2.1) has been demonstrated in recent experiments at LCLS in which hard X-ray scattering and X-ray emission spectroscopy (XES) from a model transition-metal charge transfer complex have been measured simultaneously to reveal the coupling of photo-induced charge transfer and atomic structure – on the sub-Å scale, and on the 100 fs timescale – for the first time.

Applying these techniques to much more complex light harvesting and photosynthetic assemblies, both natural and artificial, will require a much higher repetition rate to extract quantitative information that can be used to inform design and synthesis. For example, studies to date have been limited to relatively simple molecules in high concentrations with high photolysis yields, whereas functioning assemblies typically have low concentrations of active sites and must be investigated at low photolysis levels to properly understand how they operate.

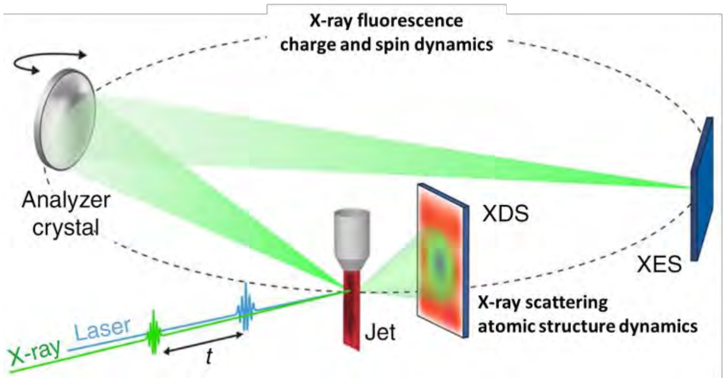

Figure 4.2.1. Setup for simultaneous probing of electronic and atomic structural dynamics with hard X-rays via emission (XES) and scattering (XDS) [1].

LCLS-II-HE will enable element-specific probing of the fine details of the valence excited-state charge dynamics by exploiting sensitive valence-to-core XES and resonant inelastic X-ray scattering (RIXS) in the 5-12 keV range. High-resolution RIXS will further enable element-specific mapping of excited-state potential-energy surfaces (PES). Time-resolved XFEL studies to date have been limited by the average spectral flux (ph/s/meV) to core-to-core X-ray emission lines, which are less informative. Although some demonstration RIXS experiments have been performed at LCLS, they have been limited to single time snapshots of large chemical changes in simple molecules at high concentration [2, 3]. LCLS-II-HE will provide a similarly dramatic advance for powerful differential extended X-ray absorption fine structure (EXAFS) studies of changes in local structure at the 0.01 Å scale. The 5-12 keV range spans the core resonances of the 3*d* transition metals (*e.g.* Fe and Cu K-edges at 7.1 and 9 keV) that are the basis for many biological enzymes and photocatalysts, and the 4*d* and 5*d* metals (*e.g.* Pt L_3-edge at 11.6 keV) on which existing man-made catalysts and photosynthetic assemblies have largely relied.

Rational design of Earth-abundant light harvesters

First row (3*d*) transition metals are attractive components in both light harvesting and catalytic systems, as they are typically inexpensive, Earth-abundant, and environmentally benign. Development of molecular light harvesters based on 3*d* transition metals [4, 5] has benefitted from the fact that the functionality of transition-metal-centered systems is highly tunable through ligand modification and substitution. However, functional tunability results in almost infinite possible design strategies for synthesizing new systems or improving existing ones. Therefore, experiments that capture the photoexcited electron transfer pathways and mechanisms are crucial to identify which excited potential energy surfaces should be targeted for modification. This will provide a unique opportunity to make rational design decisions for the next generation of molecular light harvesters.

The power of combined hard X-ray scattering and XES to reveal these exact charge transfer pathways and mechanisms in unprecedented detail has been demonstrated in recent experiments at LCLS. Figure 4.2.2a illustrates a model system for iron-based light harvesters, [Fe(bpy)$_3$]$^{2+}$. Hard X-ray emission and scattering studies of this complex allowed for direct quantification of the coupled electronic and structural configurations (Figure 4.2.2c, circles and gray lines).

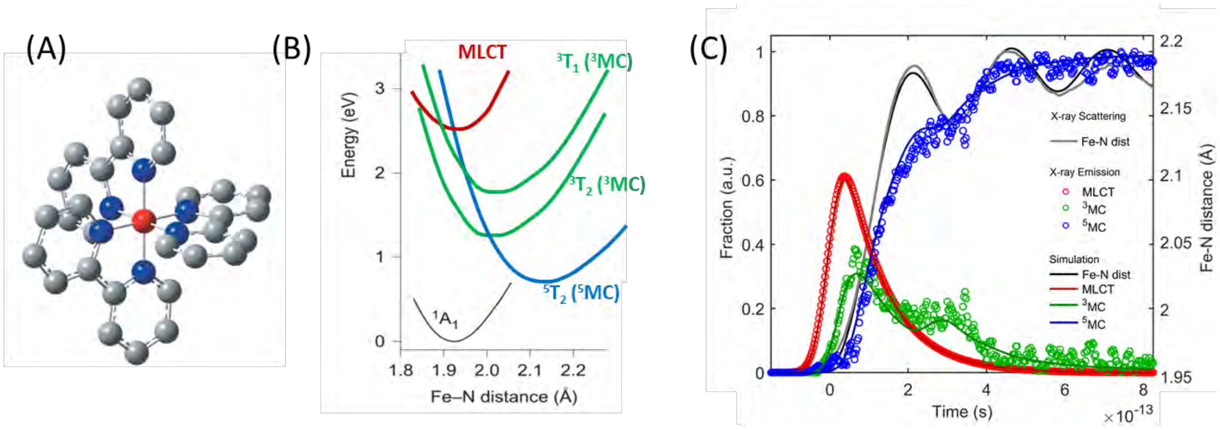

Figure 4.2.2. Results of combined hard X-ray scattering and XES studies of a model system for light harvesting: (A) [Fe(bpy)$_3$]$^{2+}$, (B) calculated potential energy surfaces, and (C) experimentally determined electronic and atomic structural dynamics compared to a simulation from the same potential energy surfaces (K. Kjaer *et al.* unpublished).

In reproducing the observed dynamics (Figure 4.2.2c, black and colored lines) by simulating the trajectory of the system on the excited state potential energy surfaces (Figure 4.2.2b), it was possible to determine excited state lifetimes, structural coherence, the locations of intersections between potential energy surfaces and the transition probabilities between surfaces. Most significantly, coherent electronic transitions are observed between the ^{3}MC and ^{5}MC states (*e.g.* at ~300 fs) that coincide with modulation of the Fe-N bond distance.

Applied to functional systems, such details of the excited-state dynamics reveal how the molecular light harvester actually functions. It also shows which potential energy surfaces need to be modified for improved functionality. However, this high level of detail can currently be obtained only for relatively simple model complexes that exhibit large structural changes at high concentrations. LCLS-II-HE will enable the application of simultaneous X-ray scattering and XES (including valence-to-core XES) to reveal the subtle coupled changes in the atomic and electronic structure that underpin many important 3*d* transition metal complexes designed for light harvesting. Applied under operating conditions (often at dilute concentrations), this will provide revolutionary new insight towards the development of these molecular systems.

4.2.2 Photocatalysis

Model molecular photocatalytic assemblies

Linking molecular light harvesters directly to a catalytic site is an important and promising approach for solar energy conversion and related applications. However, understanding the complex excited state processes at the level of detail required for rational design remains a significant science challenge. The model photocatalyst illustrated in Figure 4.2.3 highlights the challenges that impact the performance of molecular photocatalysts [1]. A charge-transfer excitation from the Ru(II) metal center efficiently harvests visible light. This initiates a series of ultrafast changes in electronic and atomic structure, including electron transfer, solvation between the distinct coordinating ligands, and changes in both oxidation and spin states. In principle, the transient Ru(III) and Co(II) sites can catalyze oxidation and reduction reactions. Combining XES and X-ray scattering enables identification of photoinduced electron transfer (ET) pathways, structural dynamics, and thermalization processes. However, the data quality currently achievable from low-repetition-rate XFELs does not allow a complete characterization of the underlying potential energy landscape. If we are to develop effective design rules for manipulating these charge transfer processes through intra- and inter-molecular modification, much more detailed information is essential. Moreover, understanding the catalytic reactions at the active sites of the system will require more sensitive experimental probes.

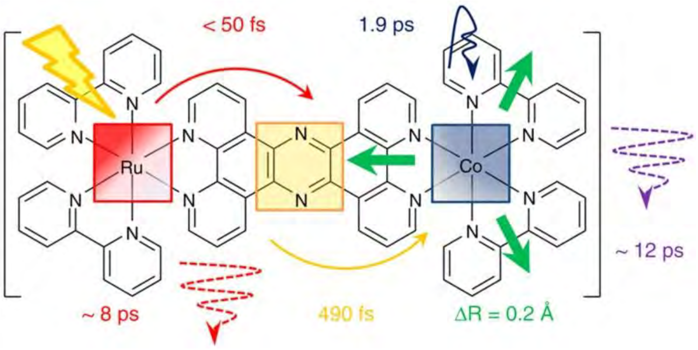

Figure 4.2.3. Non-equilibrium electron transfer across the photoexcited (1RuII=1CoIII) model photocatalyst. The fundamental timescales are indicated, as obtained from transient optical absorption spectroscopy, X-ray emission spectroscopy, and X-ray scattering [1].

Simultaneous measurements of the excited state electronic configuration at the active site (valence-to-core XES or RIXS) and detailed measurements of the excited state active site structural configuration (EXAFS) will provide mechanistic insights into the functionality of these systems. Moreover, high resolution vibrational RIXS will enable element-specific mapping of excited-state potential energy surfaces, as discussed in Section 3.2. Connecting such information with insight from computational chemistry is essential if we are to develop effective design rules for functional molecular catalysts.

Natural and artificial multi-electron photocatalysts

All reactions essential for fuel generation from sunlight (*e.g.* reduction of CO_2, oxidation of H_2O and reduction of protons to generate H_2) require two or more instances of charge transfer to complete each of the reactions. In order to design catalysts that meet this criterion, the step-by-step mechanism of the catalytic cycle (spanning femtoseconds to milliseconds) needs to be unraveled, including electron-hole separation, charge accumulation, the evolution of the atomic/molecular structure, the energetics and kinetics of each charge-state intermediate, and the reaction of photo-generated carriers with adsorbate species. The complexity of the problem calls for studies addressing multiple timescales and multiple elements. The higher energy range and higher repetition rate of LCLS-II-HE, coupled with uniform materials, will qualitatively advance the field.

Brookite (TiO_2) nanorods coupled to highly uniform Pt nanocrystal co-catalysts provide an illustrative example. In recent studies, well-defined rods have been shown to efficiently generate H_2 from the oxidation of a variety of biomass-derived organic substrates [6]. Importantly, evidence from transient absorption spectroscopy suggests that the electron-hole recombination can be controlled by engineering the length of the nanorods (as illustrated in Figure 4.2.4), and this relates directly to catalytic reactivity.

However, optical spectroscopy does not reveal key details of the relevant electronic states of TiO_2, Pt or the interface region. High-sensitivity time-resolved hard X-ray spectroscopy enabled by LCLS-II-HE will provide a full characterization of the states associated with photocatalysis in this hybrid system under operating conditions, and thereby identify promising routes for further optimization or directed design. For example, recent time-resolved XAS studies of aqueous anatase TiO_2 nanoparticles at the Ti K-edge (4.97 keV) revealed localization of charge within 300 fs at Ti^{3+} centers [7]. LCLS-II-HE will enable a similar approach to be applied to an operating catalytic assembly, probing both the TiO_2 states and the Pt states at the L_3-edge (11.6 keV) to provide a full picture of charge recombination events and their relation to chemical reactivity.

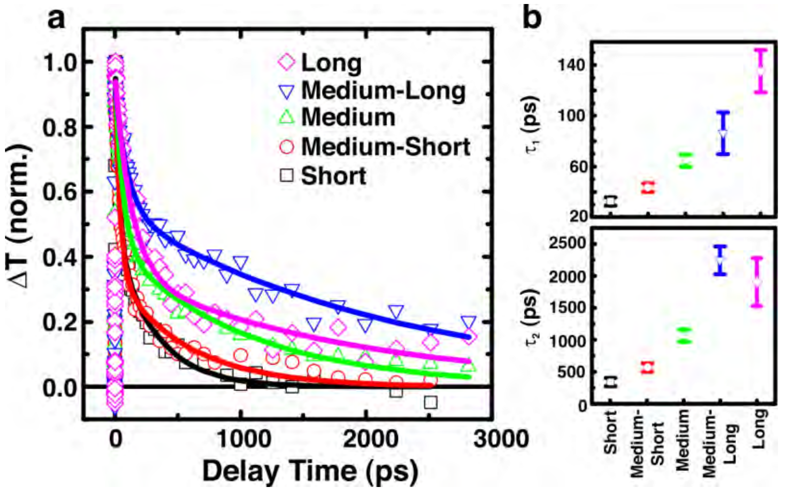

Figure 4.2.4. *In situ* transient absorption spectroscopy of brookite nanorod TiO_2/Pt photocatalysts following photoexcitation at 4.0 eV. Bi-exponential time constant fits are shown by solid lines (a), and summarized as a function of rod length (b) [6].

Another important recent example of artificial photocatalysis is the temporally resolved observation of surface intermediates of water oxidation from a first-row metal-oxide catalyst based on Co_3O_4 nanoparticles [8] (Figure 4.2.5). While vibrational spectroscopy has provided limited structural details of the surface intermediates during the catalytic cycle, time-resolved X-ray spectroscopy will be able to provide element-specific information on the dynamic changes of the electronic structure and coordination environment of the active metal centers during the catalytic cycle.

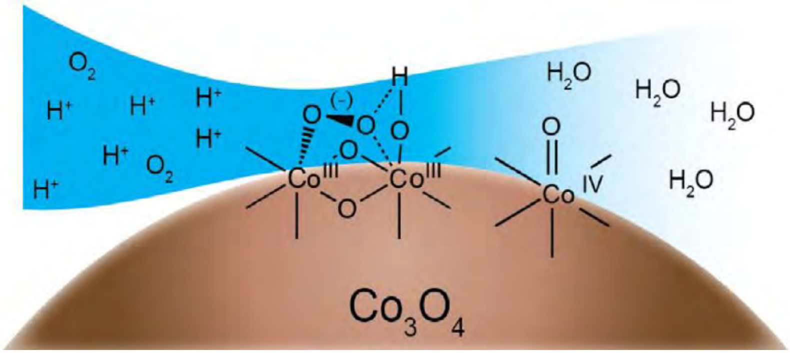

Figure 4.2.5. Visible light sensitized water oxidation at Co_3O_4 nanocatalyst surface. Two surface intermediates are detected: surface superoxide (three-electron oxidation intermediate) and oxo Co(IV) site (one-electron oxidation intermediate) [8].

The multi-metal probing capability of charge dynamics (via XES and RIXS) and nuclear structure (via scattering and/or EXAFS) on timescales from femtoseconds to milliseconds will allow detection of the dynamic structural changes of active surface metal centers. Specifically, this sensitive approach enabled by LCLS-II-HE will address questions of how charges transferred to Earth-abundant metal oxides induce catalytic changes on the particle surface, and how transferred charges advance the catalytic activity through multiple sequential steps.

One important example from nature that illustrates the potential for this new class of science at LCLS-II-HE is the site for water oxidation (Mn_4CaO_5 cluster) that acts as a charge storage device in the reaction center of photosystem II (PS-II), accumulating oxidation equivalents after each light-induced charge separation (Figure 4.2.6). Tremendous progress has been made in the structural characterization of this catalytic center in its resting state, culminating in the recent high-resolution (1.95 Å) structure of the first cycle step based on serial crystallography at the SACLA XFEL, enabled for the first time under non-damaging conditions using ultrafast X-ray pulses [9].

While low-repetition-rate XFEL studies of PS-II represent important advances [10, 11], these static pictures only scratch the surface of the information necessary to deduce the electronic configuration of the metals and the flow of charge within the catalytic center during all four steps of the reaction cycle. In particular, the electronic and atomic structures of the metastable S_4 state, where O-O bond formation occurs, remain largely unknown. Characterizing and understanding these subtle changes requires elaborate spectroscopic techniques such as valence-to-core XES, RIXS, high-resolution vibrational RIXS, and EXAFS, which will become available for the first time with LCLS-II-HE.

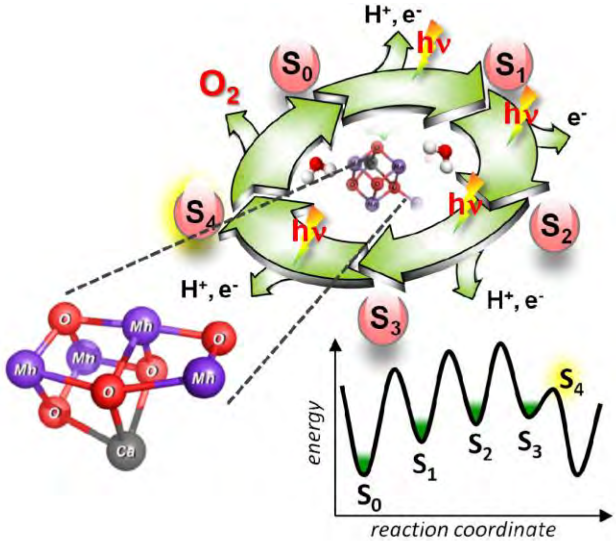

Figure 4.2.6. Catalytic scheme for the four S-state transitions in the Mn_4CaO_5 cluster of photosystem II [12].

In summary, hard X-rays at high repetition rate from LCLS-II-HE will be indispensable for simultaneously following transient valence electronic configurations (via XES and RIXS) and atomic structure (via EXAFS and coherent scattering) with the required sensitivity. Importantly, the uniform pulse structure enabled by the CW-SCRF linac is ideally suited for pulse-by-pulse sample delivery/replacement, enabling ~10^8-10^{10} independent measurements per day. By exploiting revolutionary advances in data science (as discussed in Section 3.6) it should be possible to extract information about rare transient events from comprehensive data sets.

4.2.3 Homogeneous catalysts: Correlated chemical reactivity & structural dynamics

Beyond the photocatalysts described above, catalysts that accelerate and direct chemical reactions are of vital importance in virtually all areas of energy generation, from processing fossil fuels to converting non-fossil fuel stock, producing chemicals, reducing harmful emissions from combustion, and mitigating climate change. More efficient, selective catalysts with greater yield and less waste that are simultaneously robust, chemically selective, and based on abundant materials will be essential to meeting the world's future demand for energy, food, and chemicals, and this requires a much greater understanding of catalysis.

In nature, biological catalysts, or enzymes, enable organisms to perform thermodynamically highly demanding chemical transformations under ambient conditions and as close to the thermodynamic limit as possible, often involving only very subtle structural changes. Many exploit Earth-abundant (3*d*) transition-metal active sites. They accelerate and direct chemical reactions by introducing transient intermediate steps that quickly stabilize charge-separated states via electron transfer chains. In addition, enzymatic systems often incorporate integrated self-repair capabilities and are highly regulated to control the synthesis of desired products and minimize undesirable by-products. LCLS-II-HE will enable us to use sensitive X-ray scattering and spectroscopy techniques at transition-metal resonances to capture rare transients and follow the intertwined charge and structural dynamics associated with each step of the catalytic cycle on the atomic scale. This will qualitatively advance our understanding of natural systems and inform the design of artificial catalysts and networks with targeted functionality.

Developing and characterizing light-driven biocatalysts and bio-enzyme hybrids

While pump-probe studies at LCLS-II-HE are naturally suited to study the functioning of photocatalysts, many important biocatalysts, including hydrogenase and nitrogenase, are not directly driven by light. The hydrogenase enzyme catalyzes the reversible oxidation of molecular hydrogen (H_2), which is important for numerous biological functions and is of significant interest for applications in biofuel cells. The nitrogenase enzyme is responsible for the reduction of nitrogen (N_2) to ammonia (NH_3), which is a key step in nitrogen fixation required for all life forms.

A principal challenge in studying such redox-active enzymes and enzyme mimics lies in generating a synchronized homogeneous preparation of each transient intermediate state. Under turnover conditions, a mixture of states is typically present, with the population distribution representing the relative energies of the different species. While this provides some useful insight into the energetics of the catalytic process, a detailed structural characterization of each intermediate is critically missing. Thus, the ability to develop molecular systems for energy conversion reactions that are catalyzed by light is therefore critical not only for using sunlight as an energy source but also as an important means to synchronize intermediates for mechanistic pump probe characterization.

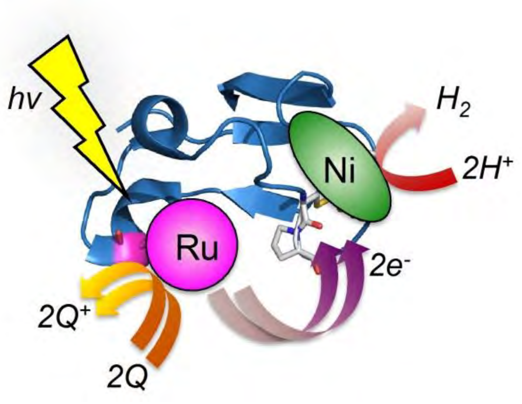

Figure 4.2.7. Schematic for photo-induced hydrogen evolution by Ru-labeled nickel-substituted rubredoxin (NiRd) [13].

It has been recently shown that nickel-substituted rubredoxin (NiRd) is a highly active enzyme for proton reduction both electro-catalytically and in solution, using a low-potential electron donor or a photo-driven assay [14]. A tentative mechanism for hydrogen evolution has been proposed by analogy to what is known about the [NiFe] hydrogenases, for which NiRd is both a structural and functional mimic. However, detailed structural and mechanistic information is needed to optimize the activity and develop increasingly active hydrogen evolution catalysts. The high repetition rate of LCLS-II-HE, combined with pump-probe spectroscopy using XES, RIXS, and EXAFS at the Ni K-edge, (8.3 keV), will provide critical new information.

Recently, a ruthenium-based photo-trigger has been successfully attached to the [NiRd]-hydrogenase protein scaffold using histidine coordination (Figure 4.2.7). Through reductive quenching of the photo-trigger by a sacrificial donor, intramolecular electron transfer between the reduced ruthenium and the nickel center initiates catalysis. Time-resolved, two-color X-ray techniques can be used to selectively interrogate the electronic structure of the nickel active site at each catalytic step while simultaneously following the redox state of the photo-trigger. By varying the site of attachment and the initial driving force for ET, we will be able to advance these studies beyond simple structural information to elucidate the kinetics and thermodynamics of catalysis. Using this approach, we can arrive at a complete understanding of the mechanism of hydrogen evolution by NiRd. As an active-site model, these studies will lay the foundation for analogous studies on the native (NiFe) enzymes [13].

The largest source of fixed nitrogen in the global biogeochemical cycle is the reduction of atmospheric dinitrogen (N_2) to ammonia (NH_3). Almost 80% of our nitrogen intake is produced by the industrial Haber-Bosch process via a dissociative reaction involving co-activation of dihydrogen (H_2) and N_2 over an Fe-based catalyst. The reaction currently generates significant amounts of CO_2 because the H_2 needed for this reaction is presently produced by steam reforming of natural gas. This one process consumes up to 5% of the world's natural gas and about 2% of the world's energy production [15]. Recently it has been reported that cadmium sulfide (CdS) nanocrystals can be used to photosensitize the nitrogenase molybdenum-iron (MoFe) protein. Thus light harvesting by CdS nanocrystals replaces ATP hydrolysis and drives the enzymatic reduction of N_2 into NH_3 [16] (see Figure 4.2.8). A turnover rate corresponding to ~60% of the ATP-coupled reaction rate for the nitrogenase complex under optimal conditions was reported. Thus these CdS:MoFe protein biohybrids provide a photochemical model for achieving light driven N_2 reduction to NH_3.

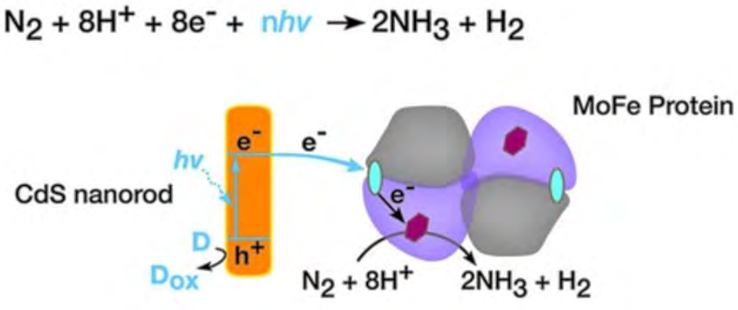

Figure 4.2.8. Reaction scheme for N_2 reduction to NH_3 by CdS:MoFe protein bio-hybrids. The electrons are provided by light-induced charge separation in the CdS nanorod as compared to the natural nitrogenase, where eight electrons are provided by hydrolysis of 16 ATP molecules [16].

The ability to create complexes between nanomaterials and MoFe protein and other enzymes shows that photoexcited electrons can be used to drive difficult catalytic transformations while providing new tools for mechanistic investigations. Hard X-rays at high repetition rates will be a critical tool to study the transient structure and bonding configurations of the active sites of these intermediates. The revolutionary new capabilities of LCLS-II-HE will provide detailed atomic and electronic structure information for these hybrid systems by scattering and spectroscopy methods, in particular XES, RIXS, and EXAFS.

4.2.4 Heterogeneous catalysis and interfacial chemistry

In functioning heterogeneous catalysts, the materials are neither static nor homogeneous. The evolution of atomic and electronic structure, the making and breaking of chemical bonds, and the exchange of vibrational energy through intermediate states ultimately determine functionality. These interactions further lead to dynamic restructuring of catalyst materials during reaction cycles. Knowing the time evolution of the atomic and electronic structure of molecules and substrates, particularly near elusive transition states, is critical to developing a predictive understanding for design of new catalysts.

Today we are unable to develop a complete picture of this structural evolution on the femtosecond to picosecond timescale relevant to atomic motion or the nanosecond to millisecond timescale characteristic of diffusion and materials evolution. LCLS has enabled the study of simple surface reactions, and reported the first observation of a surface transition state [17]. These groundbreaking studies on ideal crystals, with reactants prepared at high concentrations in a vacuum, demonstrate the potential for XFELs to provide a full understanding of chemical reactions on surfaces. However, these studies do not address "working" catalysts which are typically of low dimensionality (*e.g.* nanoclusters of metals on an oxidic support), where coupled fluctuations of the electronic and atomic structure become increasingly important.

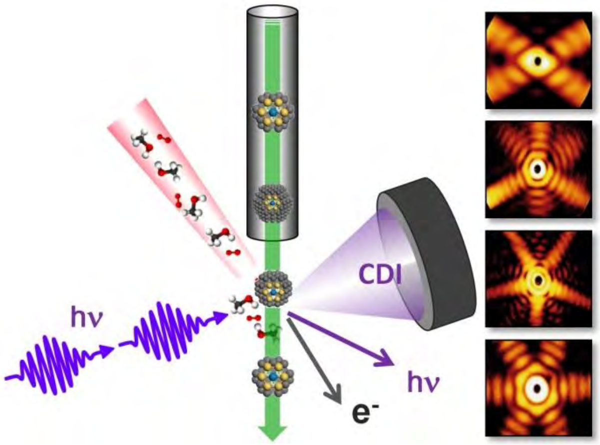

Figure 4.2.9. Left: Serial characterization of heterogeneous nanocatalyst in operation: atomic structure via diffractive imaging (CXI), electronic and chemical structure via photo (or electron) spectroscopy. Right: Characterization of silver nanoparticles via coherent diffractive imaging using an XFEL [18].

LCLS-II-HE will enable completely new approaches for simultaneously following both the atomic and electronic structure of heterogeneous catalysts in operation. One such approach is illustrated in Figure 4.2.9, where nanocatalysts are prepared either with or without pre-adsorbed reactants and interrogated pulse by pulse using a gas-phase jet or liquid particle injector. Ultrafast X-ray spectroscopy (*e.g.* EXAFS, XES, or RIXS) or photoelectron spectroscopy probes the electronic structure and chemical environment, while coherent X-ray diffraction from the same hard X-ray pulse probes the atomic structure. Demonstration experiments in the soft X-ray range at FLASH [18] and at LCLS [19] highlight the promise of this approach for characterizing small heterogeneous ensembles of nanoparticles at the atomic scale using hard X-rays.

Metal nanoparticles on an oxide support are an important class of heterogeneous catalysts and they typically exhibit unique catalytic properties. However, the atomic-level detail of their behavior is poorly understood due in part to their complex, dynamic structure, mediated by interaction with the support. In contrast to bulk materials, nanoscale systems exhibit substantial fluctuations in electronic and atomic structure, with large surface effects that depend on temperature, pressure, local chemical interactions, and other factors of the operational environment, as illustrated in Figure 4.2.10. All measurements made to date are both time- and ensemble-averaged, and mask any fluctuations that may be present, but the experimental concept shown above (Figure 4.2.9) will allow the time-dependent electronic and structural behavior of the nanoparticles to be determined at sub-picosecond timescales. Indeed, EXAFS analysis of such systems by default assumes a static structure, with any deviation in bond length, for example, encompassed by the means square displacement, σ^2 term.

A series of recent papers based on a combination of real-time density functional theory/molecular dynamics simulations, transient coupled-oscillator models, and statistical mechanics has predicted the significance of dynamic structural disorder (DSD) in supported Pt and PtSn nanoclusters at relevant reaction temperatures. Furthermore, the manifestation of DSD in X-ray absorption spectra has been simulated [20-23] (as shown in Figure 4.2.11). Figure 4.2.10 shows a snapshot of the DFT/MD simulation at t = 4 ps and a time-elapsed rendering (TER) at two different temperatures. The "blurriness" characterizes the disorder and mobility of the Pt and Sn in the $Pt_{10}Sn_{10}$ cluster on the γ-Al_2O_3 surface.

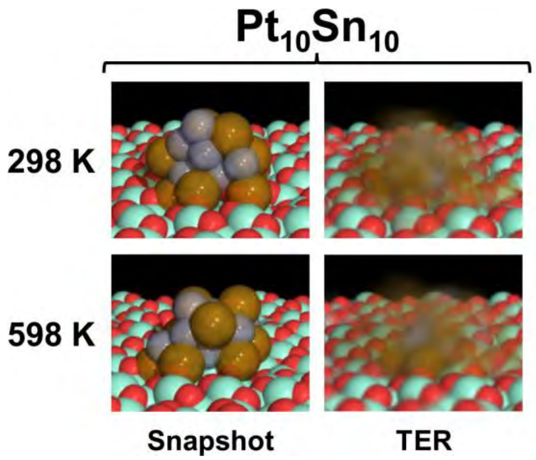

Figure 4.2.10. Snapshot of the DFT/MD simulation of a $Pt_{10}Sn_{10}$ nanoparticle on an γ-Al_2O_3 support at t = 4 and a time elapsed rendering (TER) at two different temperatures. The “blurriness” characterizes the disorder and mobility of the Pt and Sn [21].

Large variations in the white-line intensity can be seen, reflecting substantial differences in the local density of states near the Fermi level, and these variations result from the large structural and bonding fluctuations. LCLS-II-HE will reveal these fluctuations via ultrafast spectroscopy (XES, RIXS, and EXAFS) at the Pt L_3-edge (11.6 keV). The dynamical non-equilibrium nature of the structural fluctuations of the nanoclusters leads to changes in valence charge transfer, which significantly influences the reactivity of the clusters. For example, picosecond fluctuations in the Pt-Sn bonding within a $Pt_{10}Sn_{10}$ cluster supported on alumina affect the electronic structure of the binding site for reactants. This then manifests itself in different local nanoreactivity. Using the dissociation of O_2 as a prototypical example, simulations show that certain configurations result in a lower activation energy for dissociation [22].

With LCLS-II-HE, it will be possible to measure this local heterogeneity and its effect on the binding and dissociation of reactants. The DSD in these nanocatalysts induces additional active sites for reaction pathways, which likely accounts for the increased reaction rate in such catalysts. This in turn will further our understanding of the effects of disorder in nanocatalysts, and allow the design of improved catalysts for specific reaction steps. Moreover, this will make possible a direct investigation of the stability of the nanocatalysts towards sintering. For example, DFT/MD simulations have hinted that there is a “sweet spot” of temperature where the catalytic cluster is internally mobile (quasi-liquid), a regime that likely enhances the catalytic activity but is simultaneously well attached to the support, thus reducing the possibility of deactivation. The range of temperature is very sensitive to the size and composition of the clusters, and also to the nature of the support. Indeed, recent studies at the LCLS have observed transient melting of individual large nanocrystals of gold [24].

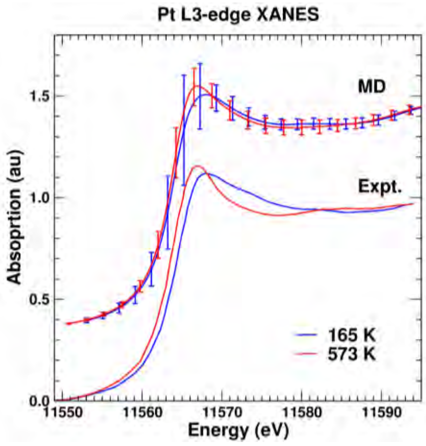

Figure 4.2.11. Comparison of DFT-MD simulations (top curves) and experimental (bottom curves) of the Pt L_3-edge XANES spectra for a Pt_{10} cluster on an alumina support. The theoretical spectra are obtained from a configurational average over all atoms in the cluster for 32 random conformations extracted from the last 5.5 ps of the MD simulation. The error bars on the theoretical calculations indicate the standard deviation of fluctuations between the various configurations.

Another vitally important and industrially relevant class of catalysts is the zeolite-containing catalysts [25]. Zeolites, which are crystalline microporous materials, are primarily used in the oil refining and petrochemical industries. Today, there are 191 different zeotypes identified, many of them synthesized for the first time in the last decade. However, there are still some fundamental questions regarding details of the reaction mechanism in zeolites. One of the most important zeolites is ZSM-5 (MFI framework), which has become ubiquitous in petroleum refining and chemical manufacturing [26, 27]. The detrimental formation of coke is one of the factors limiting the catalytic performance of zeolite materials, particularly ZSM-5, in high-demand catalytic processes, such as fluid catalytic cracking (FCC) and the methanol-to-hydrocarbons (MTH) reaction. However, the molecular-level details of how the coke forms are still not well understood [28, 29].

One powerful new approach to elucidate the material properties that promote the detrimental formation of coke during the MTH reaction on ZSM-5, is to study the elementary reaction steps using excitation pulses in the UV, visible, IR or THz regions, followed by ultrafast X-ray probe pulses that are uniquely available from LCLS-II-HE. Previous attempts to understand the reaction mechanism have used *in situ* fast IR heating of MFI, followed by analysis using UV Raman spectroscopy [30]. However, the constraints of the experiment meant that only long-lived intermediates could be detected. Here we envision a true *in situ* experiment using a scheme like that shown in Figure 4.2.9, where a jet of zeolite crystals is pre-loaded with the reactant of interest, then transiently heated with an IR pulse and probed spectroscopically with X-ray pulses. DFT calculations indicate that there can be up to 8 molecules of ethylene/unit cell [31]. Timescales of picoseconds to milliseconds could be probed using *e.g.* X-ray Raman spectroscopy. Simultaneously, coherent diffraction imaging would provide information on the crystallinity of the zeolite itself and allow correlations to be drawn regarding the size and shape of the zeolite crystal. In addition, X-ray fluorescence imaging could be used to quantify the total amount of carbon in each zeolite crystal. The experiments would be conducted using different reactants (*e.g.* ethylene, propylene, methanol, and higher molecular weight hydrocarbons), and as a function of acid-site strength of the MFI by controlling the Si/Al ratio.

LCLS-II-HE provides a combination of enabling capabilities not available from any other source. First, ultrafast pulses and high peak power from an XFEL are essential for getting useful information from a single pulse. Second, the high repetition rate and uniform pulse structure are ideally suited for pulse-by-pulse measurement and sample replacement. The capability of making 10^8-10^{10} independent measurements per day, combined with advanced data science and computational approaches (as discussed in Section 3.6), opens a tremendous opportunity to characterize inhomogeneous ensembles of nanoparticles and reaction conditions and capture rare catalytic events.

Nanostructured catalysts and interfaces

The study of nanostructured catalysts is an important emerging area that can benefit dramatically from LCLS-II-HE capabilities. Today, nanocrystals can be prepared with atomic precision and are essential components in the preparation of well-defined materials with which to understand catalytic transformations. The use of more uniform nanocrystals (*e.g.* in the approach illustrated in Figure 4.2.9), in combination with LCLS-II-HE, will tremendously improve the data quality and facilitate the statistical analysis of the experiments by controlling structural heterogeneity. The benefits of improved nanocrystal uniformity have been demonstrated in recent X-ray scattering experiments at SSRL, and LCLS-II-HE would drastically improve the data quality. Here the dataset from a highly uniform ensemble could be treated in its entirety using algorithms that dramatically reduce the analysis time. Such approaches applied with LCLS-II-HE will provide access to atomic-scale structural dynamics of an operating ensemble of nanostructured catalysts.

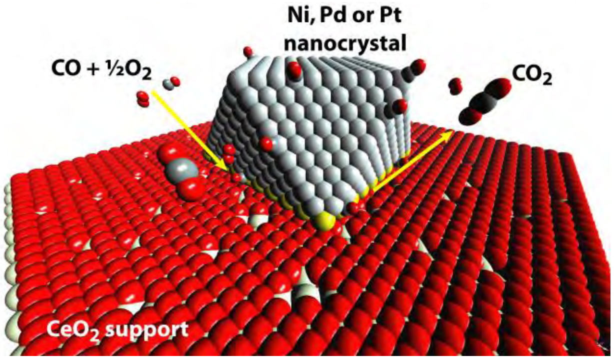

Figure 4.2.12. Illustration of CO oxidation at the interface between an adsorbed metal (Ni, Pd, or Pt) nanoparticle and a support (CeO_2). Enhancement of catalytic reactivity is often attributed to more active sites at the metal-oxide interface, but it can be difficult to quantify this effect [32].

The rapid development of uniform nanostructured catalysts will open an important opportunity to understand "hybrid" systems, *i.e.* multicomponent materials, where two or more components are in contact. Investigations of single crystal surfaces have revolutionized the study of catalytic transformations in the past 40 years, and have enabled the first observation of a transition state during catalytic bond formation using LCLS [17]. It is now well known that the interface region between multiple components forms the basis of many catalytic reaction mechanisms. One example is enhanced CO oxidation observed at the interface between monodisperse metal nanoparticles (Ni, Pt, or Pd) on alumina or ceria, as illustrated in Figure 4.2.12. A second striking example is the supported Au catalysts used in oxidation reactions and water-gas shift-reactions. Au particles less than 5 nm in size become active for reactions such as CO oxidation, but only when they are on a support material. While the importance of the Au/support interface in oxygen and water activation has been recognized, two different chemical intermediates have been proposed: (1) Au-O-O-S (S=support) and (2) Au-O-O-H [33, 34].

Understanding the role of interfaces in catalysis is becoming increasingly important as new tools are developed for both the synthesis and the characterization of this difficult and complex reactive zone. Investigation of these interfaces at the atomic level, and with time resolution to follow structural evolution, will provide new insight into how to combine materials to create more active and selective catalytic materials. Tunable hard X-rays will enable tracking of atomic and electronic structure changes in hybrid catalysts exploiting transition-metal K- and L-edges and advanced time-resolved spectroscopy and scattering techniques (XES, EXAFS, RIXS, XPCS). Sensitivity provided by high repetition rate will be essential to probe the low concentrations of active catalytic sites (*e.g.* on the surface of nanoparticles or at the interface between a nanoparticle and the support). The combination of hard X-ray photon energy and time resolution will allow probing non-equilibrium dynamics of nanoparticles under reactive conditions, and at chemical resonances. Mapping of chemical transformations across timescales, from femtoseconds to milliseconds, will provide an invaluable picture of these interfaces in action. LCLS-II-HE will allow us to uncover how the charge migrates between support materials, particle surfaces, and adsorbed molecules while reactants are being converted – important information to advance our ability to predict and optimize reactivity in catalyst support assemblies.

4.2.5 Charge and ion transfer at solid-liquid interfaces

Heterogeneous chemistry at the liquid-solid interface plays a central role in emerging catalytic processes though electrochemistry. For example, in transforming CO_2 to fuels and nitrogen to ammonia, electrochemical reactions transfer protons from solvated liquid to adsorbed intermediates on the catalytic solid material. The complexity of the solid-liquid interface includes adsorption/desorption, diffusion, solvation/desolvation, and the interaction between solvated and adsorbed species with the dynamical surface geometric and electronic structure. Relevant processes span a wide range of timescales, from slow reorganization of nuclear and solvent coordinates spanning nanoseconds (*e.g.* ligand exchange reaction of aqueous Li^+) to days (*e.g.* Cr^{3+} ion water exchange), to the establishment of transition point configurations (activation), and the subsequent ultrafast electron transfer between the electrode and the reactant molecules/ions, possibly proton-coupled, to slower energy transductions (femtoseconds to picoseconds). In spite of the importance of charge transfer processes in electrochemistry, these solid-electrolyte interfaces remain poorly understood at a fundamental level. Our current understanding is based largely on the empirical electrical double-layer model, which was developed in the mid-19th to mid-20th centuries [35-39].

One important area where interfacial chemistry is central is in ion batteries for energy storage. Here metal cations move from the negative electrode to the positive electrode while discharging, and reverse during the charge cycle. The need for major advances in both energy storage capacity and density is driving numerous innovations in battery design, and further highlights the need for a deeper understanding of the interfacial chemistry at fundamental length and time scales and under operating conditions. One promising approach for achieving higher energy density is to exploit multivalent ions, such as divalent Mg, Ca, or Zn or trivalent Al ions, in place of monovalent Li ions on which present battery technology is based. One drawback, however, is that the high charge density of multivalent ions gives rise to a stiff and organized solvation shell, which acts as a barrier for charging/discharging.

Recent static hard X-ray scattering studies at the Advanced Photon Source (APS), combined with pair-distribution-function (PDF) analysis and MD modeling, have revealed the cation structure for multivalent electrolytes, as illustrated in Figure 4.2.13 [40]. While this highlights the potential for hard X-ray methods to probe electrolyte structure at the atomic scale, our present knowledge is limited to a static description of the solvation shell of the bulk electrolyte. We do not know how the solvation shell evolves along the charging/discharging reaction path, and we lack the sensitivity to probe the dynamic structure in the critical interface region.

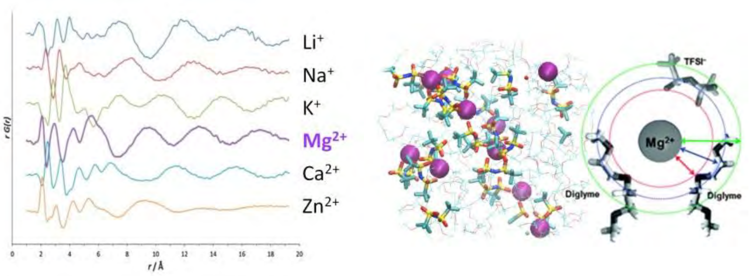

Figure 4.2.13. Solvation structure of electrolytes for multivalent energy storage. *r*-Weighted form of the *d*-PDFs, *r*G(*r*), highlights the well-defined inner-sphere features and broader solvation shells at longer distances. MD simulation showing Mg^{2+} in space-filling format [40].

The expanded photon energy range coupled with the programmable time structure and repetition rate of LCLS-II-HE will provide important new insights into the structural dynamics of relevant electrolytes near the interface region in operating electrochemical cells. Advanced X-ray studies of interfacial chemistry *operando* employ a "dip-pull" apparatus (*e.g.* as developed at the Advanced Light Source for ambient pressure photoemission studies) whereby a thin meniscus forms on a biased electrode pulled from the electrolyte solution to provides access to a nanometer-scale liquid film [41]. Figure 4.2.14 shows a variant of this approach with a rotating anode to provide a continuously-replenished electrolyte film of variable thickness under operating conditions. This approach can be combined with either sequential XPCS techniques, to access longer time scales, or two-pulse XPCS, to access the fastest time scales (see Section 3.3), capturing both the structural re-arrangement and chemical transformation of solid-liquid interfaces with high spatial and spectral resolution.

The tunability of LCLS-II-HE will enable resonant XPCS for chemically selective tracking of structural changes in transition metal and post-transition metal ions, providing an invaluable picture of these electrolyte/electrode interfaces in action. While the chemical species in the electrochemical double layer (few nm thickness) transform upon electrochemical potential change, the bulk electrolyte or electrode composition does not. Signals from the electrochemical interface can be discriminated from bulk electrolyte or electrode by subtractive normalization of measurements between two electrochemical conditions. The time structure of hard X-ray pulses provided by LCLS-II-HE and its unprecedented average brightness are essential for this approach, allowing extraction of small differential scattering signals. Future extension of LCLS-II-HE capabilities to 20 keV and beyond (see Section 6) will enable time-resolved X-ray scattering studies at large $\boldsymbol{q}$ to be combined with PDF analysis to map the local ion structure at the interface, and follow its evolution through changes in operating conditions.

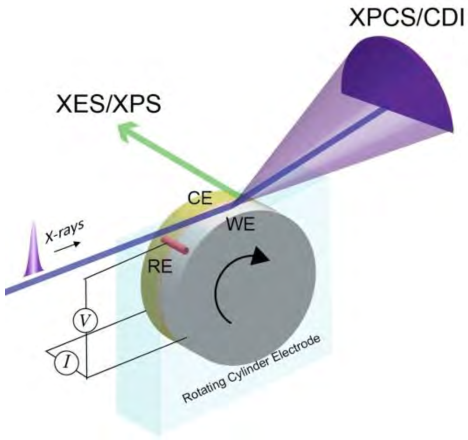

Figure 4.2.14. Schematic of electrochemical cell based on the rotating electrode reactor. The working electrode (WE) and counter cylindrical electrode (CE) are partially emerged from an electrolyte solution. As the cylinder rotates, WE and CE are continuously dipped and pulled from the electrolyte. In the steady state, fresh liquid layers on WE and CE are continuously replenished. The electrochemical potential of WE is referenced to stationary electrode (RE) near the X-ray interaction point. The exposed thickness of the liquid layers on WE and CE can be controlled by the angular velocity of cylinder electrode and the arc length of the exposed part of WE and CE.

4.2.6 Aqueous and interfacial geochemistry: elemental cycling and contaminant mitigation

Natural Earth systems are extremely complex on all length and time scales and are dominated by compositional, structural and temporal heterogeneities, interfaces, and disorder (*e.g.* as illustrated in Figure 4.2.15 and highlighted in the 2015 DOE-BES report [42]). A fundamental understanding of the behavior of geochemical systems across a broad range of time and spatial scales is critical for ensuring the future vitality of ecosystems [43]. Understanding and controlling interfacial chemistry is at the core of this grand challenge. A 2015 BES roundtable report on subsurface technology and basic science [44] emphasized this point, and DOE Energy Frontier Research Centers are investigating molecular-level controls of subsurface reactivity relevant to geologic carbon sequestration and solid-fluid interfaces. LCLS-II-HE capabilities will allow detailed mechanistic and kinetic studies of geochemical reactions on the timescales of bond making and breaking and electron transfer. Such studies will revolutionize our understanding of the mechanisms by which chemical contaminants such as heavy metals, radionuclides, and natural organic matter interact in complex aqueous-solid-gas systems, as described below.

Soils, sediments, and microorganisms are bathed in water or coated with water films. Water is required for microbial metabolism, solute transport, and a vast array of geochemical reactions. Consequently, studies of geochemical processes require techniques that can penetrate water. Because of their penetrating power and ability to access molecular length scales, hard X-rays are the technique of choice for geochemical and environmental studies [45]. Earth materials, including microbial-mineral assemblages, are chemically and physically heterogeneous at length scales down to nanometers. Nanoparticles are abundant as grain coatings and colloids and are often highly reactive. Model systems that will be employed to study dynamics in these systems must reflect this chemical and physical heterogeneity, and many must be wet. Ultrafast X-ray scattering and spectroscopy methods that can operate under dilute, heterogeneous aqueous conditions are required.

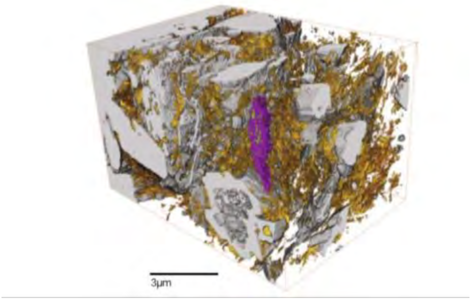

Figure 4.2.15. 3D reconstruction of pore space (yellow), organic matter (purple), and calcite and quartz (grey) in shale, Opalinus clay (from reference 46 reproduced from reference 47).

Within the complex architecture of natural porous media, metals such as Cr, Mn, Fe, and Ti serve as important micronutrients for microbial and plant communities, redox controls), and mineral-forming constituents. Metals and metalloids, including Cr, Co, Cu, Zn, Se, As, Hg, and Pb, may be present as environmental contaminants. The activity of metals in geochemical settings is controlled largely by reactions occurring in aqueous solution and at mineral-water and microbe-water interfaces. In spite of the broad importance of metals and metalloids in the subsurface, ultrafast studies of such geochemical reactions are almost completely lacking.

At hard X-ray energies, XAS and XES offer the ability to penetrate water and, moreover, provide element specificity and high sensitivity (*e.g.*, accessing µM solution concentrations). EXAFS provides quantitative information on local molecular structure, whereas XANES, XES and RIXS enable direct observation of core-to-LUMO/HOMO transitions, which are highly sensitive to chemical bonding. These methods, coupled with LCLS-II-HE capabilities, thus provide the capability to simultaneously follow the evolution of electronic and physical structure under environmentally-relevant conditions (*e.g.* dilute aqueous reactants, nanostructured samples) at sub-picosecond timescales.

Interfacial geochemical dynamics: sorption, desorption, and redox

Surface-mediated, mineral-aqueous solution interface reactions, in which ions are released from solid surfaces into solution via desorption or during chemical weathering reactions, or are removed from solution via sorption reactions, profoundly impact the compositions of natural waters, including oceans, lakes, groundwater, and subsurface brines. Mineral-water interfaces, particularly on iron and manganese oxides and iron sulfides, also strongly catalyze redox reactions that are slow or unmeasurable in aqueous solution. Chemical reactions at solid-liquid interfaces include acid-base (hydrolysis) and surface complexation or adsorption reactions, ligand exchange and electron or ion transfer reactions, dissolution of solids, as well as nucleation and growth of solids in water. The complexity of chemistry at the liquid-solid interface, as visualized in Figure 4.2.16, involves absorption/desorption, diffusion, solvation/desolvation, and the interaction between solvated and adsorbed species with the dynamical surface geometric and electronic structure.

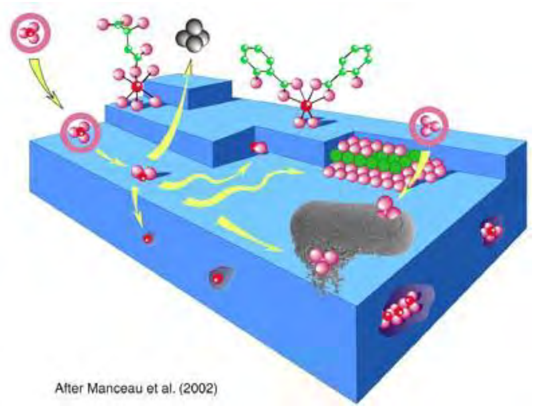

Figure 4.2.16. Interfacial processes involving adsorbate molecules at mineral-water interface: physisorption, chemisorption, detachment, absorption or inclusion, occlusion, attachment, hetero-nucleation, and organo-mineral complexation [48].

Relevant processes span a wide range of timescales, from the slow exchange of water molecules for aqueous ions (about one day), to ligand exchange reactions of ions (~100 ps), to electron-transfer processes (femtoseconds). It is important to address: (i) How the presence, abundance, and types of surface defect sites affects ultrafast mechanisms and rates of metal ion sorption, desorption, and redox processes, (ii) How nanoparticle or nanopore diameter affect mechanisms and rates of these same reactions, and (iii) How electrons are transferred between the bulk and surface species during redox reactions. In order to answer these questions, it will be necessary to comprehensively follow the reaction (bond formation, loss) under *in situ* conditions at interfaces, including loss of waters of solvation, precursor states, bond activation, formation of initial adsorption complexes, and their electronic and physical evolution.

The significance of these issues is illustrated by the problem of interfacial desorption/sorption of Zn^{2+} on iron oxide surfaces. Zinc is an important and widespread environmental contaminant that adsorbs strongly and reversibly to iron oxide nanoparticles (FeOOH), depending on pH and aqueous conditions. LCLS-II-HE capabilities provide a means to directly probe the ultrafast dynamics of the Zn^{2+} desorption processes and characterize the associated stepwise structural and electronic changes.

FeOOH nanoparticles with adsorbed Zn^{2+} (in an aqueous suspension delivered by a liquid jet) can be transiently heated via THz excitation to trigger desorption of the Zn^{2+} in the electronic ground state. Transition state complexes (physical and electronic structure) and their lifetimes can be characterized via time-resolved XANES and XES to capture the breaking of Zn^{2+}-surface oxygen bonds and the formation of inner-sphere solvation shells around Zn^{2+}. Time-resolved EXAFS will detect changes in Zn-Fe and Zn-O pair correlations. The Zn^{2+} first coordination shell exhibits both tetrahedral and octahedral geometries that are relatively easy to resolve in XAS spectra and are stabilized by changes in the local bonding environment, providing additional ways to probe surface dynamics.

Since such studies require low sorption densities of Zn^{2+}, a high average flux of tunable X-rays (in the Zn K-edge region, ~9.7 keV) will be essential to extract small differential signals. Comprehensive studies as a function of particle size, pH, ionic strength, and complexing ligands will transform our understanding of adsorption-desorption processes and the interplay between adsorbate chemistry and surface structure.

Aqueous-phase geochemical dynamics: redox, rates, and isotope fractionation

Complexation and redox reactions occurring in aqueous solutions control the transport of contaminants, the bioavailability of nutrients required for primary productivity, and ecosystem resilience to climate change. Moreover, aqueous systems provide valuable models to help understand more complicated interfacial reactions. Our ability to understand the dynamics of aqueous-phase metal reactions rests on insights gained from observing stepwise component processes at shorter time and length scales. The binding of common geochemical complexing ligands, such as bicarbonate, silicate, or acetate anions or more complex dissolved organic matter, alters access of the reductants and other reactive species to metal centers and thus modifies the pathway and rates of reaction. We need to consider: (i) The molecular structures (physical and electronic) and compositions of intermediates of reactions involving aqueous metal ions, particularly in multi-electron redox transformations, (ii) The structures and compositions of the transition state complexes, and (iii) The lifetimes of intermediates and transition states.

Redox control over the environmental behavior of the common contaminant Cr, which is slightly soluble in its reduced form, Cr(III), but is highly soluble, mobile, and carcinogenic when present as Cr(VI), provides an important example. Mass-dependent fractionation of Cr isotopes arising from redox transitions are of intense interest for their ability to indicate chromium reduction in the subsurface due to remediation of contaminated sites or natural attenuation by native reductants. Crucially, these signatures depend upon the specific structural and electronic transitions involved in the overall reaction, because the rate-determining step (*e.g.*, either electron transfer between or the change in coordination from tetrahedral Cr(VI) and Cr(V) to octahedrally coordinated Cr(IV)) determines the magnitude of the intrinsic fractionation.

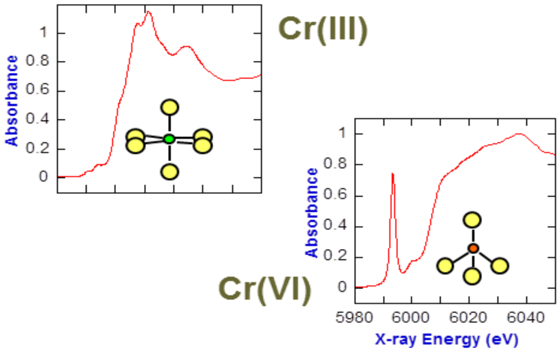

Figure 4.2.18. Chromium XANES and local structures.

We envision a series of LCLS-II-HE experiments that will significantly advance our understanding of this problem. The goal is to understand the pico- and sub-picosecond physical/electronic structures and lifetimes of transition states in the Cr(III) ↔ Cr(VI) redox transition. Chromium is well suited to this study because XANES spectra (at the Cr K-edge, 5.99 keV) are rich in absorption features, providing high contrast between different oxidation states and electronic structures (Figure 4.2.18). Since aqueous chromium can be photo-oxidized or photo-reduced by visible light, visible laser pulses can be used to initiate oxidation state changes in aqueous liquid jets containing either Cr(III) or Cr(VI) over a range of relevant concentrations. Time-resolved XAS and XES measurements at LCLS-II HE will be used to characterize the transition state complexes and their lifetimes. We anticipate that, after the initial electron transfer reaction, Cr oxidation states may return to the original oxidation state, which would enable studies of the reverse reaction. Knowledge gained from such studies will significantly advance our understanding of chemical controls over isotope fraction factors and, in turn, the evolution of Earth's environments, past and present.

References

1. S. E. Canton*, et al.*, "Visualizing the non-equilibrium dynamics of photoinduced intramolecular electron transfer with femtosecond X-ray pulses", *Nat Commun,* **6**, 6359 (2015).

2. W. Zhang, *et al.*, "Tracking excited-state charge and spin dynamics in iron coordination complexes", *Nature,* **509**, 345 (2014).
3. P. Wernet, *et al.*, "Orbital-specific mapping of the ligand exchange dynamics of Fe(CO)$_5$ in solution", *Nature,* **520**, 78 (2015).
4. M. W. Mara, *et al.*, "Electron Injection from Copper Diimine Sensitizers into TiO$_2$: Structural Effects and Their Implications for Solar Energy Conversion Devices", *J. Am. Chem. Soc.,* **137**, 9670 (2015).
5. T. C. B. Harlang, *et al.*, "Iron sensitizer converts light to electrons with 92% yield", *Nature chemistry,* **7**, 883 (2015).
6. M. Cargnello, *et al.*, "Engineering titania nanostructure to tune and improve its photocatalytic activity", *PNAS,* **113**, 3966 (2016).
7. F. G. Santomauro, *et al.*, "Femtosecond X-ray absorption study of electron localization in photoexcited anatase TiO$_2$", *Scientific Reports,* **5**, 14834 (2015).
8. M. Zhang, M. de Respinis, and H. Frei, "Time-resolved observations of water oxidation intermediates on a cobalt oxide nanoparticle catalyst", *Nat Chem,* **6**, 362 (2014).
9. M. Suga, *et al.*, "Native structure of photosystem II at 1.95 Å resolution viewed by femtosecond X-ray pulses", *Nature,* **517**, 99 (2015).
10. J. Kern, *et al.*, "Simultaneous Femtosecond X-ray Spectroscopy and Diffraction of Photosystem II at Room Temperature", *Science,* **340**, 491 (2013).
11. C. Kupitz, *et al.*, "Serial time-resolved crystallography of photosystem II using a femtosecond X-ray laser", *Nature,* **513**, 261 (2014).
12. W. Lubitz, E. J. Reijerse, and J. Messinger, "Solar water-splitting into H$_2$ and O$_2$: design principles of photosystem II and hydrogenases", *Energy & Environmental Science,* **1**, 15 (2008).
13. O. A. Zadvornyy, *et al.*, "Photo-induced H$_2$ production by [NiFe]-hydrogenase from T. roseopersicina covalently linked to a Ru(II) photosensitizer", *J. Inorg. Biochem.,* **106**, 151 (2012).
14. J. W. Slater, and H. S. Shafaat, "Nickel-Substituted Rubredoxin as a Minimal Enzyme Model for Hydrogenase", *The Journal of Physical Chemistry Letters,* **6**, 3731 (2015).
15. S. K. Ritter, "The Haber-Bosch Reaction: An Early Chemical Impact On Sustainability", *Chem. and Engin. News,* **86**, cover story (2008).
16. K. A. Brown, *et al.*, "Light-driven dinitrogen reduction catalyzed by a CdS:nitrogenase MoFe protein biohybrid", *Science,* **352**, 448 (2016).
17. H. Öström, *et al.*, "Probing the transition state region in catalytic CO oxidation on Ru", *Science,* **347**, 978 (2015).
18. I. Barke, *et al.*, "The 3D-architecture of individual free silver nanoparticles captured by X-ray scattering", *Nat Commun,* **6**, 6187 (2015).
19. N. D. Loh, *et al.*, "Fractal morphology, imaging and mass spectrometry of single aerosol particles in flight", *Nature,* **486**, 513 (2012).
20. F. Vila, *et al.*, "Dynamic structure in supported Pt nanoclusters: Real-time density functional theory and x-ray spectroscopy simulations", *Phys. Rev. B,* **78**, 121404 (2008).
21. F. D. Vila, *et al.*, "Operando Effects on the Structure and Dynamics of PtnSnm/γ-Al2O3 from Ab Initio Molecular Dynamics and X-ray Absorption Spectra", *The Journal of Physical Chemistry C,* **117**, 12446 (2013).
22. J. J. Rehr, and F. D. Vila, "Dynamic structural disorder in supported nanoscale catalysts", *The Journal of Chemical Physics,* **140**, 134701 (2014).
23. F. D. Vila, *et al.*, "Molecular Dynamics Simulations of Supported Pt Nanoparticles with a Hybrid Sutton–Chen Potential", *The Journal of Physical Chemistry C,* **120**, 14883 (2016).
24. J. N. Clark, *et al.*, "Imaging transient melting of a nanocrystal using an X-ray laser", *PNAS,* **112**, 7444 (2015).
25. S. Kulprathipanja, ed. *Zeolites in Industrial Separation and Catalysis* (Wiley-VCH Verlag GmbH & Co. KGaA, 2010).
26. W. Vermeiren, and J.-P. Gilson, "Impact of Zeolites on the Petroleum and Petrochemical Industry", *ToCat,* **52**, 1131 (2009).
27. E. T. C. Vogt, *et al.*, "Chapter Two - Zeolites and Zeotypes for Oil and Gas Conversion," in *Advances in Catalysis*, C. J. Friederike, ed. (Academic Press, 2015), pp. 143.
28. J. P. Hofmann, *et al.*, "Large Zeolite H-ZSM-5 Crystals as Models for the Methanol-to-Hydrocarbons Process: Bridging the Gap between Single-Particle Examination and Bulk Catalyst Analysis", *Chemistry – A European Journal,* **19**, 8533 (2013).

29. D. Mores, *et al.*, "Space- and Time-Resolved In-situ Spectroscopy on the Coke Formation in Molecular Sieves: Methanol-to-Olefin Conversion over H-ZSM-5 and H-SAPO-34", *Chemistry – A European Journal,* **14**, 11320 (2008).
30. P. M. Allotta, and P. C. Stair, "Time-Resolved Studies of Ethylene and Propylene Reactions in Zeolite H-MFI by In-Situ Fast IR Heating and UV Raman Spectroscopy", *ACS Catalysis,* **2**, 2424 (2012).
31. F. Jianfen, *et al.*, "Molecular dynamics simulation of ethene diffusion in MFI and H[Al]ZSM-5", *Journal of Molecular Structure: THEOCHEM,* **492**, 133 (1999).
32. M. Cargnello, *et al.*, "Control of Metal Nanocrystal Size Reveals Metal-Support Interface Role for Ceria Catalysts", *Science,* **341**, 771 (2013).
33. J. Saavedra, *et al.*, "The critical role of water at the gold-titania interface in catalytic CO oxidation", *Science,* **345**, 1599 (2014).
34. I. X. Green, *et al.*, "Spectroscopic Observation of Dual Catalytic Sites During Oxidation of CO on a Au/TiO2 Catalyst", *Science,* **333**, 736 (2011).
35. H. Helmholtz, "Ueber einige Gesetze der Vertheilung elektrischer Ströme in körperlichen Leitern mit Anwendung auf die thierisch-elektrischen Versuche", *AnP,* **165**, 211 (1853).
36. M. Gouy, "Sur la constitution de la charge électrique à la surface d'un électrolyte", *J. Phys. Theor. Appl.,* **9**, 457 (1910).
37. D. L. Chapman, "LI. A contribution to the theory of electrocapillarity", *Philosophical Magazine Series 6,* **25**, 475 (1913).
38. O. Stern, "Zur theorie der elektrolytischen doppelschist", *Zeitschrift fur Elektrochemie,* **30**, 508 (1924).
39. D. C. Grahame, "The Electrical Double Layer and the Theory of Electrocapillarity", *Chem. Rev.,* **41**, 441 (1947).
40. S. H. Lapidus, *et al.*, "Solvation structure and energetics of electrolytes for multivalent energy storage", *PCCP,* **16**, 21941 (2014).
41. S. Axnanda, *et al.*, "Using "Tender" X-ray Ambient Pressure X-Ray Photoelectron Spectroscopy as A Direct Probe of Solid-Liquid Interface", *Scientific Reports,* **5**, 9788 (2015).
42. J. C. Hemminger, "Challenges at the Frontiers of Matter and Energy: Transformative Opportunities for Discovery Science - BESAC Report U.S. D.O.E.," (http://science.energy.gov/~/media/bes/besac/pdf/Reports/CFME_rpt_print.pdf, 2015).
43. D. DePaolo, "Basic Research Needs for Geosciences: Facilitating 21st Centrury Energy Systems - BESAC Report U.S. D.O.E.," (http://science.energy.gov/~/media/bes/pdf/reports/files/Basic_Research_Needs_for_Geosciences_rpt.pdf, 2007).
44. L. Pryak-Nolte, and D. DePaolo, "Controlling Subsurface Fractures and Fluid Flow: A Basic Research Agenda - BES Report U.S. D.O.E.," (http://energy.gov/sites/prod/files/2016/01/f28/BES%20Report%20Controlling%20Subsurface%20Fractures%20and%20Fluid%20Flow.pdf, 2015).
45. G. E. Brown, and N. C. Sturchio, "An Overview of Synchrotron Radiation Applications to Low Temperature Geochemistry and Environmental Science", *Reviews in Mineralogy and Geochemistry,* **49**, 1 (2002).
46. L. M. Keller, *et al.*, "Pore space relevant for gas permeability in Opalinus clay: Statistical analysis of homogeneity, percolation, and representative volume element", *Journal of Geophysical Research: Solid Earth,* **118**, 2799 (2013).
47. J. Zachara, *et al.*, "Internal Domains of Natural Porous Media Revealed: Critical Locations for Transport, Storage, and Chemical Reaction", *Environ. Sci. Technol.,* **50**, 2811 (2016).
48. A. Manceau, M. A. Marcus, and N. Tamura, "Quantitative speciation of heavy metals in soils and sediments by synchrotron X-ray techniques," in *Applications of Synchrotron Radiation in Low-Temperature Geochemistry and Environmental Science*, P. Fenter, M. Rivers, N. C. Sturchio, and S. Sutton, eds. (Reviews in Mineralogy and Geochemistry, Mineralogical Society of America, Washington, D.C., 2002), pp. 341.

4.3 Imaging Biological Function and Structural Dynamics

Understanding the atomic-scale structure, structural dynamics, and conformational landscape of macromolecular complexes and assemblies, in physiologically relevant environments, is an important frontier for both biology and nanomaterial self-assembly. Understanding the function of a biological molecule or assembly starts with knowledge of the structure of its constituent components. For decades, function has been inferred from such static structures obtained primarily from crystallographic measurements. This powerful method has been complemented by the capabilities of LCLS and will be further enhanced by LCLS-II and LCLS-II-HE. However, functioning biological systems are not static, and probes of structural dynamics are essential to reach a deeper understanding the function of macromolecular complexes and nanomachines whose structures change over a range of time and length scales, often in response to changes in local environment (temperature, pH) or interaction with small molecules or other external stimuli. Here, LCLS-II-HE will have significant impact by enabling comprehensive studies at fundamental time and length scales and under operating conditions or native environments (*e.g.* aqueous, room temperature). The high repetition rate of LCLS-II-HE, combined with the high photon energy consistent with the high-resolution necessary to understand dynamics at the atomic level, will provide paradigm-changing capabilities for the field of structural biology.

LCLS-II-HE is the ideal, much desired upgrade to LCLS that the structural biology community requires. The combination of high spatial and time resolution with a high repetition rate will make LCLS-II-HE a revolutionary machine for many biological science fields. The expected impact of LCLS-II-HE in elucidating the structure and function of molecules is described below.

4.3.1 Imaging biological structures via crystallography

The X-ray FEL methods of femtosecond crystallography (FX) and more specifically serial femtosecond crystallography (SFX) are now well-known and have had a significant impact on the field of structural biology since the beginning of LCLS and SACLA operations [1-8]. An overarching advantage of XFEL crystallography approaches is the ability to avoid radiation damage via ultrafast measurements – "diffraction before destruction" [9]. This in turn enables high-resolution structural determination from very small crystals (<1 μm) that are not suitable for synchrotron crystallography methods, and has further resulted in significant advances in resolution for classes of crystals that are particularly damage sensitive (*e.g.* metalloproteins and transmembrane proteins such as the G-protein coupled receptors) [8, 10, 11]. LCLS-II-HE will have a dramatic scientific impact – providing structures of large classes of molecules at high resolution enabled by hard X-ray pulses at high repetition rates.

High-throughput nanocrystallography

Our ability to sequence the complete DNA set of an organism – the revolution in genomics – exceeds the growth rate of Moore's Law (*i.e.* transistor density of integrated circuits doubling every 18 months). Currently, the number of sequenced proteins doubles roughly every nine months. This explosion in genomic information dramatically outpaces our ability to determine the basic structure of these proteins. Moreover, understanding the function of these proteins requires structural studies in many contexts (local environment, response to substrates, dynamics etc.). In addition, ~50% of all drug targets are membrane proteins, yet few structures of these important proteins are available due to the challenges associated with crystallizing them. While SFX with nanocrystals mitigates many historical challenges for crystallographers (*e.g.* producing large well-ordered crystals, avoiding radiation damage) the scientific impact SFX will have on biology will be limited unless a meaningful level of throughput can be achieved. LCLS-II-HE capabilities will dramatically advance the throughput for protein structural studies under ambient conditions and for very small crystals, (*e.g.* with much more rapid data collection compared to micro electron diffraction [12]) and provides a foundation for even greater growth in the future. This will make XFEL structural methods high-impact tools for new structural biology.

Metalloprotein crystallography

A large fraction of proteins and enzymes exploit metal centers for essential catalytic functions ranging from photosynthesis (which accounts for all the oxygen in the biosphere) and nitrogen fixation (the principal source of nitrogen in soil). Understanding the function of metalloenzymes is of profound importance not only for biology, but for bio-inspired catalysts for fuels production (as discussed in Section 4.2). While as much as 6% of the macromolecular structures in the protein data bank (PDB) contain Fe atoms, it is quite likely that many, if not most, are inaccurate as for the details of the metal ion active sites. Metalloproteins with reducible metal ion active sites are notoriously prone to radiation damage by photoreduction, which alters the structure and limits the resolution that can be obtained (or sometimes inhibits structural determination of the active site altogether). At the same time, the precise electronic and geometric structure of the metal center is necessary for a detailed understanding of its role in facilitating the chemical reaction. This major knowledge gap presents a significant barrier to understanding how metalloenzymes efficiently catalyze reactions – typically with Earth-abundant elements and under ambient conditions.

Section 4.2.3 focused on spectroscopy studies of solution-phase metalloprotein dynamics, and unique approaches for preparing and probing transient intermediate states through hybrid assemblies that can be triggered by light. Such approaches are in principle also amenable to crystallography studies in which high-throughput SFX methods enabled by LCLS-II-HE can provide atomic resolution without damage and at room temperature (near native environments). In addition, these methods will be applicable to rare samples (*e.g.* human proteins) which cannot be studied at present 120 Hz rates due to the large sample volumes required. Furthermore, the energy range of LCLS-II-HE will access the absorption K-edges of key 3*d* transition metals that are beyond the reach of LCLS-II. This can be exploited to minimize damage, enhance contrast for the metal centers and provide for phasing via anomalous scattering. Simultaneous diffraction and X-ray absorption and/or emission spectroscopy studies will probe the structure of the molecule and the local electronic states of target atoms (as described in Section 4.2) to provide new insights into enzyme function.

Examples of important metalloproteins abound, with many still to be studied. One example is nitrogenase which converts atmospheric dinitrogen (N_2) into a bioavailable form, ammonia (NH_3), and is the only known enzyme capable of performing this energetically difficult multi-electron reduction. Understanding how this conversion is accomplished is of high importance for the production of ammonia (as fertilizer), for energy efficiency (as industrial processes to produce ammonia consumes enormous amounts of energy), and ultimately for global warming.

Nitrogenase consists of two component metalloproteins, the iron (Fe)–protein (Av2) and the molybdenum-iron (MoFe)–protein (Av1). The Fe-protein mediates the adenosine triphosphate (ATP)–dependent electron transfer to the MoFe-protein to support dinitrogen reduction. To achieve the elaborate redox properties required for reducing the N–N triple bond, two metal centers are present in the MoFe-protein: The P-cluster and the FeMo-cofactor. The P-cluster is the initial acceptor for electrons, donated from the Fe-protein during complex formation between the two proteins. Electrons are subsequently transferred to the FeMo-cofactor (Figure 4.3.1) that constitutes the active site for substrate reduction. This is the most complex metal center known in biological systems, and we have only a limited understanding of how it functions. Even the fundamental question of whether molybdenum or iron represents the site for substrate binding still under debate, and as a consequence, a variety of mechanistic pathways have been proposed based on either molybdenum or iron as the catalytic center.

Substrates and inhibitors bind only to forms of the MoFe-protein reduced by two to four electrons relative to the resting, “as-isolated” state, which can be generated only in the presence of reduced Fe-protein and ATP. Mechanistic studies must take into account the dynamic nature of the nitrogenase system, which requires multiple association and dissociation events between the two component proteins, as well as the ubiquitous presence of protons that are reduced to dihydrogen (H_2) even in competition with other substrates. The resulting distribution of intermediates under turnover conditions complicates the structural and spectroscopic investigation of substrate interactions.

A recent static crystallography study at SSRL presented the first structure with a substrate or inhibitor bound to the active site of nitrogenase [13]. The structure reveals a CO molecule bridging Fe2 and Fe6 of the FeMo-cofactor. The binding geometry is achieved by replacing a “belt-sulfur” atom (S2B) and highlights the generation of a reactive iron species uncovered by the displacement of sulfur. The CO inhibition is fully reversible as established by resumption of enzyme activity and reappearance of S2B in the 1.43 Å resolution structure determined from crystals of the reactivated enzyme. The substantial and reversible reorganization of the FeMo-cofactor accompanying CO binding was unanticipated and provides insights into a catalytically competent state of nitrogenase.

The damage-limiting capabilities of LCLS-II-HE combined with SFX capabilities to study dynamics in near-native environments at room temperature will prove invaluable for advancing our understanding of the complex dynamics of metal-containing systems such as nitrogenase. Moreover, unique approaches for preparing and probing transient intermediate states of enzymes through hybrid assemblies that can be triggered by light (as discussed in Section 4.2.3) will transform this field.

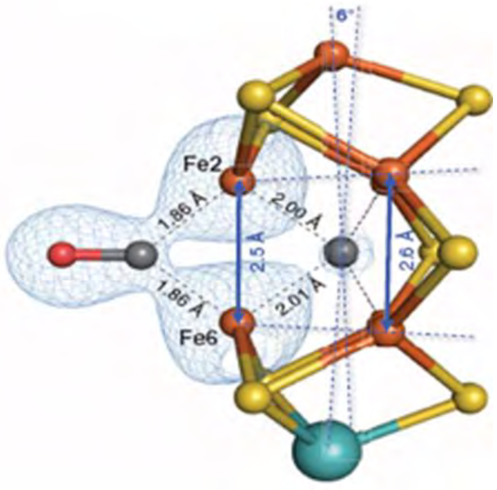

Figure 4.3.1. Side view of the active site of the nitrogenase FeMo-cofactor (a [7Fe:9S:C:Mo]-R-homocitrate cluster), showing the binding of CO (left) replacing a sulfur atom of the cofactor. The electron density (blue) contoured at 1.5 σ is shown for the CO substrate and two Fe atoms of the cofactor [13].

De novo phasing

Because of the limited damage from ultrashort X-ray pulses, LCLS-II-HE has tremendous potential to become a powerful tool to solve truly novel structures of very important, extremely challenging samples. Realizing this potential will require robust *de novo* phasing methods whereby the phases of the XFEL diffraction patterns are obtained directly – typically by exploiting the anomalous scattering from specific atoms. The most common approach is Se-based anomalous phasing [14], near the Se K-edge at 12.6 keV, although other elements have been successfully used at LCLS and at SACLA [15-17]. The high-resolution typically desired for structural determination favors hard X-rays, and many of the elements used for phasing, including Se, require the higher photon energy range provided by LCLS-II-HE.

Results to date from *de novo* phasing using XFELs demonstrate that large data redundancy is required to achieve the necessary signal-to-noise for phasing. This precludes the application of these methods on the most important samples that must be solved *de novo*: novel and rare proteins which are not available in sufficient quantities to study at 120 Hz. LCLS-II-HE will eliminate this restriction and enable new biological science by minimizing sample waste while accessing high energies up to the Se K-edge or beyond for routine *de novo* phasing.

4.3.2 Novel analysis methods

Structure from imperfect crystals

Recent advances in the analysis of diffraction patterns, particularly XFEL scattering data, are opening entirely new paths to solve the structures of crystals previously thought to be of insufficient quality. These approaches exploit the diffuse scattering between and beyond the Bragg peaks, which for certain types of crystalline disorder can be representative of the Fourier transform of a single molecule. For example, if all unit cells are identical and identically oriented in a crystal, but the lattice periodicity is not perfect, then the Bragg intensities will be extinguished at relatively low resolution. Nevertheless, there will still be diffuse scattered X-ray intensity at higher resolutions, which will represent the scattering of a single molecule, scaled in intensity by the number of molecules illuminated and by the degree of crystalline disorder [18]. Analysis of this diffuse scattering enables higher resolution structures to be extracted from previously discarded crystals.

Continuous diffraction bridges the gap between crystallographic and single particle imaging methods. It not only provides the potential for increased resolution but can also offer a direct method for phasing and therefore provide access to novel structures. The high repetition rate of LCLS-II-HE will be crucial to enabling such work, and related direct-phasing approaches based on extended intensity profiles between Bragg peaks [19], by providing the greater data redundancy and tremendous enhancement of signals required for these methods.

The continuous diffraction method will also be of great importance for dynamic studies where enhanced resolution can potentially be achieved. The high repetition rate of LCLS-II-HE in this case will provide the necessary rapid data collection that will allow all relevant time scales to be probed with sufficient data quality and quantity for structural and dynamic interpretation.

Biological function and energy landscapes from heterogeneous ensembles and large data sets

While crystallography is an extremely powerful tool for elucidating atomic structures, many complex biological machines defy crystallization due to weak interactions among constituent components and their intrinsic flexibility. Fluctuation X-ray scattering and single particle imaging (SPI) can provide alternative paths towards understanding dynamics of non-crystalline samples at low to medium resolution. Single particle imaging [9, 20, 21] continues to evolve toward higher resolution along the paths defined in the LCLS SPI roadmap [22]. It will benefit greatly from LCLS-II-HE by exploiting both high-peak-power and high-repetition-rate pulses in the hard X-ray regime to achieve better resolution combined with complete data sets to characterize inhomogeneous ensembles of particles.

Fluctuation scattering [23-26] is an ensemble scattering approach enabled by the combination of ultrafast X-ray pulses and high repetition rate. It potentially provides ~100 times more information than conventional SAXS – sufficient for 3D reconstruction of molecular assemblies in solution. It has emerged as a method bridging SPI and crystallography, and is potentially powerful for understanding dynamics and protein interactions in native environments.

For both fluctuation scattering and SPI, the ability to collect 10^8-10^{10} scattering patterns per day with high-intensity pulses in the 5-12 keV range holds tremendous promise. By exploiting revolutionary advances in data science (*e.g.* Bayesian analysis, pattern recognition, manifold maps, and machine learning algorithms as described in Section 3.6) it should be possible to characterize heterogeneous ensembles of particles, capture rare transient events, map energy landscapes and create conformational movies of biological machines at different stages in their work cycle [27] from comprehensive data sets of X-ray scattering patterns.

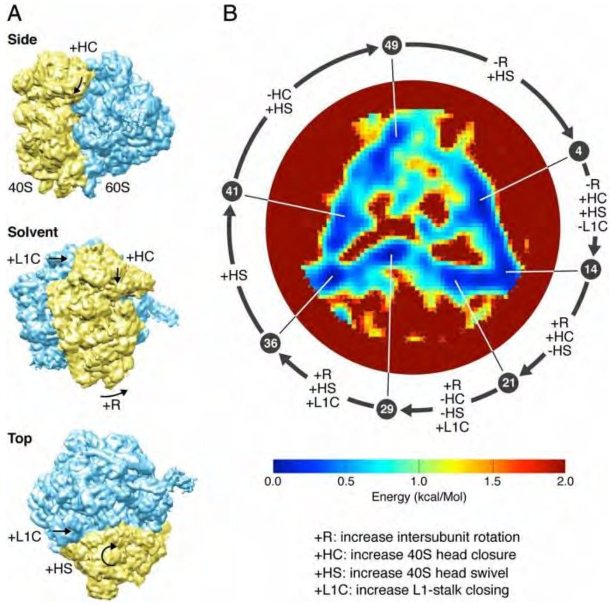

Figure 4.3.2. (A) Three views of a cryo-EM map of the 80S ribosome from yeast, with arrows indicating four key conformational changes associated with the elongation work cycle of the ribosome. (B) The energy landscape traversed by the ribosome. The color bar shows the energy scale. The roughly triangular minimum-free-energy trajectory is divided into 50 states. The arrows indicate the structural changes between seven selected states, each identified by its place in the sequence of 50 states.[28]

A recent example from cryo-EM highlights the potential for extracting three-dimensional structure [29], conformational movies, and energy landscapes from experimental ultralow-signal snapshots of biological entities viewed in unknown orientations at unknown points in their work cycle [28] (Figure 4.3.2). Biological machines function under severe Brownian bombardment, and no single observation is fully reproducible. Reliable information necessitates averaging over homogeneous (*i.e.* sorted) ensembles. The richness of a conformational movie and the detail with which an energy landscape can be mapped depend critically on the number of available snapshots [28].

It is well established that detailed structural information can be recovered from snapshots with extremely low signal. Three-dimensional structure, conformational movies, and energy landscapes can be extracted from image snapshots with signal-to-noise ratios as low as 0.06 [28-30]. Comparable capability has been demonstrated for simulated [30-33] and experimental diffraction snapshots containing as few as 10 diffracted photons per frame [34]. In contrast, current experimental diffraction snapshots of large viruses contain millions of scattered photons from the object of interest [35]. However, substantial shot-to-shot variations in extraneous factors – such as scattering from apertures and particle injectors, as well as difficult-to-control detector nonlinearities – severely degrade the available information [36]. Developments in the source, optics and instrumentation to fully utilize LCLS-II-HE have the potential to reduce such extraneous variations to levels small compared with the (conformational) signal from the object.

The enhanced repetition rate of LCLS-II-HE, combined with improvements in shot-to-shot uniformity in the incident illumination and detector response, can be expected to revolutionize our ability to obtain molecular movies of biological machines at physiological temperatures, and the energy landscapes traversed in the course of biological function.

4.3.3 Imaging biological dynamics: Photo-triggering, heterogeneity and native environments

A new regime of time-resolved protein crystallography was recently demonstrated at LCLS [37, 38], with many more examples under analysis. These results illustrate the potential of dynamic pump-probe structure studies, and further highlight the need for hard X-rays at much higher repetition rate.

Photoactive Yellow Protein (PYP) is a well-characterized model system to study isomerization reactions in macromolecules. It enters a reversible photocycle upon excitation of its chromophore using photons in the blue range of the visible spectrum. The photocycle has a rich set of intermediate states, some with large atomic displacements. The chromophore remains in an excited state for a few hundred femtoseconds and it is believed that the excited state dynamics drive the change from *trans* to *cis*. Such isomerization reactions are important in a wide range of chemical reactions and constitute the first step in vision [39-41] for example.

LCLS was used to observe isomerization in PYP at simultaneous high spatial (1.6Å) and temporal resolution (~150 fs). Structural changes are observed at the earliest time point of 142 fs in the electron density difference map (Figure 4.3.3). Here, the use of small crystals in a flowing jet at room temperature allows for much more uniform illumination of the sample, minimizes group velocity mismatch between the laser and the X-ray pulses for improved time resolution, and provides a fresh sample for every pulse. Such experiments are only possible with an XFEL source. Hard X-rays at much higher repetition rate are essential to realize the full potential of this approach – to provide a complete time sequence of protein dynamics, applicable to a broad range of complexes, and for direct comparison with atomic-scale molecular dynamics models.

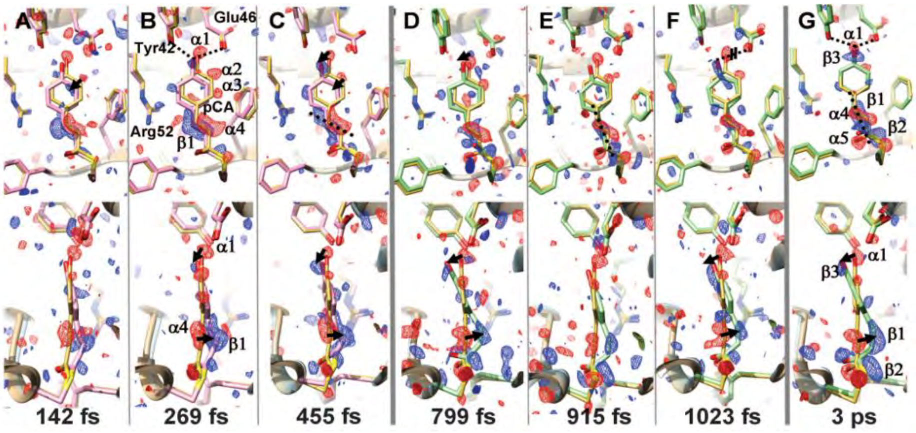

Figure 4.3.3. Snapshot of the structural changes in PYP following photoexcitation. The first three time points show a twisted *trans* state beginning to change while the next three show an early *cis* conformation, with the isomerization compete after 3 ps. The C=C double bond is shown in a dotted line in G [38].

Structural dynamics of phytochrome signal transduction proteins

Phytochromes are representative of an important class of photo-triggered dynamics in biology where LCLS-II-HE capabilities will provide a qualitative advance in our understanding. Phytochromes (Figure 4.3.4) are part of a large family of red-light-sensing kinases that control diverse cellular functions in bacteria and higher plants [42]. Interconversion between a red-absorbing conformation (P_r) and a far-red absorbing conformation (P_{fr}) initiates signal amplification and transduction, and is initiated by rapid photoisomerization of the C_{15}-C_{16} bridge of the bilin prosthetic group. At present, there lacks a complete understanding of the mechanisms and structural dynamics that link the local isomerization event, on the sub-picosecond timescale [43], to large-scale conformational changes (on timescales spanning ns to msec) that ultimately connect to the cellular signaling network that mediates gene expression and influences growth and development. This is illustrative of a large class of biological systems where atomic-scale changes in bonding rapidly lead to nm-scale conformational signals and biological reactions (as further underscored by recent studies of “protein quakes” at LCLS using solution scattering [44, 45]) and crystallography [37]. Understanding such processes in nature will inform biomimetic design of robust and efficient artificial systems for light harvesting, sensing, and energy storage.

Time-resolved serial femtosecond crystallography (SFX) exploiting the high repetition rate of LCLS-II-HE will provide the first mapping of the atomic-scale structural dynamics occurring on femtoseconds to picoseconds timescales, and beyond. While the large conformational changes in phytochromes and related proteins tend to inhibit crystallography approaches to understand the structural dynamics, X-ray FELs have demonstrated a unique ability to probe nanocrystals at room temperature that can accommodate a much wider range of conformational changes. Also, serial methods using X-ray FELs have the ability to study irreversible transformations. Serial methods of LCLS-II-HE will provide a unique capability to study irreversible reactions over a wider range of time scales.

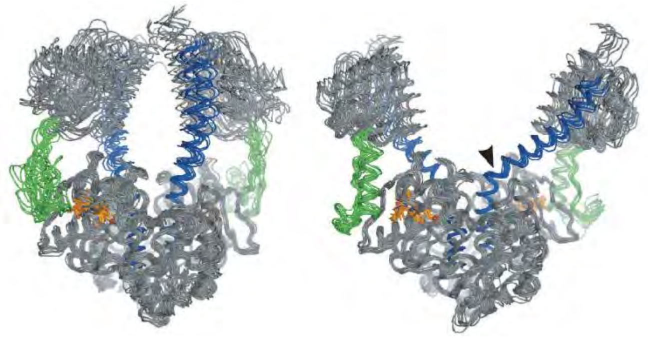

Figure 4.3.4. Proposed solution structures of bacterial phytochrome for the P_r (left) and P_{fr} (right) states of the photosensory core. The long scaffolding helix is highlighted in blue, the PHY tongue in green, and the biliverdin chromophore in orange. The PHY domain separation differs by about 3 nm between the P_r and P_{fr} structures. The hinge region at the scaffolding helix in P_{fr} is indicated with a black arrowhead [46].

Larger scale conformational dynamics in phytochromes (and related complexes) must be studied in more physiologically relevant conditions and linked to crystallography studies at higher resolution. LCLS-II-HE will be indispensable for time-resolved solution SAXS/WAXS which can provide low resolution but much faster than crystallography. Recent synchrotron studies of phytochrome photosensors [46] highlight the potential of this approach. Time-resolved SAXS on µs to ms timescales suggests an unusual mechanism by which atomic-scale conformational changes near the chromophore lead to angstrom-scale changes in the fold of the PHY tongue, and further lead to a nm-scale conformational signal (Figure 4.3.4). However, X-ray source capabilities limit these studies to the isolated photosensor unit, and to relatively slow timescales. LCLS-II-HE will map the dynamics of the full-length phytochrome on femtoseconds timescales and longer, to address key questions such as whether the opening of the dimer shown in Figure 4.3.4 is modified in the full structure or if different conformational changes may lead to exposure of previously hidden regions of the protein (*e.g.* to substrates). The high repetition rate of LCLS-II-HE combined with high resolution will be critical in enabling these types of studies.

Structural dynamics and rare events of functioning enzymes

In biological complexes, structural dynamics are particularly important in cases where high-resolution crystal structures at cryogenic temperature are unable to explain the fast enzyme kinetics observed in physiological conditions [47]. For example, acetylcholine esterase is characteristic of systems in which the catalytically active site resides deep inside the protein, with apparently limited accessibility that is inconsistent with observed high reaction turnover rates (50,000 per second). Dynamic breathing motions must facilitate these reactions, but neither high-resolution crystal structures nor solution scattering experiments have been able to capture such motions or explain the dynamic enzyme function. LCLS-II-HE will enable new structural dynamics methods to follow such processes in native environments.

The value of room-temperature experiments on small crystals has been demonstrated during LCLS structural studies of GPCR membrane proteins that mediate cellular communication and respond to a variety of extra-cellular signaling molecules [10]. Compared with structures from large cryo-cooled crystals, the room-temperature GPCR structures resolved at LCLS display a distinct distribution of thermal motions and conformations of residues that likely more accurately represent the receptor structure and dynamics in a cellular environment. This provides new insight into biological function. The high repetition rate of LCLS-II-HE, and the ability to collect 10^8-10^{10} scattering snapshots per day (combined with revolutionary advances in detectors and data science), will be indispensable for mapping the full range of spontaneous motions and conformations over a heterogeneous sample ensemble. Advanced analysis methods that exploit diffuse scattering [48] and more modeling of conformations [49]will be able to reveal currently inaccessible room temperature conformations due to the high repetition rate of LCLS-II-HE allowing greater sampling of rare states and improved data quality from higher redundancy.

The dynamic fluctuations and conformational response of enzymes to active substrates or small molecules in native environments is central to their biological function, and current structural biology methods provide only limited insight. The repetition rate of LCLS-II-HE combined with advanced microfluidic mixing liquid jets [50] will open entirely new opportunities for investigating enzyme dynamics and their response to rapidly introduced substrates. For SFX with 0.5 μm nanocrystals, diffusion times at room temperature are estimated to be ~10 μs [51]. For solution scattering approaches, comparable timescales may be accessible with micron-size mixing jets [50, 52, 53]. Both approaches require the small focus and high flux/pulse provided by X-ray FELs. While rapid mixing enhances the population of transient intermediate states, they nevertheless constitute "rare events," with their observation probability (and distinguishability from other states) determined by the reaction kinetics. The high repetition rate of LCLS-II-HE is essential in order to capture such rare events and characterize a distribution of transient intermediate structures.

In the frequent cases where metals are involved in the catalytic site, studies of enzymatic kinetics will benefit from the combination of diffraction techniques and element-specific X-ray spectroscopic techniques. Probing the subtle changes at the active site in multiple ways at high resolution will provide a very detailed picture of the evolution of the geometric and electronic structure of the active site over the reaction cycle of an enzyme.

To access the fastest enzyme dynamics, photo-activated caged substrates [54] may be employed to trigger enzymatic activity. More generally, the use of light to manipulate biological systems and trigger selected residues in time or space is a rapidly growing area of biological research that will be increasingly relevant for dynamic studies at LCLS-II-HE.

The study and rational design of light-consuming enzymes

Enzymes out-perform man-made catalysts on a routine basis, often working many orders of magnitude more quickly, conducting chemistry with fewer side products, and operating in aqueous solution near room temperature. Since enzymes are proteins, they can be easily introduced into biological systems through genetic engineering; enabling researchers to reprogram organisms to produce useful chemical matter (see *e.g.* recent work on opioid synthesis in yeast [55]).

The origins of the remarkable catalytic performance of enzymes remain one of the great mysteries of biochemistry [56]. Specifically, the details of how protein structure and dynamics combine to generate rapid and specific chemistry are unknown. The ability to image biochemical catalysis at atomic and femtosecond resolution, opens the possibility to both understand the fundamental physical foundation of biocatalysis and also advance rational design of new enzyme systems. Photoenzymes are ideally suited for this purpose, as their light-activated nature enables fine control of chemistry in both space and time. Time-resolved serial femtosecond crystallography (TR-SFX) of photoenzymes, therefore, is uniquely suited to address the longstanding scientific challenge of the origins of enzyme catalysis.

A main source of difficulty in identifying the source of enzyme's catalytic power is the range of timescales implicated. It has been suggested that timescales of protein motions ranging from femtoseconds (for hydrogen vibrations) to milliseconds (for domain-scale collective motions) influence catalysis [57, 58]. This span makes acquiring a fine series of time points over many decades highly desirable to definitively address the question of what role, if any, dynamics plays in enzyme-induced rate enhancement.

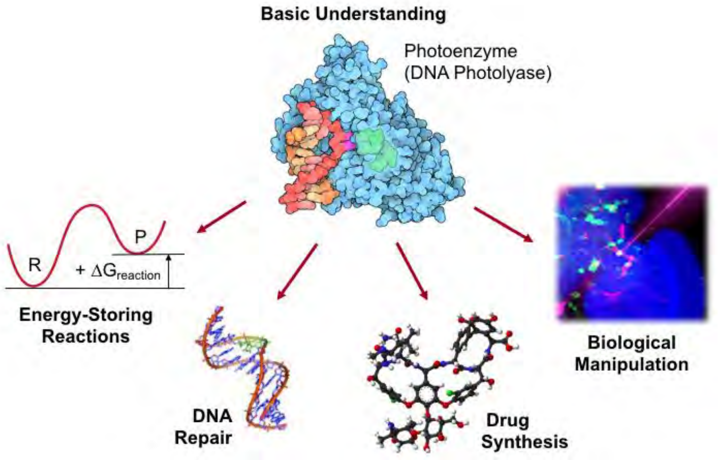

Figure 4.3.5. Example of applications of photoenzyme engineering based on a prototypical wild-type photoenzyme, DNA photolyase. Photolyase repairs UV-induced DNA lesions, using light to fix damage caused by light. Engineering of photolyase could result in new energy storing reactions, novel methods for DNA repair, new ways to synthesize complex molecules such as drugs, and finally spatiotemporal control of chemistry in biological systems using light.

The high repetition rate afforded by the LCLS-II-HE upgrade would make these studies possible. Currently, a single week-long TR-SFX experiment might hope to obtain two or three time points at best – invaluable information, but insufficient to cover many decades in time. Increasing the rate of data collection by orders of magnitude would enable movies at high resolution in both time and space, capable of putting to rest questions over the origins of enzyme catalysis. LCLS-I-HE offers the desired high repetition rate but for these studies, it lacks the high resolution capabilities that are absolutely necessary and will be providing by the high energy upgrade of LCLS-II-HE.

Such movies would also provide a firm foundation for engineering novel photoenzymes for applications in organic synthesis, biological manipulation, and medicine. The use of enzymes to conduct organic synthesis has long held appeal, due to enzyme's rapid turnover, chemical specificity, environmental friendliness, and biological origin. At the same time, the ability to perform photochemistry is highly desirable. Reactions involving the absorption of a photon are unique in that the chemical products can be higher in free energy than the reactants, enabling fuel production, for example. Photochemical reactions often exhibit different stereo- or regio-selectivity than the corresponding reaction performed on the ground state, providing synthetic access to specific enantiomers that might be desired in *e.g.* pharmaceutical applications. Finally, light provides a facile mechanism for manipulation of biological systems, a fact leveraged by optogenetics and biological photoactuators[59]. For all these reasons, the unique combination of proteins that conduct photochemistry – photoenzymes – provide an appealing engineering target. Development of new photoenzymes would be greatly facilitated by atomic-resolution time resolved imaging covering many decades in time, experiments possible with the LCLS-II-HE source.

References

1. C. Bostedt, *et al.*, "Linac Coherent Light Source: The first five years", *Reviews of Modern Physics,* **88**, 015007 (2016).
2. S. Boutet, *et al.*, "High-Resolution Protein Structure Determination by Serial Femtosecond Crystallography", *Science,* **337**, 362 (2012).
3. H. N. Chapman, *et al.*, "Femtosecond X-ray protein nanocrystallography", *Nature,* **470**, 73 (2011).
4. A. E. Cohen, *et al.*, "Goniometer-based femtosecond crystallography with X-ray free electron lasers", *Proceedings of the National Academy of Sciences of the United States of America,* **111**, 17122 (2014).
5. P. Fromme, "XFELs open a new era in structural chemical biology", *Nat. Chem. Biol.,* **11**, 895 (2015).

6. M. Uervirojnangkoorn, *et al.*, "Enabling X-ray Free Electron Laser Crystallography for Challenging Biological Systems from a Limited Number of Crystals", *Elife,* **4** (2015).
7. U. Weierstall, *et al.*, "Lipidic cubic phase injector facilitates membrane protein serial femtosecond crystallography", *Nature Communications,* **5**, 3309 (2014).
8. Q. J. Zhou, *et al.*, "Architecture of the synaptotagmin-SNARE machinery for neuronal exocytosis", *Nature,* **525**, 62 (2015).
9. R. Neutze, *et al.*, "Potential for biomolecular imaging with femtosecond X-ray pulses", *Nature,* **406**, 752 (2000).
10. Y. Y. Kang, *et al.*, "Crystal structure of rhodopsin bound to arrestin by femtosecond X-ray laser", *Nature,* **523**, 561 (2015).
11. M. Suga, *et al.*, "Native structure of photosystem II at 1.95 Å resolution viewed by femtosecond X-ray pulses", *Nature,* **517**, 99 (2015).
12. T. Gonen, "Microed: Three Dimensional Electron Diffraction of Microscopic Crystals", *BpJ,* **110**, 9a (2016).
13. T. Spatzal, *et al.*, "Ligand binding to the FeMo-cofactor: Structures of CO-bound and reactivated nitrogenase", *Science,* **345**, 1620 (2014).
14. J. L. Smith, and A. Thompson, "Reactivity of selenomethionine - dents in the magic bullet?", *Structure with Folding & Design,* **6**, 815 (1998).
15. T. R. M. Barends, *et al.*, "De novo protein crystal structure determination from X-ray free-electron laser data", *Nature,* **505**, 244 (2014).
16. T. Nakane, *et al.*, "Native sulfur/chlorine SAD phasing for serial femtosecond crystallography", *Acta Crystallographica Section D-Biological Crystallography,* **71**, 2519 (2015).
17. K. Yamashita, *et al.*, "An isomorphous replacement method for efficient de novo phasing for serial femtosecond crystallography", *Scientific Reports,* **5** (2015).
18. K. Ayyer, *et al.*, "Macromolecular diffractive imaging using imperfect crystals", *Nature,* **530**, 202 (2016).
19. R. A. Kirian, *et al.*, "Direct Phasing of Finite Crystals Illuminated with a Free-Electron Laser", *Physical Review X,* **5**, 011015 (2015).
20. M. Bergh, *et al.*, "Feasibility of imaging living cells at subnanometer resolutions by ultrafast X-ray diffraction", *QRBio,* **41**, 181 (2008).
21. G. Huldt, A. Szőke, and J. Hajdu, "Diffraction imaging of single particles and biomolecules", *Journal of Structural Biology,* **144**, 219 (2003).
22. A. Aquila, *et al.*, "The linac coherent light source single particle imaging road map", *Struct. Dyn.,* **2**, 041701 (2015).
23. Z. Kam, "Determination of Macromolecular Structure in Solution by Spatial Correlation of Scattering Fluctuations", *Macromolecules,* **10**, 927 (1977).
24. Z. Kam, M. H. Koch, and J. Bordas, "Fluctuation x-ray scattering from biological particles in frozen solution by using synchrotron radiation", *Proc. Natl. Acad, Sci. USA,* **78**, 3559 (1981).
25. D. K. Saldin, *et al.*, "Structure of a single particle from scattering by many particles randomly oriented about an axis: toward structure solution without crystallization", *NJPh,* **12**, 14 (2010).
26. E. Malmerberg, C. A. Kerfeld, and P. H. Zwart, "Operational properties of fluctuation X-ray scattering data", *IUCrJ,* **2**, 309 (2015).
27. P. B. Moore, "How should we think about the ribosome?", *Annu Rev Biophys,* **41**, 1 (2012).
28. A. Dashti, *et al.*, "Trajectories of the ribosome as a Brownian nanomachine", *Proceedings of the National Academy of Sciences of the United States of America,* **111**, 17492 (2014).
29. J. Frank, *Three-Dimensional Electron Microscopy of Macromolecular Assemblies* (Oxford University Press, New York, 2006).
30. P. Schwander, R. Fung, and A. Ourmazd, "Conformations of macromolecules and their complexes from heterogeneous datasets", *Philosophical Transactions of the Royal Society B: Biological Sciences,* **369** (2014).
31. R. Fung, *et al.*, "Structure from fleeting illumination of faint spinning objects in flight", *NatPh,* **5**, 64 (2009).
32. P. Schwander, *et al.*, "Mapping the conformations of biological assemblies", *NJPh,* **12**, 035007 (2010).
33. N. T. Loh, and V. Elser, "Reconstruction algorithm for single-particle diffraction imaging experiments", *Phys Rev E. ,* **80**, 026705 (2009).
34. H. T. Philipp, *et al.*, "Solving structure with sparse, randomly-oriented x-ray data", *OExpr,* **20**, 13129 (2012).
35. M. F. Hantke, *et al.*, "High-throughput imaging of heterogeneous cell organelles with an X-ray laser", *Nature Photonics,* **8**, 943 (2014).

36. A. Hosseinizadeh, *et al.*, "Single-particle structure determination by X-ray free-electron lasers: Possibilities and challenges", *Structural Dynamics,* **2**, 041601 (2015).
37. T. R. M. Barends, *et al.*, "Direct observation of ultrafast collective motions in CO myoglobin upon ligand dissociation", *Science,* **350**, 445 (2015).
38. K. Pande, *et al.*, "Femtosecond structural dynamics drives the trans/cis isomerization in photoactive yellow protein", *Science,* **352**, 725 (2016).
39. R. W. Schoenlein, *et al.*, "The first step in vision: Femtosecond isomerization of rhodopsin", *Science,* **254**, 412 (1991).
40. L. A. Peteanu, *et al.*, "The first step in vision occurs in femtosecond: Complete blue and red spectral shifts", *PNAS,* **90**, 11762 (1993).
41. Q. Wang, *et al.*, "Vibrationally coherent photochemistry in the femtosecond primary event of vision", *Science,* **266**, 422 (1994).
42. P. H. Quail, "Phytochrome photosensory signalling networks", *Nat. Rev. Mol. Cell Biol.,* **3**, 85 (2002).
43. J. Dasgupta, *et al.*, "Ultrafast excited-state isomerization in phytochrome revealed by femtosecond stimulated Raman spectroscopy", *PNAS,* **106**, 1784 (2009).
44. D. Arnlund, *et al.*, "Visualizing a protein quake with time-resolved X-ray scattering at a free-electron laser", *Nat Meth,* **11**, 923 (2014).
45. M. Levantino, *et al.*, "Ultrafast myoglobin structural dynamics observed with an X-ray free-electron laser", *Nat Commun,* **6**, 6772 (2015).
46. H. Takala, *et al.*, "Signal amplification and transduction in phytochrome photosensors", *Nature,* **509**, 245 (2014).
47. D. A. Keedy, *et al.*, "Crystal Cryocooling Distorts Conformational Heterogeneity in a Model Michaelis Complex of DHFR", *Structure,* **22**, 899 (2014).
48. A. H. Van Benschoten, *et al.*, "Measuring and modeling diffuse scattering in protein X-ray crystallography", *PNAS,* **113**, 4069 (2016).
49. D. A. Keedy, *et al.*, "Mapping the conformational landscape of a dynamic enzyme by multitemperature and XFEL crystallography", *Elife,* **4** (2015).
50. M. Trebbin, *et al.*, "Microfluidic liquid jet system with compatibility for atmospheric and high-vacuum conditions", *LChip,* **14**, 1733 (2014).
51. M. Schmidt, "Mix and Inject: Reaction Initiation by Diffusion for Time-Resolved Macromolecular Crystallography", *Advances in Condensed Matter Physics,* **2013**, 10 (2013).
52. D. J. Wang, *et al.*, "Double-focusing mixing jet for XFEL study of chemical kinetics", *Journal of Synchrotron Radiation,* **21**, 1364 (2014).
53. D. E. Hertzog, *et al.*, "Optimization of a Microfluidic Mixer for Studying Protein Folding Kinetics", *AnaCh,* **78**, 4299 (2006).
54. G. C. R. Ellis-Davies, "Caged compounds: photorelease technology for control of cellular chemistry and physiology", *Nat Meth,* **4**, 619 (2007).
55. S. Galanie, *et al.*, "SYNTHETIC BIOLOGY Complete biosynthesis of opioids in yeast", *Science,* **349**, 1095 (2015).
56. R. Wolfenden, and M. J. Snider, "The depth of chemical time and the power of enzymes as catalysts", *Acc. Chem. Res.,* **34**, 938 (2001).
57. S. J. Benkovic, and S. Hammes-Schiffer, "A perspective on enzyme catalysis", *Science,* **301**, 1196 (2003).
58. K. A. Henzler-Wildman, *et al.*, "A hierarchy of timescales in protein dynamics is linked to enzyme catalysis", *Nature,* **450**, 913 (2007).
59. A. Gautier, *et al.*, "How to control proteins with light in living systems", *Nat. Chem. Biol.,* **10**, 533 (2014).

4.4 Materials Heterogeneity, Fluctuations and Dynamics

Ultrafast, atomic-scale, dynamical motions underlie the energy efficiency and performance of functional materials and devices. There exists untapped potential to enhance materials performance and create new functionality through a much deeper insight into the atomic-scale dynamics of materials. To date, ultrafast X-ray studies of materials have focused largely on discovery-oriented science, employing time-resolution to disentangle the coupled degrees of freedom in strongly correlated materials or to capture snapshots of material transformations. LCLS-II-HE will enable sensitive real-time *in situ* probes of atomic-scale structure that will advance this field from demonstration experiments in model systems, to measurements that address applications-oriented materials challenges. This novel class of measurements will lead to new understanding of materials, and ultimately device performance, and will couple directly to both theory efforts and next generation materials design initiatives.

4.4.1 Charge migration at the atomic scale in complex materials for energy storage and conversion

Detailed knowledge of atomic and ionic diffusion is fundamental for the functionality, synthesis, and stability of a wide range of materials. In particular, diffusion of electroactive ions in complex electrode materials is central to the function of many technological devices for energy transformation and storage including fuel cells, batteries, and membranes used for desalination and separations. The diffusion dynamics of the ions through the crystal lattice of an electrode material (*e.g.* Li^+, Na^+, or multivalent ions in a battery) have a tremendous impact on the energy storage capacity, rate capability, and material lifetime. Slow diffusion is believed to be a factor limiting charge and discharge rates in many electrode materials, and can, for example, limit fast charging in electric vehicles.

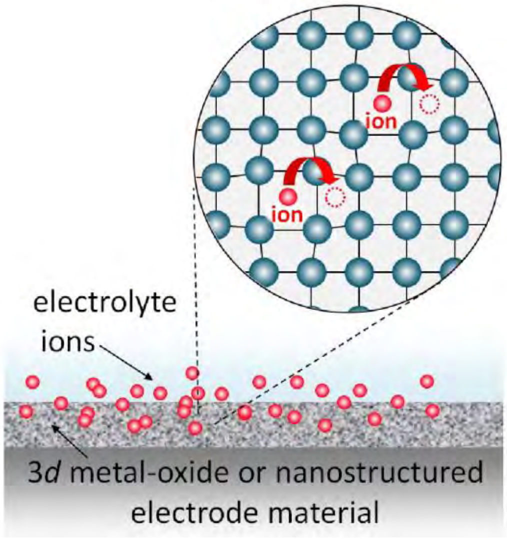

Figure 4.4.1. Illustration of ion diffusion dynamics and local strain in crystalline electrode material.

While much is known from first-principles modeling and simulation about how ions diffuse through a lattice [1, 2], little is known experimentally about the atomic-scale processes involved in ion diffusion. On fundamental length and time scales, individual ion-hopping events between adjacent interstitial sites may approach ~100 fs timescales. These events or hops are associated with significant transient changes in the crystal strain field [3], which in turn can influence the dynamics of neighboring ions at high concentrations (see Figure 4.4.1). Such statistical ultrafast local events ultimately link to longer-range dynamics spanning many decades, since the slower coupled diffusional motions occur as a result of many local hops. Our ability to characterize such phenomena over the length and time scales required for comparison with theory is substantially limited by available experimental tools. This has restricted our ability to develop validated design guidelines to improve ion diffusion in functional materials.

The capabilities of LCLS-II-HE will enable much more detailed insight into ion and atom migration in complex materials under operating conditions. Dynamic scattering with coherent X-rays (XPCS) has already been shown to be a powerful probe of atomic diffusion [4], but it is limited to relatively slow timescales (typically ms and longer) by present X-ray sources. Advanced XPCS techniques with a high-repetition-rate hard X-ray laser (as outlined in Section 3.3) will enable *operando* studies of the local aspects of ion diffusion at a high spatial resolution due to the higher photon energy of LCLS-II-HE. Systematic studies will reveal how these processes depend on electrode nanostructure, material crystal structure, diffusion direction, and ion concentration (state of charge).

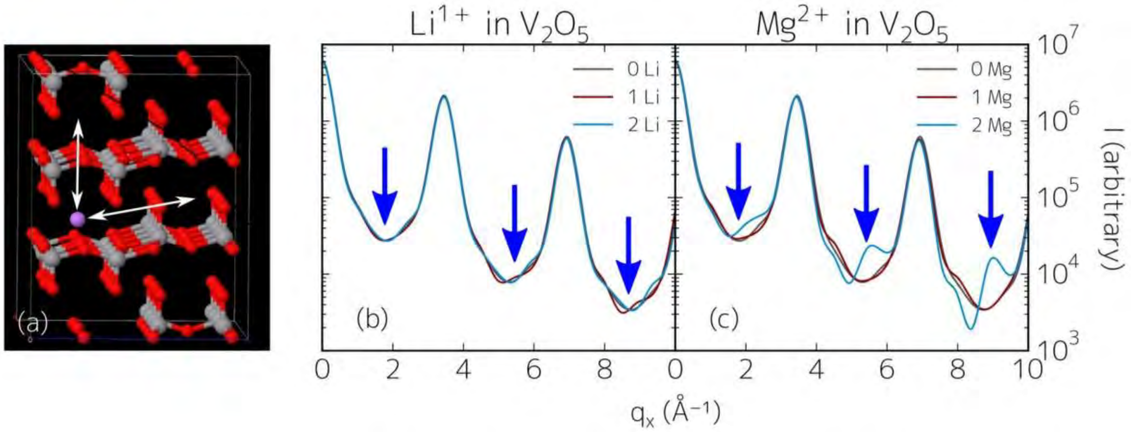

Figure 4.4.2. (a) *Ab-initio* simulated structure of Li^{1+} intercalated into V_2O_5, and possible jump vectors along the crystallographic a- and c-directions. Note that these likely have a vastly different jump probability. (b) and (c) Calculated diffuse scattering from the obtained structures for 0, 1 and 2 Li^{1+} (Mg^{2+}) ions intercalated into V_2O_5 along the $\boldsymbol{q}_x$ direction, showing diffuse scattering due to occupational disorder. The blue arrows indicate the half-order peaks originating in partial ion occupancy. Notice the increased intensity in the case of Mg^{2+} due to the larger scattering cross-section. Similar changes appear for Li^+ but are difficult to distinguish on the logarithmic scale.

Coherent X-ray scattering from the electrode material will directly probe transient distortions of the lattice and longer-range strain fields that arise from stochastic ion-hopping events (as illustrated in Figure 4.4.1) on relevant timescales, from <1 ps to ms, that are presently inaccessible. With LCLS-II-HE, an initial speckle pattern can be obtained from the electrode at t=0. This is followed by speckle patterns at time-delays from <100 fs up to milliseconds using the two-pulse, programmable XPCS mode on LCLS-II-HE. The ion dynamics are encoded in the time-dependent auto-correlation function of the scattering intensity, $g_2(\boldsymbol{q}, t)$, which is directly related to the dynamic structure factor, $S(\boldsymbol{q},t)$. The auto-correlation function and dynamic structure factor can be analyzed by Fourier transformation or referenced to theory and modeling.

For time scales of the hops (<1 ps), this approach can determine the local distortion *during* the hop, which can be compared with the hop trajectory expected from theory. As an illustration, Figure 4.4.2 shows *ab initio* model calculations of the diffuse scattering from Li^{1+} and Mg^{2+} intercalated into V_2O_5 [5]. Note that even on a log scale, there are large changes in scattering near the half-order partial occupancy "peak" (indicated by the blue arrows), resulting from partial Mg^{2+} occupancy. Changes are smaller, but still measurable for the Li^{1+}. Thus, we expect measurable changes even for single to few ion hops.

The LCLS-II-HE brings two advantages. Most significant is that the higher X-ray energy provides accesses to speckle data at much higher scattering momenta $\boldsymbol{q}$, with consequence that the atomic motions during hops can be obtained with finer spatial resolution. The practical highest $\boldsymbol{q}$ for soft X-rays from LCLS-II is small, and this dramatically limits the measurable spatial resolution. Second, higher photon energies are more able to penetrate the environments relevant to energy storage applications.

This example of ion diffusion in V_2O_5 electrodes is archetypal, and the approach can be applied to diffusion dynamics of many other types of ions or atoms in condensed matter. For example, similar studies will be relevant to diffusion of oxygen anions in solid-oxide fuel cells, membranes for chemical separations (*e.g.* desalination, CO_2 sequestration), and environmental chemistry. In addition, related XPCS studies could be used to probe the dynamics of small polarons, as shown in Figure 4.4.3. These charge localizations are associated with subtle lattice distortions, and inhibit the flow of charge in complex oxides cathode materials [6].

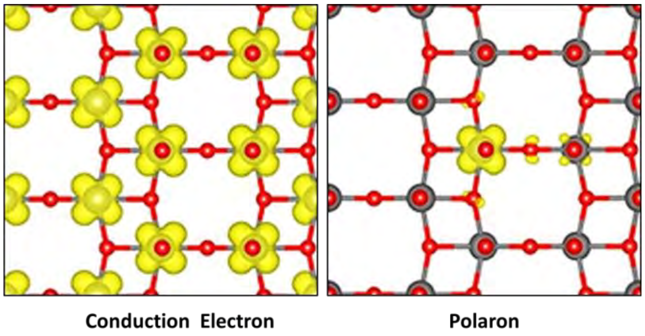

Figure 4.4.3. Crystal structure of V_2O_5 with typical conduction electron distribution (left), and localized electron density (polaron) associated with a subtle local distortion in the crystal structure (right) [6].
(credit Yufeng Liang, LBNL)

4.4.2 Nanoscale non-equilibrium phonon dynamics & thermal transport

Understanding heat flow at nanoscale dimensions, in heterogeneous systems, and across interfaces is a fundamental problem that has the potential to provide technological solutions to our energy needs by enabling new technologies to manipulate the flow of energy. There are two well-understood limits of this problem: a macroscopic, continuum description governed by the diffusion equation, and an atomic-level description based on classical physics or quantum mechanics (*e.g.* classical or *ab-initio* molecular dynamics). However, the intermediate regime between diffusive and ballistic transport is almost completely unexplored. This intermediate regime is particularly relevant in nanostructures and heterogeneous systems, where the characteristic dimensions are comparable to the phonon mean free paths, thereby opening new approaches to nanoscale control of thermal transport.

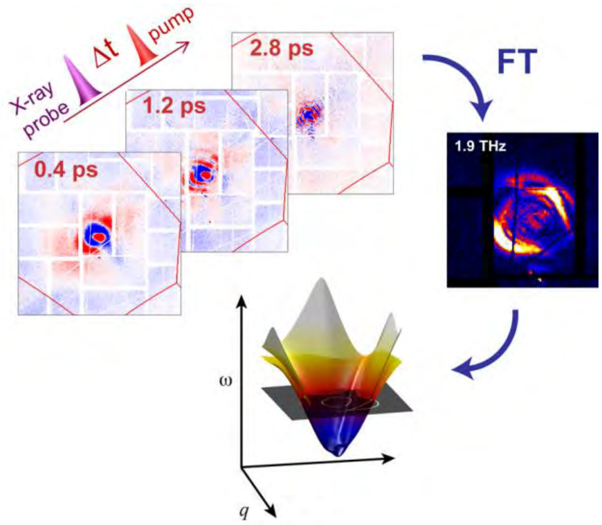

Figure 4.4.4. Fourier transform (FT) inelastic X-ray scattering (FT-IXS). Left: differential X-ray scattering intensities from Ge at various time delays. Right: magnitude of FT at 1.9 THz showing momentum distribution of phonons in particular region of ***q***-space. Bottom: schematic of the Ge acoustic phonon dispersion from data [7].

A similar scientific challenge arises in understanding energy transport in 2D materials in the monolayer and multilayer limit, where the out-of-plane dimension is comparable to phonon wavelengths and mean free paths. An understanding of the interfacial thermal conductivity associated with a monolayer on substrate, or the ability to measure directly the cross-plane thermal conductivity in a multilayer is a requirement, for example, for the implementation of quasi-2D materials as phase-change materials within a working device. Clearly, a fundamental description of phonon transport in this crossover regime is needed for the targeted design of nanostructured materials, functional hierarchical structures, and two-dimensional heterostructures. However, this requires transformative new methods for imaging phonon propagation with microscopic (wavevector) resolution and femtosecond to nanosecond timescales. Novel XFEL sources and experiments will play a central role in the development of these technologies.

X-ray diffraction techniques at high-repetition rate open up a new window into these processes at buried interfaces by directly resolving in real time the transfer of energy within a complex heterostructure [8]. Furthermore, new XFEL-based techniques such as Fourier-Transform Inelastic X-ray Scattering (FT-IXS) [7, 9, 10] have sensitivity to the phonon wavevector across the Brillouin zone, and thus give access to the dynamics of the heat-carrying, short-wavelength phonons that have THz frequencies on ultrafast timescales. This approach is illustrated in Figure 4.4.4, which presents LCLS measurements of nonequilibrium phonon dispersion in bulk Ge.

Since the structural changes associated with phonon transport across buried interfaces are subtle [8], FT-IXS measurements of interface conductance are extremely challenging with existing XFEL sources. Similarly, differential X-ray scattering signals from nanostructured materials – such as those designed for manipulating thermal transport, as illustrated in Figure 4.4.5 – are extremely weak. While LCLS provides the necessary hard-X-ray photons for FT-IXS methods, these methods are limited primarily by average brightness which determines the achievable signal-to-noise ratio. Thus, the low repetition-rate and large intensity-fluctuations of LCLS restrict experiments to bulk samples and ideal model systems. Although LCLS-II will provide more stable pulses at high repetition-rate, the low photon energy (< 5 keV) limits the accessible regions of reciprocal space and prevents the study of buried structures.

The high repetition rate of the LCLS-II-HE will not only increase the data quality by orders of magnitude compared with that of LCLS but will allow *in situ* studies of functional materials under technologically relevant device conditions. Weakly scattering nanostructures and subtle effects from interfaces that are beyond the current capabilities will be open to study with LCLS-II-HE. For example, the time-domain application of techniques like coherent Bragg rod analysis (COBRA) [11] can directly measure and reconstruct the time-dependent electron density distribution within a monolayer or few-layer sample. Pair-distribution-function (PDF) approaches can extract time-dependent pair correlation functions [12]. The high-stability and extension of the fundamental energy of LCLS-II-HE to beyond 20 keV (in addition to the extremely high energy of the third harmonic) make these methods feasible for the first time. Furthermore, many technologically relevant materials are structurally heterogeneous at the nanoscale, requiring imaging techniques with nanoscale resolution, or complementary ***q***-space techniques such as XPCS or FT-IXS (see Section 3.3). These studies require hard X-ray pulses to access large momentum transfer, moderate peak power to avoid single-pulse damage, and high repetition rate to probe weakly scattering nanostructures and 2D layers.

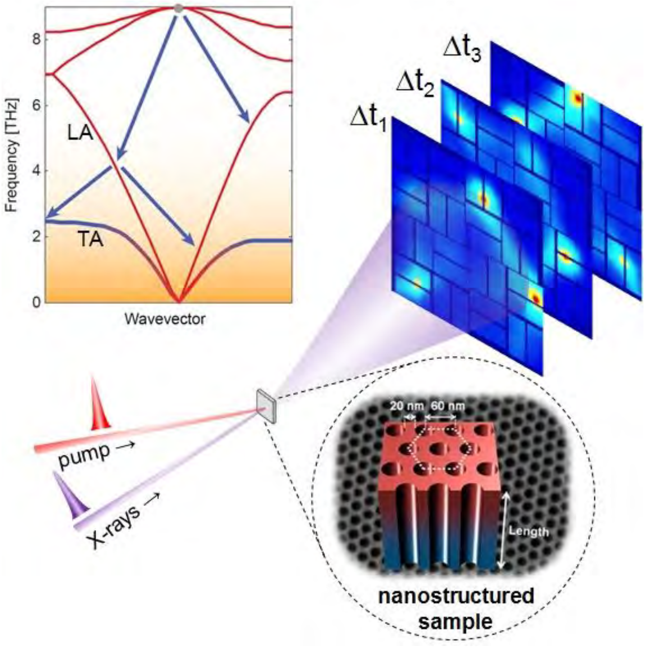

Figure 4.4.5. Illustration of X-ray scattering probe of energy transport dynamics in nanostructured Si material designed to exploit ballistic transport for anisotropic thermal conductivity [13]. Left inset: Equilibration scheme for nonequilibrium phonons indicating a bottleneck in coupling to TA modes.

4.4.3 Electron-lattice interaction and material functionality

In many technologically relevant materials, electron-lattice interactions determine material functionality and performance under operational conditions. For example, electron-lattice coupling in organic photovoltaics leads to polaronic distortions which fundamentally determine charge mobility; in other cases, the material operates near or across a phase boundary, as in phase-change materials. In thermoelectric applications, the desirable properties (*e.g.* low thermal conductivity) depend on the interactions between valence electrons and the lattice which give rise to highly anomalous phonon modes. Pump-probe experiments can be used to decouple the electron-lattice dynamics. Here we show two examples of currently challenging experiments that are enabled by LCLS-II-HE.

Electron-phonon coupling in 2D transition metal dichalcogenides

Two-dimensional (2D) transition metal dichalcogenides and related materials have attracted great interest in recent years because of their novel electronic, optical, and mechanical properties. These include the emergence of a direct band gap; strong light-matter, electron-electron and electron-phonon interactions; enhanced catalytic activity; unique semiconducting and metallic structural phases; and the ability to withstand extreme strains [14-17]. By stacking 2D layers as heterostructures, novel hybrid materials with unique functionalities can be synthesized, making use of the weak interlayer van der Waals bonding [18, 19]. This weak coupling in turn creates novel opportunities for manipulating their structural and optoelectronic properties with external fields or perturbations. Sensitive atomic-scale, time-resolved, *in situ* probes are required to resolve these changes.

For example, small temperature changes in these multilayer structures have been shown to drive a transition from an indirect to a direct band gap, and this is associated with changes in the interlayer coupling [20]. Under photoexcitation, ultrafast optical studies in layered *1T*-TaS_2 have revealed a hidden quantum phase [21]. Recent preliminary work at SSRL (using hard X-ray scattering at 100 ps resolution and MHz repetition rate) has shown that light can be used to modulate and control the interlayer bonding in the prototypical transition metal dichalcogenide MoS_2 (Figure 4.4.6), giving rise to a surprising *compressive* strain at the 10^{-6} level, which is measurable only as a result of the MHz X-ray repetition rate. This effect can be thought of as a modulation of the van der Waals / Casimir interaction between layers [22], driven by electronic excitation. It opens up novel possibilities for manipulation of the functional properties of 2D materials on ultrafast timescales at high bandwidths. These measurements require high-repetition-rate probes in order to resolve these near-equilibrium responses.

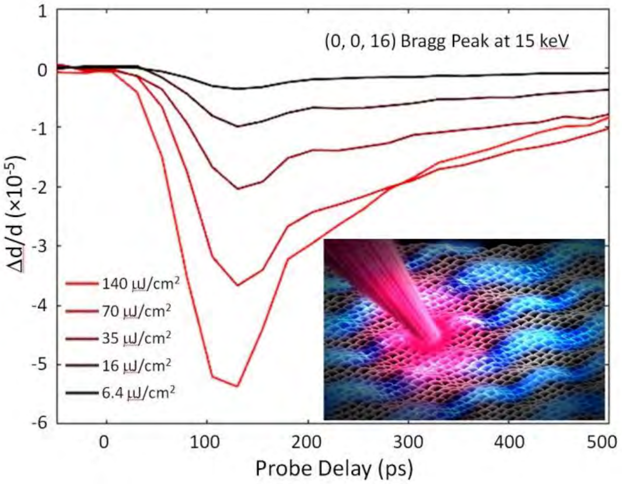

Figure 4.4.6. Interlayer light-driven dynamic compressive strain in few-layer MoS_2 from MHz X-ray diffraction of (0,0,16) reflection with 100 ps synchrotron pulses. Present time resolution is inadequate to resolve the underlying dynamics. Inset: Illustration of dynamical response of a monolayer transition metal dichalcogenide driven by optical excitation (A.M. Lindenberg – unpublished).

Similar opportunities exist for probing exciton-phonon interactions in the quasi-2D limit. Prior studies have indicated the important role of exciton-lattice interactions in the monolayer limit, but direct probes of the atomic-scale vibrational response following optical creation of an exciton are not possible using current XFEL sources. Direct measurements of the lattice response, in parallel with existing techniques for probing the electronic response, will open a new window into the coupled electronic-structural degrees of freedom in 2D materials, which determine their functional properties. This will provide a comprehensive understanding of the flow of electronic and vibrational excitation across an interface between two van-der-Waals layers as a function of the relative crystallographic orientation of the layers. In particular, for a homo-interface between two of the same materials, misorientation from crystallographic registry provides a new approach to modifying thermal and electrical interfacial transport and a potential route to improved performance of thermoelectric materials.

The above experiments require structural probes sensitive to both the in-plane and out-of-plane unit cell dynamics. Access to high momentum transfer (provided by hard X-rays) is required to reconstruct the unit cell dynamics and local strain fields. High repetition rates enable measurements of the small local lattice displacements associated with these materials under technologically relevant device conditions.

Electron-phonon coupling in hybrid perovskites

Lead-halide hybrid perovskites have emerged as disruptive materials for photovoltaics, with power conversion efficiencies now exceeding 20% – comparable to polycrystalline silicon [23]. In the prototypical methylammonium lead-halide ($CH_3NH_3PbX_3$, X=I, Br, Cl), charge carriers in polycrystalline films show remarkably long lifetimes (>1 μs) with correspondingly long diffusion lengths, which are essential for efficient extraction of charge in a photovoltaic device. The fundamental mechanisms for these remarkable properties are not understood.

Recent studies have suggested that ultrafast structural dynamics following absorption of a photon underlie these efficiencies. For example, experiments have pointed towards the importance of coupled electronic and structural polaronic distortions in protecting charges from seeing the intrinsic defects in these materials [9]. These effects are connected, in turn, to proposals that the hybrid organic-inorganic structure of these materials leads to greater structural deformability, giant photostriction responses, and strong light-matter coupling [24, 25].

Theoretical studies have pointed toward the role of dynamic structural fluctuations and coupling to electronic structure as a potential explanation for the long carrier lifetimes and slow recombination rates exhibited by these materials even in the presence of significant defects [26, 27]. Thus, there appears to exist an important connection between electronic and structural processes at early time-scales after photoexcitation – atomic-scale processes that determine the efficiency of a photovoltaic device.

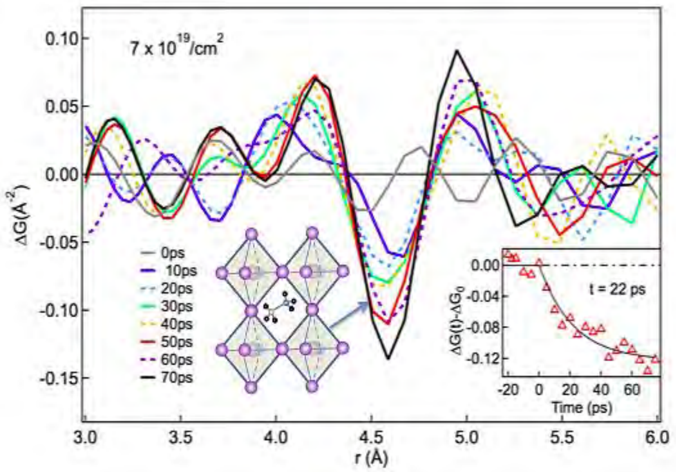

Figure 4.4.7. Time-dependent change in pair correlation function in $CH_3NH_3PbI_3$ as measured by femtosecond electron scattering techniques (X. Wu, A.M. Lindenberg – unpublished).

Direct experimental probes of the coupled optical and structural response that likely underlie these functional properties are not available from present sources, but will be possible with the capabilities of LCLS-II-HE. The organic groups within these hybrid materials lead to fragility, making pump-probe experiments at high excitation density (as typically required for measurements with LCLS at 120 Hz) difficult to perform without perturbing the material structure. Experiments therefore need to be carried out under weak excitation conditions, corresponding to small-amplitude lattice distortions. Under conditions where the peak power of LCLS leads to damage, the high repetition rate of LCLS-II-HE would enable measurements of small-amplitude, weakly perturbative, local strain fields. These measurements require access to high momentum transfer to enable PDF analysis and extraction of the dynamic atomic correlations that are potentially modulated through absorption of a photon.

In preliminary measurements, we have used femtosecond electron scattering to probe dynamics in methylammonium lead iodide at sufficiently high momentum transfer (***q***) to allow for extraction of a time-dependent pair correlation function, shown in Figure 4.4.7. This shows, surprisingly, that changes occur predominantly in the iodine-iodine correlation peak (whereas minimal changes occur in the lead-iodide correlation peak), corresponding to a light-induced sublattice disordering of the iodine octahedra. These measurements suggest that bonding between the organic group and the iodine octahedra play an important role in charge transport. Thus, the first steps following creation of an electron-hole pair may be influenced by both the intrinsic structural fluctuations and by light-induced enhancement of these fluctuations. These results illustrate the power of carrying out measurements at high enough momentum transfer to probe time-dependent pair correlation functions, as enabled by LCLS-II-HE (exploiting the projected fundamental energy range beyond 20 keV, or the third harmonic at higher energies). In contrast, the ***q***-resolution that is achievable via ultrafast electron scattering at high electron energies is inadequate to support a careful reconstruction of the pair distribution function.

We note that in addition to the prototypical 3D hybrid perovskites, there exists a class of 2D hybrid perovskites analogous to the transition metal dichalcogenide materials discussed above. These quantum-well-like structures exhibit a host of unique opto-electronic responses, including, for example, broadband photoluminescence spanning the entire visible spectral range [28]. It is thought that charge localization and the development of large structural distortions around a self-trapped exciton give rise to these properties, but the mechanisms are not well understood [28]. Here, in addition to X-ray scattering, X-ray spectroscopy methods with elemental specificity will provide complementary insight into the local polaronic distortions and charge localization that may underlie these properties.

Electron-phonon coupling and anharmonicity in thermoelectric materials

PbTe is an example of a broad class of thermoelectric materials where the low thermal conductivity results from a balanced interplay between electron-phonon coupling and anharmonicity. PbTe, in particular, exhibits incipient ferroelectric behavior (a tendency towards ferroelectric ordering but without macroscopic order) and it is believed that the associated mode softening of the transverse optical (TO) branch accounts for the low lattice conductivity in PbTe. Research to date has concentrated on the role of lattice anharmonicity and phonon-phonon interactions [29-34]. On the other hand, a few theoretical studies have focused on the importance of electron-phonon coupling as a link between the mixed ionic-covalent character of Pb–Te bonds and the soft mode behavior [33, 35].

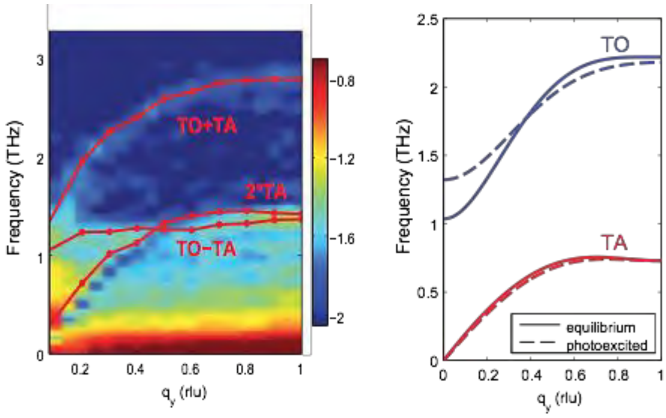

Figure 4.4.8. Left: FT-IXS spectrum of the phonon dispersion in photoexcited PbTe. Right: calculations showing that photo-excitation stiffens the TO branch at ***q***=0, and pushes the system away from ferroelectricity. The experimental observation of combination modes TO±TA (left) is a signature of this effect and can be used to identify how photo-excitation changes the interatomic forces.

A recent LCLS experiment [36] showed that electron-phonon coupling rather than phonon-phonon interactions (anharmonicity) leads to ferroelectric tendencies in PbTe. Furthermore, with the help of first principles simulations, the relevant electronic states that couple to the ferroelectric soft mode were identified. This experiment used FT-IXS [7] to probe the non-equilibrium phonon dispersion upon photoexcitation. The observed spectrum of phonons (obtained from a Fourier transform of the oscillatory components) contained combinations of TO±TA frequencies, and these are signatures of how the bonding forces in the photoexcited state differ from the bonding forces of the ground state (see Figure 4.4.8), resulting in eigenmodes that are linear combinations of the ground states TO and TA [36].

Since the experiment directly measures the mixing of the eigenvectors, ideally one could extract from these data how and which of the elements of the dynamical matrix change upon photoexcitation. Unfortunately, this is out of reach for current XFEL sources; the LCLS data [36] were limited to high signal-to-noise regions of reciprocal space, and samples were limited by the absorbed pulse energy rather than the average power. The high repetition rate and high stability of LCLS-II-HE will provide a transformative opportunity to reveal the fine details of how the valence electrons affect the interatomic forces by probing the phonon spectrum out of equilibrium.

References

1. G. S. Gautam*, et al.*, "The Intercalation Phase Diagram of Mg in V_2O_5 from First-Principles", *Chem. Mater.,* **27**, 3733 (2015).
2. G. S. Gautam*, et al.*, "First-principles evaluation of multi-valent cation insertion into orthorhombic V_2O_5", *ChCom,* **51**, 13619 (2015).
3. A. Van der Ven, J. Bhattacharya, and A. A. Belak, "Understanding Li Diffusion in Li-Intercalation Compounds", *Acc. Chem. Res.,* **46**, 1216 (2013).
4. M. Leitner*, et al.*, "Atomic diffusion studied with coherent X-rays", *Nat Mater,* **8**, 717 (2009).
5. G. Ceder, and G. S. Gautam, *personal communication,* (2016).
6. L. R. De Jesus*, et al.*, "Mapping polaronic states and lithiation gradients in individual V_2O_5 nanowires", *Nat Commun,* **7** (2016).
7. M. Trigo*, et al.*, "Fourier-transform inelastic X-ray scattering from time- and momentum-dependent phonon-phonon correlations", *Nat Phys,* **9**, 790 (2013).
8. M. Kozina*, et al.*, "Measurement of transient atomic displacements in thin films with picosecond and femtometer resolution", *Structural Dynamics,* **1**, 034301 (2014).
9. X. Y. Zhu, and V. Podzorov, "Charge Carriers in Hybrid Organic–Inorganic Lead Halide Perovskites Might Be Protected as Large Polarons", *The Journal of Physical Chemistry Letters,* **6**, 4758 (2015).
10. M. P. Jiang*, et al.*, "The origin of incipient ferroelectricity in lead telluride", *Nat Commun,* **7** (2016).
11. Y. Yacoby*, et al.*, "Direct determination of epitaxial interface structure in Gd_2O_3 passivation of GaAs", *Nat Mater,* **1**, 99 (2002).
12. E. S. Božin*, et al.*, "Entropically Stabilized Local Dipole Formation in Lead Chalcogenides", *Science,* **330**, 1660 (2010).
13. J. Lee, J. Lim, and P. Yang, "Ballistic Phonon Transport in Holey Silicon", *Nano Lett.,* **15**, 3273 (2015).
14. K.-A. N. Duerloo, Y. Li, and E. J. Reed, "Structural phase transitions in two-dimensional Mo- and W-dichalcogenide monolayers", *Nat Commun,* **5** (2014).
15. J. Feng*, et al.*, "Strain-engineered artificial atom as a broad-spectrum solar energy funnel", *Nat Photon,* **6**, 866 (2012).
16. K. F. Mak*, et al.*, "Atomically Thin MoS_2: A New Direct-Gap Semiconductor", *Phys. Rev. Lett.,* **105**, 136805 (2010).
17. E. M. Mannebach*, et al.*, "Dynamic Structural Response and Deformations of Monolayer MoS_2 Visualized by Femtosecond Electron Diffraction", *Nano Lett.,* **15**, 6889 (2015).
18. L. Britnell*, et al.*, "Strong Light-Matter Interactions in Heterostructures of Atomically Thin Films", *Science,* **340**, 1311 (2013).
19. F. Withers*, et al.*, "Light-emitting diodes by band-structure engineering in van der Waals heterostructures", *Nat Mater,* **14**, 301 (2015).

20. S. Tongay, *et al.*, "Thermally Driven Crossover from Indirect toward Direct Bandgap in 2D Semiconductors: $MoSe_2$ versus MoS_2", *Nano Lett.,* **12**, 5576 (2012).
21. L. Stojchevska, *et al.*, "Ultrafast Switching to a Stable Hidden Quantum State in an Electronic Crystal", *Science,* **344**, 177 (2014).
22. E. G. Galkina, *et al.*, "Drastic change of the Casimir force at the metal-insulator transition", *Phys. Rev. B,* **80**, 125119 (2009).
23. X. Li, *et al.*, "A vacuum flash–assisted solution process for high-efficiency large-area perovskite solar cells", *Science,* **353**, 58 (2016).
24. D. A. Egger, A. M. Rappe, and L. Kronik, "Hybrid Organic–Inorganic Perovskites on the Move", *Acc. Chem. Res.,* **49**, 573 (2016).
25. Y. Zhou, *et al.*, "Giant photostriction in organic-inorganic lead halide perovskites", *Nat Commun,* **7** (2016).
26. C. Motta, *et al.*, "Revealing the role of organic cations in hybrid halide perovskite CH3NH3PbI3", *Nat Commun,* **6** (2015).
27. F. Zheng, *et al.*, "Rashba Spin–Orbit Coupling Enhanced Carrier Lifetime in $CH_3NH_3PbI_3$", *Nano Lett.,* **15**, 7794 (2015).
28. T. Hu, *et al.*, "Mechanism for Broadband White-Light Emission from Two-Dimensional (110) Hybrid Perovskites", *The Journal of Physical Chemistry Letters,* **7**, 2258 (2016).
29. T. Shiga, *et al.*, "Microscopic mechanism of low thermal conductivity in lead telluride", *Phys. Rev. B,* **85**, 155203 (2012).
30. S. Takuma, *et al.*, "Origin of anomalous anharmonic lattice dynamics of lead telluride", *Applied Physics Express,* **7**, 041801 (2014).
31. Y. Chen, X. Ai, and C. A. Marianetti, "First-Principles Approach to Nonlinear Lattice Dynamics: Anomalous Spectra in PbTe", *Phys. Rev. Lett.,* **113**, 105501 (2014).
32. C. W. Li, *et al.*, "Phonon Self-Energy and Origin of Anomalous Neutron Scattering Spectra in SnTe and PbTe Thermoelectrics", *Phys. Rev. Lett.,* **112**, 175501 (2014).
33. Y. Zhang, *et al.*, "Anomalous Lattice Dynamics near the Ferroelectric Instability in PbTe", *Phys. Rev. Lett.,* **107**, 175503 (2011).
34. H. W. Leite Alves, *et al.*, "Lattice contribution to the high dielectric constant of PbTe", *Phys. Rev. B,* **87**, 115204 (2013).
35. P. B. Littlewood, and V. Heine, "The infrared effective charge in IV-VI compounds. I. A simple one-dimensional model", *Journal of Physics C: Solid State Physics,* **12**, 4431 (1979).
36. M. P. Jiang, *et al.*, "The origin of incipient ferroelectricity in lead telluride", *Nature Communications,* **7**, 12291 (2016).

4.5 Quantum Materials

A hallmark of quantum materials is the significant role played by quantum effects in determining the exotic properties of these compounds. These solids are not adequately described by single electron band models and related theories that provided the basis for the semiconductor revolution of the 20th century. Their properties are often termed "emergent" because they cannot be directly predicted by simple consideration of the constituent particles: individual atoms, electrons, their orbitals, and spins. Rather the strong coupling of these particles leads to collective modes, exotic quantum phases and important properties such as unconventional high-temperature superconductivity, colossal magnetoresistivity, ferroelectricity, and topologically protected phases [1, 2].

The phase diagram in Figure 4.5.1 is one illustration of the scientific richness of quantum materials shown here in terms of the strength of the interactions between the lowest electronic states with other degrees of freedom, and the strength of the spin-orbit coupling. Conventional metals, band insulators and semiconductors – the mainstays of modern technology – are materials in the weak-coupling region. Here, the theory of Fermi-liquids and the conventional phase transition formalism satisfactorily explain the material properties. Quantum materials reside outside this weak-coupling region, and their properties are determined by collective modes of the electronic continuum described by the momentum-dependent dynamic structure factor $S_e(\boldsymbol{q},\omega)\sim\chi(\boldsymbol{q},\omega)$. Comprehensive direct measurements of this fundamental description of quantum matter at meV energy resolution and spanning the entire Brillouin zone have remained largely inaccessible. Understanding this rich electronic behavior will require new concepts beyond the conventional paradigms, and new experimental approaches that provide direct insight to collective modes [3, 4].

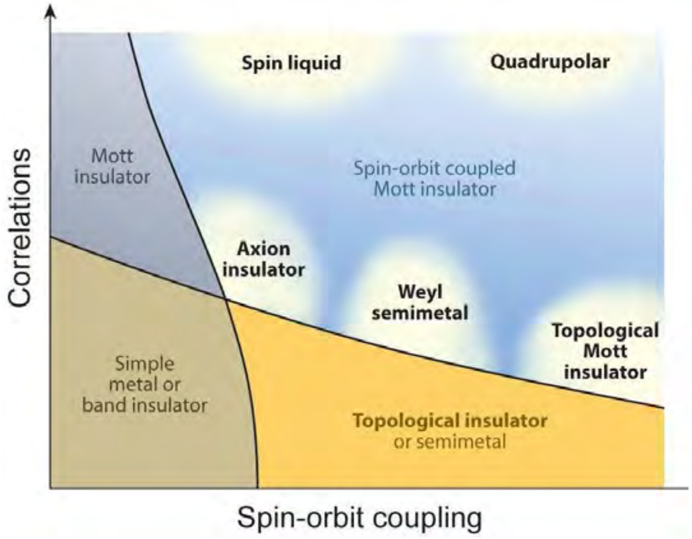

Figure 4.5.1. Schematic phase diagram for novel electronic materials and properties arising from the combination of charge correlations and spin-orbit coupling. The *5d*-transition metal oxides and diachalcogenides are the materials of choice to explore new physics enabled by spin-orbit coupling (figure adapted from reference 2).

One area of great current interest is the role of spin-orbit (S-O) coupling as an origin of new phenomena in strongly correlated materials [2, 5], particularly in the regime where the energy scale of S-O interactions is comparable to that of electron correlations. In this regime, strong S-O coupling can create a novel electronic structure that is topologically protected by quantum geometrical constraints. This introduces a new ingredient to the rich phenomena already enabled by strong correlations, such as exotic magnetism and high-T_C superconductivity. Thus, the combination of S-O coupling and strong correlation can lead to new emergent phenomena, such as topologically protected superconductivity.

Tuning and manipulating interactions in quantum materials is a second area of tremendous interest, driven in part by the development of new approaches, by the new insight this provides to the underlying physics, and by the prospect of directly controlling quantum material properties. One powerful approach is interface engineering of quantum material heterostructures [6, 7] by material synthesis with atomic precision using molecular beam epitaxy (MBE) or pulsed laser deposition (PLD). Surprising emergent phenomena have been discovered at these interfaces.

Another powerful approach is to disentangle intertwined orders (or access new phases) by perturbing quantum materials out of equilibrium via applied forces, transient magnetic fields [8], or through coherent light-matter interaction with optical or THz pulses [9-11]. Each of these approaches for manipulating interactions has the potential to provide unique insight into the collective effects that govern quantum materials, though in many cases a clear interpretation of the observed phenomena is still lacking and is being vigorously debated. Thus, exploiting these approaches requires novel experimental tools that are capable of fully characterizing the properties of quantum materials and heterostructures, both in and out of equilibrium. The capabilities of LCLS-II-HE will be indispensable for this area of research, as outlined below.

LCLS-II-HE will allow ultrahigh resolution inelastic X-ray scattering measurements with an energy resolution of a few meV using hard X-rays. In particular, the extension of the spectral range to 12 keV enables RIXS studies of the *5d* transition metal oxides [2, 5] and dichalcogenides [12, 13], which are the most compelling materials exhibiting new emergent phenomena arising from low dimensionality and the interplay between correlations and strong spin-orbit coupling. Hard X-rays from LCLS-II-HE can characterize $S_e(\boldsymbol{q},\omega)$ across the entire Brillouin zone and can provide atomic resolution (to elucidate coupling between atomic and electronic structure). Furthermore, they can penetrate materials to probe bulk properties and heterostructure interfaces, and will open new opportunities for probing samples in environments such as high-pressure cells.

4.5.1 Low energy collective excitations in 5*d* transition-metal oxides

Recently, the role of strong spin-orbit coupling in strongly correlated materials has spurred significant scientific interest because the combination of these interactions can lead to new collective effects and properties [2]. Examples include exotic magnetism, spin liquids, and unconventional topological superconductivity. The 5*d* transition-metal oxides, especially the wide variety of iridium oxides [5], are the most exciting materials in which to investigate these phenomena. The ability to fully characterize the collective excitations arising from spin, charge, lattice, and orbital degrees of freedom in these compounds is essential. To date, most crystalline 5*d* transition-metal oxide samples are limited to small single crystals or thin films, which are impractical to measure using conventional neutron scattering techniques. Thus, photon-based probes such as RIXS, IXS, and angle-resolved photoemission (ARPES) have been the primary tools to map the electronic structure in energy and momentum.

In particular, RIXS is exquisite for revealing collective excitations in the iridates [14, 15]. For example, in the Sr_2IrO_4 compound (which is isostructural to La-based superconducting cuprates), state-of-the-art RIXS measurements with an energy resolution of ~30 meV have mapped out the energy-momentum dispersion of orbital and spin wave excitations. These results reveal that the pseudospin -½ acts collectively like the Heisenberg S=½ system, reminiscent of the magnetic excitations in the high-T_C superconducting cuprates [16-18].

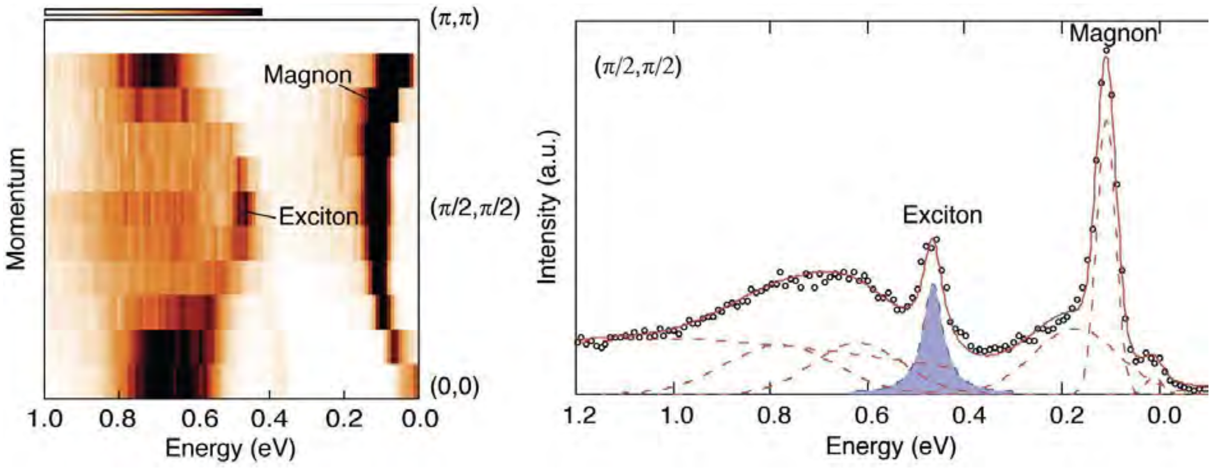

Figure 4.5.2. State-of-the-art RIXS measurement of collective modes in Sr_2IrO_4 at 30 meV resolution. Magnons and orbital excitons have been mapped in the energy-momentum space [18]. Higher spectral flux (ph/s/meV) from LCLS-II-HE will enable higher-resolution (<10 meV) and higher-fidelity maps over the entire Brillouin zone to resolve phonons and other low-energy collective excitations yet to be discovered.

Notably, new discoveries are rapidly adding new elements (and puzzles) to the emerging map of electronic states of doped Sr_2IrO_4. For example, researchers recently discovered a hidden-order state that breaks crystal inversion and rotational symmetry. This is likely associated with some sort of intra-unit-cell orbital-loop current – an exotic order previously proposed for cuprates (see Figure 4.5.3) [19]. Furthermore, ARPES studies have demonstrated that electron-doped Sr_2IrO_4 exhibits a *d*-wave gap with temperature- and momentum-dependence that is similar to *d*-wave gaps in the under-doped superconducting cuprates [20]. Further investigation of these phenomena requires high resolution RIXS measurements to uncover the underlying low-energy collective excitations that are hallmarks of the ground state. High resolution RIXS (~5 meV) at LCLS-II-HE (see Sections 3.2.5, and Appendix 2) will map low-energy charge excitations and phonon modes that are presently inaccessible and will reveal interplay effects between different degrees of freedom that are presently hidden.

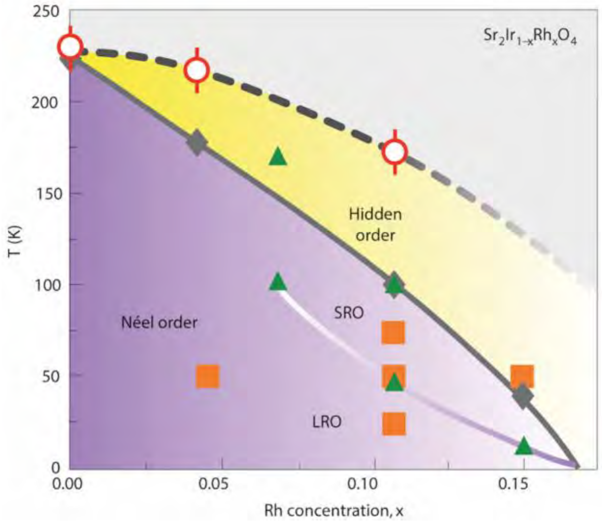

Figure 4.5.3. Phase diagram of Rh-doped Sr_2IrO_4 compounds [19]. The collective excitations associated with the mysterious “hidden order” could be revealed by high resolution RIXS at LCLS-II-HE.

High-resolution RIXS is also essential for studying the magnetic properties of frustrated magnetic systems, for example the pyrochlore $R_2Ir_2O_7$ and honeycomb A_2IrO_3 compounds. In these materials the magnetic interactions are frustrated by the lattice topology, which inhibits the development of long-range magnetic order, making them candidates to host non-trivial topological states (*e.g.* Weyl semimetals), the long-sought spin liquid state, and their proximate exotic magnetic phases [2, 5, 21]. Mapping the magnetic excitations in reciprocal space is crucial to understand these phenomena. However, the magnetic excitations of these systems are expected to reside at low energies, which cannot be adequately revealed by current state-of-the-art RIXS instruments [15, 22, 23]. Thus, the availability of a high-resolution RIXS instrument at LCLS-II-HE will significantly advance the physics of frustrated magnetism. It will further enable studies of related 5*d* transition-metal compounds such as osmium oxides and tungsten dichalcogenides, opening up a wide range of new scientific areas.

Transient fields & time-domain disentanglement of couplings

The time structure of LCLS-II-HE will enable new approaches to exploit coherent light-matter interactions by driving materials directly on the low-energy scales characteristic of phonons, magnons, polarons, and other collective modes. While conventional probes have studied the behavior of these excitations as quasi-static parameters are tuned, their nonlinear response has not been studied in detail. It is possible to use ultrafast pulses spanning the visible-to-THz regimes to induce coherent collective excitations and temporally alter the strongly intertwined degrees of freedom.

For example, recent studies have shown that broadband THz pulses can selectively couple to electronic order, and thereby transiently decouple charge and lattice modes [24]. Such approaches can also trigger phase transitions and create new phases that are inaccessible in thermal equilibrium [10, 25-27]. Tailored ultrafast vibrational excitation has been shown to drive insulator-to-metal phase transitions in colossal magnetoresistive manganites [9], photo-induced superconductivity has been reported [10], and enhanced superconductivity is claimed to result from transiently-driven nonlinear lattice dynamics in YBCO [11] and K-doped C_{60} [28].

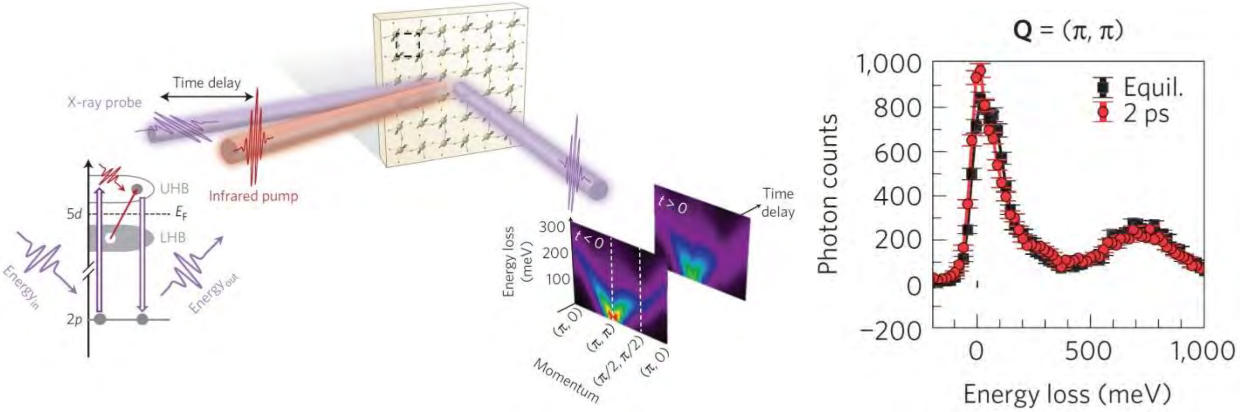

Figure 4.5.4. Left: Setup of time-resolved RIXS experiment on Sr_2IrO_4 conducted at LCLS. Right: Snapshot of RIXS spectrum at 2 ps following the pump pulse shows a subtle photo-induced change in the quasi-elastic region [29]. Due to the limitation in the average spectral flux (ph/s/meV) the measurement was performed at lower resolution and at only one time delay and two points in momentum space (only one shown here). The high repetition rate of LCLS-II-HE is essential for systematic studies in the time domain with notably higher energy resolution.

These novel photo-induced phenomena are ultimately related to the mechanisms of emergent phenomena in equilibrium and are a key step towards active control of material properties, yet a clear interpretation and characterization of the collective modes in the transient regime is still lacking. Dean *et al.* [29] have recently conducted a pioneering time-resolved RIXS measurement on Sr_2IrO_4 at LCLS (Figure 4.5.4) that illustrates the current limitations and future potential of this approach. The transient RIXS spectra reveal subtle photo-induced changes associated with magnetic excitations in the quasi-elastic region at a single $\boldsymbol{q}$ (π, π) and single time delay (2 ps) following excitation. A full characterization – at high resolution and over a range of time delays and $\boldsymbol{q}$-space – will require the ultrafast average spectral flux available from LCLS-II-HE.

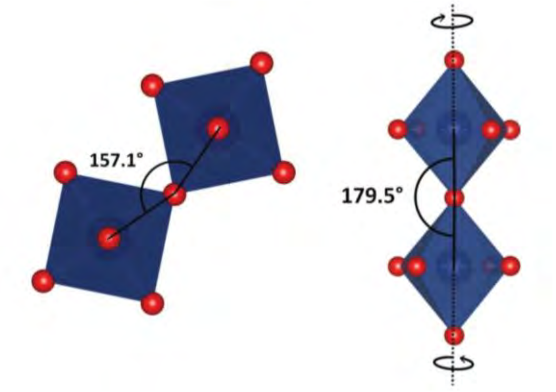

Figure 4.5.5. Crystal structure of $Sr_3Ir_2O_7$ revealing the tilting of the IrO_6 octahedrons. Such tilting is common in the iridates and is linked to the electronic structure. This provides an opportunity to manipulate the electronic structure via resonant THz pumping of the corresponding phonons (figure adapted from reference 30).

Figure 4.5.5 illustrates the crystal structure of $Sr_3Ir_2O_7$ and the tilting of the IrO_6 octahedrons which is common in the iridates and is intimately linked to the underlying electronic structure [5]. Since such octahedron tilting reduces the crystal symmetry, optical phonons are generally associated with such octahedron motions. This provides an opportunity to manipulate the electronic structure and magnetic properties via resonant THz pumping of the corresponding phonon – analogous to what has been demonstrated in the 3*d* transition metal compounds [9, 10, 31]. The combination of tailored optical/mid-IR/THz excitation pulses with RIXS capability for time/energy/momentum characterization of collective modes will be a powerful new tool for understanding the rich non-equilibrium phenomena in 5*d* transition metal oxides and related materials.

Emergent properties and pulsed magnetic fields in quantum materials

Complementing the coherent light-matter interactions described above, magnetic fields are important tuning parameters for understanding the phase diagrams of quantum materials. Thus, X-ray scattering under strong magnetic fields represents a powerful approach for understanding the abundant field-induced phenomena. High-T_C superconducting cuprates provide a prominent example that highlights the importance of this approach. In this case, the universal existence of charge density wave (CDW) correlations in the pseudogap phase [32] raises profound questions regarding the role of charge order. For example, researchers would like to know whether the CDW order is competing with or more intimately intertwined with high-T_C superconductivity (HTSC). Exploring the CDW ordering phenomena upon suppression of superconductivity by an external magnetic field provides invaluable insight into this issue.

Incorporating a capability for strong applied magnetic fields at an X-ray facility presents many significant challenges, including the limited maximum magnetic field of state-of-the-art DC magnets (up to ~20 Tesla), the complexity and inflexibility of most experimental end stations, and sample damage.

Importantly, these challenges have led to serious scientific discrepancies in our understanding of HTSC in cuprates – particularly when comparing the X-ray scattering data using a DC magnet (of modest field strength) with data from lab-based transport experiments (where fields up to ~100 Tesla have been achieved). As a result, the potential association of the CDW phase with the pseudogap phase remains a significant open question.

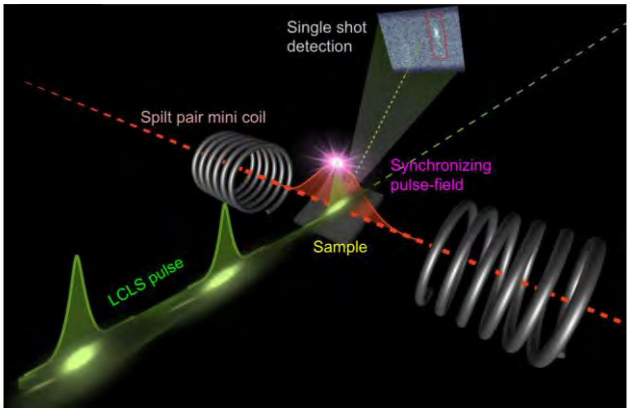

Figure 4.5.6. X-ray scattering studies of a high-temperature superconductor in the presence of a strong magnetic field at LCLS. The sample is mounted within the gap window of the split-pair pulsed magnet, and X-ray pulses are synchronized with the magnetic pulses for scattering studies. Inset: single shot scattering image of a 3D charge density wave (CDW) pattern in the superconducting cuprate YBCO in the presence of a 28 Tesla field [8].

A new approach has been developed (and recently demonstrated at LCLS), in which a high-field pulsed magnet has been integrated with an X-ray scattering experiment by taking advantage of the peak brightness and the time structure of the XFEL (see Figures 4.5.6 and 4.5.7a). The first results from this instrument reveal a surprising 3D CDW order that emerges at high magnetic fields [8]. Such experiments provide important insight into the link between CDW and HTSC, and are expected to open entirely new perspectives on other quantum materials, especially the frustrated quantum magnets [21] such as herbertsmithite [33, 34].

One significant limitation of this approach is the integrated X-ray flux that is available within the window of peak magnetic field. The pulsed magnet operates once every 20 minutes, yielding an effective duty cycle of $<10^{-6}$, as illustrated in Figure 4.5.7. This limitation renders synchrotron experiments impractical, and even the demonstration experiments at LCLS were limited to elastic scattering (compared to XPCS, IXS or RIXS approaches) from a relatively strong CDW peak.

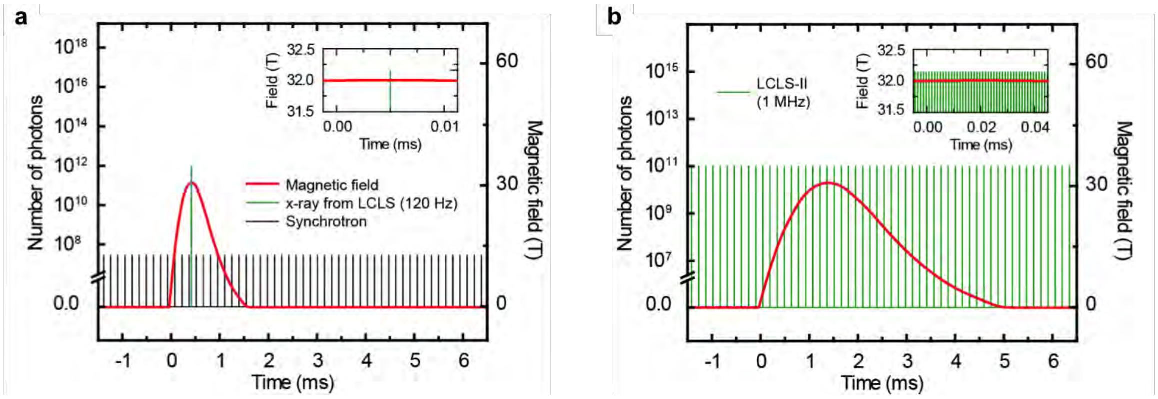

Figure 4.5.7. (a) Applied magnetic field as a function of time. The black spikes represent the gated 30 μs detection window used in synchrotron experiments. The green spike represents a single LCLS X-ray pulse with ~10^{12} photons on the sample at the peak magnetic field. (b) Alternatively, at 1 MHz repetition rate LCLS-II-HE provides 100 pulses within a 100 μs detection window.

The capabilities of LCLS-II-HE will provide a qualitative advance for studies of quantum materials in strong magnetic fields. LCLS-II-HE can deliver more than 10^{14} hard X-ray photons within the time window of the peak field, an improvement of more than 10^{6} over synchrotron sources using the same approach, and a factor of more than 10^{2} over present LCLS capabilities (see Figure 4.5.7). Furthermore, this provides access to even higher peak magnetic fields that may have shorter time windows. Significantly, successive X-ray pulses from LCLS-II-HE can map the entire field-strength dependence over the time-profile of each field pulse.

4.5.2 Emergent properties at interfaces of quantum materials heterostructures

Engineered material interfaces offer an important approach for manipulating the properties of quantum materials, and may give rise to new phenomena not observed in the bulk. To date, the focus of quantum material interfaces has been on 3*d* transition metal oxides, such as the rich phases exhibited in $LaAlO_3/SrTiO_3$ heterostructures [35, 36] and the more recent discovery of high-T_C interfacial superconductivity in monolayers of FeSe grown on $SrTiO_3$ [37-41]. Notably, there are rapidly increasing efforts (and successes) in the synthesis and characterization of 5*d* transition metal element heterostructures. For example, the monolayer transition metal dichalcogenides (such as WSe_2 and WS_2 [42]) have been shown to be direct band gap semiconductors rather than indirect band gap, as in the bulk form. This may allow for valley-dependent carrier spin polarization – a basis for valleytronic applications.

Sr_2IrO_4 is a further example where films of monolayer thickness have been synthesized and shown to exhibit both a Fermi arc [43] and a temperature-dependent *d*-wave gap (see Figure 4.5.8) [20]. With these initial successes, it is expected that an even greater variety of 5*d* transition-metal oxide heterostructures will become available in the near future. At the interface between the constituent quantum materials, new emergent phenomena are predicted due to strain, orbital reconstruction, and quantum confinement effects [6, 7]. However, direct experimental probes of the coupled electronic/atomic structure and collective modes in the interface region of heterostructures are still lacking.

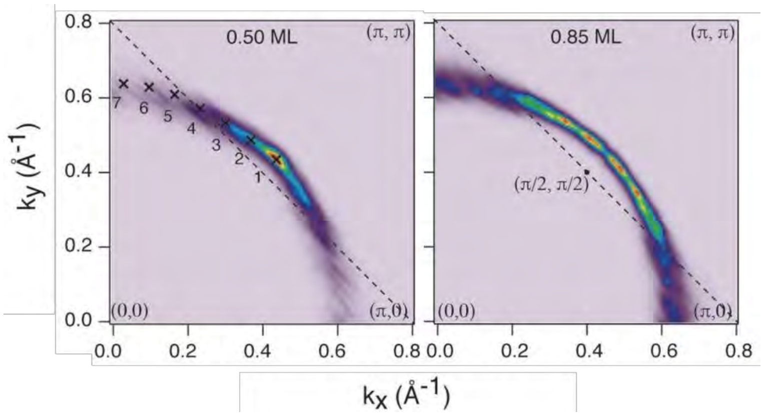

Figure 4.5.8. Fermi arc evolution as a function of the thickness of the Sr_2IrO_4 film (which is one way to vary the doping concentration). The high sensitivity of RIXS implemented at LCLS-II-HE will allow the measurement of collective excitations of these films (figure from reference 43).

The spectral flux and sensitivity of LCLS-II-HE operating at high repetition rate will enable momentum-resolved RIXS studies of monolayer systems and heterostructure interfaces. For example, high-resolution RIXS characterization of the phonon and magnetic excitations in Sr_2IrO_4 monolayer systems can be compared with theoretical models to provide further insight into the mechanism of the interfacial superconductivity. In the 2D dichalcogenide WSe_2, RIXS measurements will directly access the excitons and joint density of state at different valleys in the Brillouin zone. Importantly, element-specific information provided by tunable X-rays will be invaluable to clarify the role of the building blocks of these materials.

4.5.3 Coupled electronic and atomic structure in quantum materials

Combined ultrafast X-ray diffraction and photoemission for understanding electron-phonon coupling

Electron-phonon coupling (EPC) is one of the canonical examples of many-body interactions leading to broken-symmetry ground states such as BCS superconductivity or charge-density wave order. Previous theoretical analysis of the EPC strength in quantum materials relied on non-trivial (and sometimes biased) assumptions and was difficult to implement for multi-band systems such as ferro-pnictides. A new approach is being pioneered to extract information on the EPC purely from experiments – namely by combining time-resolved X-ray diffraction (trXRD) and time-resolved photoemission spectroscopy (trARPES).

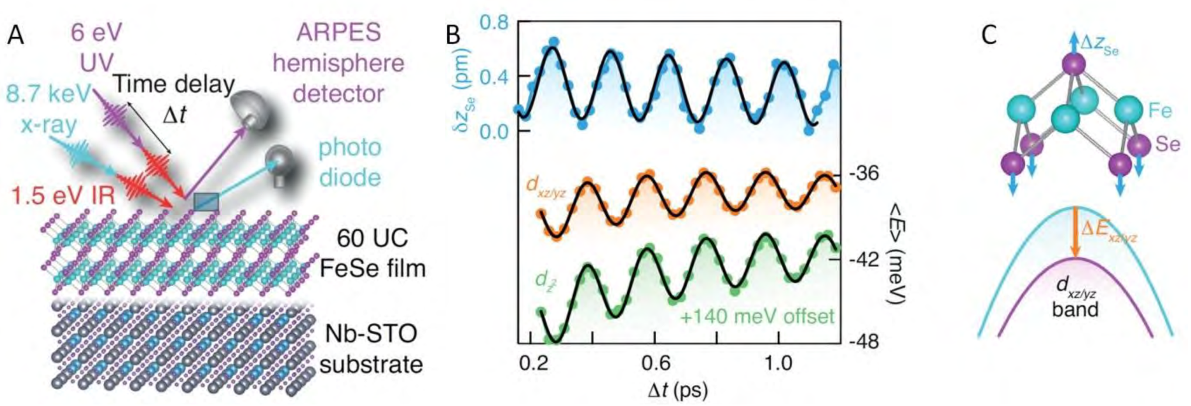

Figure 4.5.9. (A) Temporal evolution of atomic coordinates and electronic binding energies of photo-excited 60-unit-cell-thick FeSe/STO films measured via ultrafast trXRD and trARPES. (B) X-ray scattering measurement of coherent displacement of the selenium atoms δz_{Se} and momentum-averaged photoemission measurement of the energy shifts of the $d_{xz/yz}$ and d_{z2} bands. Coherent "lock-in" at the A_{1g} frequency allows a direct comparison of the lattice response and the electronic bands. (C) Schematic of the light-induced A_{1g} coherent phonon mode that corresponds to a periodic displacement of selenium atoms (top) and results in a periodic modulation of the electronic binding energies (bottom) (Gerber *et al.* unpublished)

In demonstration experiments, the deformation potential in bulk-like, FeSe films that are 60 unit cells thick has been benchmarked by measuring the light-induced coherent motion of the crystal lattice by trXRD and the corresponding dynamics of the electronic band energy by trARPES. Connecting the two measurements via the A_{1g} optical phonon frequency defines a "coherent lock-in" experiment, which determines the deformation potential with a precision down to ~1 meV/pm. The experimental values for the deformation potential can be explained theoretically only when correlation effects are included via dynamical mean-field theory calculations of the band structure. This leads to a complex orbital-dependent EPC, which is much larger than expected from conventional density functional theory. This understanding is corroborated by an unexpected hardening of the A_{1g} mode at much higher pump fluences: correlations decrease with increasing fluence in this nonlinear regime and thus limit the influence of magnetism on the electronic and phononic structure. This early work explicitly demonstrates the need to include correlation effects to obtain the correct lattice and electronic structure, which in turn has unexpected yet profound consequences for the EPC in ferro-pnictides.

The simultaneous combination of trXRD and trARPES will enable a much deeper understanding of the coupling between atomic and electronic structure – both in and out of equilibrium – across broad classes of quantum materials. This approach is an important complement to RIXS/IXS, and LCLS-II-HE capabilities will be indispensable. Diffraction with hard X-rays is essential to discern sub-Å atomic displacements, photoemission with hard X-rays is essential to provide bulk sensitivity (matching the probe volume of trXRD), and high repetition rate is essential to avoid space charge effects and compensate for the dramatic loss of photoemission cross section with increasing photon energies [44-46].

Non-equilibrium control of nanoscale spin-lattice coupling

The prospect of manipulating materials' properties with femtosecond laser pulses and the demand for faster information storage and processing have fueled research on the ultrafast manipulation of magnetic order, resulting in important discoveries of femtosecond demagnetization and all-optical magnetic switching. However, understanding when and how optical energy delivered to valence electrons is transferred to spin and lattice degrees of freedom remains among the most challenging and important topics in condensed matter physics.

While femtosecond soft X-ray pulses have been successfully used to probe the non-equilibrium angular momentum transfer between magnetic subsystems [47] and on the nm length scale [48], the interaction with the lattice is often neglected. It is commonly thought that magnetic properties respond to lattice rearrangements, such as strain [49], rather than the reverse. Figure 4.5.10 provides the first indication that ultrafast changes of magnetic order can directly couple to and drive the lattice. The figure shows the extremely anisotropic lattice expansion along a-, b-, and c-axes of FePt, the prototype material for next-generation magnetic data storage media, following ultrafast photo-excitation [50]. Lattice expansion within the initial 3 ps is thought to be driven by electronic stress [51]. Stress due to non-equilibrium phonon populations occurs usually on a longer timescale. However, the results in Figure 4.5.10 for the FePt case reveal for the first time that magnetic stress can also drive the observed anisotropic lattice expansion as predicted by first-principles calculations [50]. Such measurements provide the blueprint for groundbreaking studies in many systems, ranging from metallic alloys [52] to colossal magnetoresistive oxides, [9, 53] to disentangle the driving force behind photo-induced changes in magnetic and lattice order.

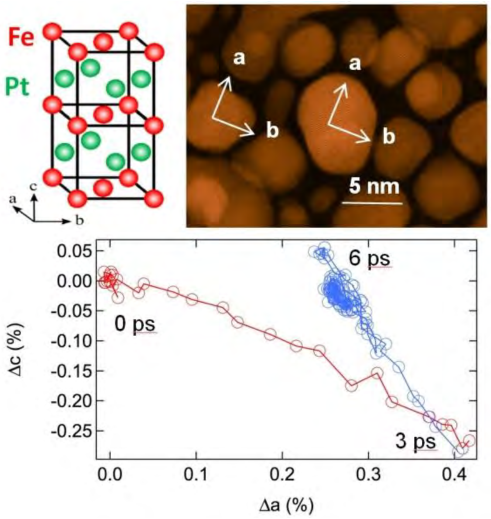

Figure 4.5.10. Lattice structure (top left) and transmission electron microscopy image of morphology (top right) of granular FePt materials, the likely candidates for future magnetic data storage media. The ultrafast lattice response (bottom) is composed of an initial c-axis contraction (red lines and symbols) in response to ultrafast demagnetization followed after 3ps by an expansion due to the population of nonequilibrium phonons (blue lines and symbols). [50].

Using hard X-rays from LCLS it was recently possible to directly detect the propagating strain waves during the first few picoseconds after photo-excitation. Figure 4.5.11 displays the surprisingly sharp

(~100 fs) strain wave fronts that were reconstructed from THz coherent phonon oscillations detected in diffuse hard X-ray scattering [51]. The temporal width of the strain front is of the order of electronic and spin relaxation times and hints at the highly non-equilibrium nature of the involved electron-lattice coupling. This opens up novel ways to manipulate the electron and spin systems via ultrasharp strain waves generated in different parts of the sample or in adjacent layers. Applications may range from ultrafast magneto-elastic switching to novel ways to control multiferroic materials and heterostructures.

Currently sensitivity and information content of such studies are limited by the heat load due to the high single-pulse X-ray fluences required to accumulate sufficient statistics at 120 Hz. Such measurements at very high repetition rates at LCLS-II-HE will drive a major advance in this area. The combination of fully coherent XFEL pulses with high repetition rates should enable coherent diffractive imaging of ultrafast strain waves propagating in much smaller nanoparticles than what is currently feasible at 120 Hz [1].

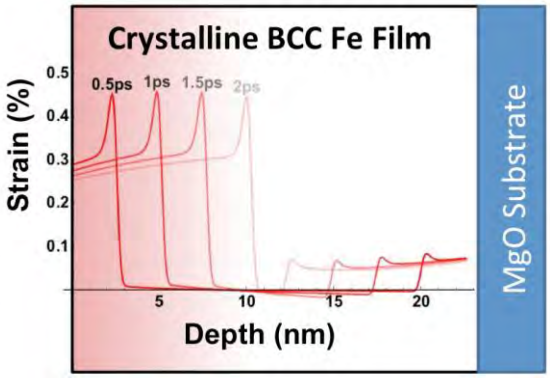

Figure 4.5.11. Spatial profile of the lattice strain developing after ultrafast photo-excitation of an Fe film. The red solid lines represent strain profiles obtained by fitting the experimental observation of coherent phonon modes up to 3.5 THz [2]. The red shading schematically represents the electron temperature profile (which follows the laser penetration profile) just after excitation. (H. Durr *et al.* unpublished)

References

1. E. Dagotto, "Complexity in strongly correlated electronic systems", *Science,* **309**, 257 (2005).
2. W. Witczak-Krempa*, et al.*, "Correlated Quantum Phenomena in the Strong Spin-Orbit Regime", *Annual Review of Condensed Matter Physics,* **5**, 57 (2014).
3. G. Fleming, and M. Ratner, "Directing Matter and Energy: Five Challenges for Science and the Imagination - BESAC Report U.S. D.O.E.," (http://science.energy.gov/bes/news-and-resources/reports/abstracts/#GC, 2007).
4. J. C. Hemminger, "Challenges at the Frontiers of Matter and Energy: Transformative Opportunities for Discovery Science - BESAC Report U.S. D.O.E.," (http://science.energy.gov/~/media/bes/besac/pdf/Reports/CFME_rpt_print.pdf, 2015).
5. J. G. Rau, E. K.-H. Lee, and H.-Y. Kee, "Spin-Orbit Physics Giving Rise to Novel Phases in Correlated Systems: Iridates and Related Materials", *Annual Review of Condensed Matter Physics,* **7**, 195 (2016).
6. E. Dagotto, "When Oxides Meet Face to Face", *Science,* **318**, 1076 (2007).
7. J. Chakhalian, A. J. Millis, and J. Rondinelli, "Whither the oxide interface", *Nat Mater,* **11**, 92 (2012).
8. S. Gerber*, et al.*, "Three-dimensional charge density wave order in $YBa_2Cu_3O_{6.67}$ at high magnetic fields", *Science,* **350**, 949 (2015).
9. M. Rini*, et al.*, "Control of the electronic phase of a manganite by mode-selective vibrational excitation", *Nature,* **449**, 72 (2007).
10. D. Fausti*, et al.*, "Light-Induced Superconductivity in a Stripe-Ordered Cuprate", *Science,* **331**, 189 (2011).
11. R. Mankowsky*, et al.*, "Nonlinear lattice dynamics as a basis for enhanced superconductivity in $YBa_2Cu_3O_{6.5}$", *Nature,* **516**, 71 (2014).
12. W. Zhao*, et al.*, "Evolution of Electronic Structure in Atomically Thin Sheets of WS_2 and WSe_2", *ACS Nano,* **7**, 791 (2013).
13. S. Das*, et al.*, "Beyond Graphene: Progress in Novel Two-Dimensional Materials and van der Waals Solids", *Annual Review of Materials Research,* **45**, 1 (2015).
14. B. J. Kim*, et al.*, "Phase-Sensitive Observation of a Spin-Orbital Mott State in Sr_2IrO_4", *Science,* **323**, 1329 (2009).

15. J. P. Clancy, *et al.*, "X-ray scattering study of pyrochlore iridates: Crystal structure, electronic, and magnetic excitations", *Phys. Rev. B,* **94**, 024408 (2016).
16. J. Kim, *et al.*, "Magnetic Excitation Spectra of Sr_2IrO_4 Probed by Resonant Inelastic X-Ray Scattering: Establishing Links to Cuprate Superconductors", *Phys. Rev. Lett.,* **108**, 177003 (2012).
17. S. Fujiyama, *et al.*, "Two-Dimensional Heisenberg Behavior of J_{eff}=1/2 Isospins in the Paramagnetic State of the Spin-Orbital Mott Insulator Sr_2IrO_4", *Phys. Rev. Lett.,* **108**, 247212 (2012).
18. J. Kim, *et al.*, "Excitonic quasiparticles in a spin–orbit Mott insulator", *Nat Commun,* **5**, 4453 (2014).
19. Y. Y. Kang, *et al.*, "Crystal structure of rhodopsin bound to arrestin by femtosecond X-ray laser", *Nature,* **523**, 561 (2015).
20. Y. K. Kim, *et al.*, "Observation of a d-wave gap in electron-doped Sr_2IrO_4", *Nat Phys,* **12**, 37 (2016).
21. L. Balents, "Spin liquids in frustrated magnets", *Nature,* **464**, 199 (2010).
22. H. Gretarsson, *et al.*, "Crystal-Field Splitting and Correlation Effect on the Electronic Structure of A_2 IrO_3", *Phys. Rev. Lett.,* **110**, 076402 (2013).
23. S. Hwan Chun, *et al.*, "Direct evidence for dominant bond-directional interactions in a honeycomb lattice iridate Na_2IrO_3", *Nat Phys,* **11**, 462 (2015).
24. M. Porer, *et al.*, "Non-thermal separation of electronic and structural orders in a persisting charge density wave", *Nat Mater,* **13**, 857 (2014).
25. F. Schmitt, *et al.*, "Transient electronic structure and melting of a charge density wave in $TbTe_3$", *Science,* **321**, 1649 (2008).
26. J. P. Hinton, *et al.*, "New collective mode in $YBa_2Cu_3O_{6+x}$ observed by time-domain reflectometry", *Phys. Rev. B,* **88**, 060508 (2013).
27. L. Stojchevska, *et al.*, "Ultrafast Switching to a Stable Hidden Quantum State in an Electronic Crystal", *Science,* **344**, 177 (2014).
28. M. Mitrano, *et al.*, "Possible light-induced superconductivity in K_3C_{60} at high temperature", *Nature,* **530**, 461 (2016).
29. M. P. M. Dean, *et al.*, "Ultrafast energy- and momentum-resolved dynamics of magnetic correlations in the photo-doped Mott insulator Sr_2IrO_4", *Nat Mater,* **15**, 601 (2016).
30. T. Hogan, *et al.*, "Structural investigation of the bilayer iridate $Sr_3Ir_2O_7$", *Phys. Rev. B,* **93**, 134110 (2016).
31. K. W. Kim, *et al.*, "Ultrafast transient generation of spin-density-wave order in the normal state of $BaFe_2As_2$ driven by coherent lattice vibrations", *Nat Mater,* **11**, 497 (2012).
32. R. Comin, and A. Damascelli, "Resonant X-Ray Scattering Studies of Charge Order in Cuprates", *Annual Review of Condensed Matter Physics,* **7**, 369 (2016).
33. T.-H. Han, *et al.*, "Fractionalized excitations in the spin-liquid state of a kagome-lattice antiferromagnet", *Nature,* **492**, 406 (2012).
34. S. Nishimoto, N. Shibata, and C. Hotta, "Controlling frustrated liquids and solids with an applied field in a kagome Heisenberg antiferromagnet", *Nat Commun,* **4**, 2287 (2013).
35. A. Ohtomo, and H. Y. Hwang, "A high-mobility electron gas at the $LaAlO_3/SrTiO_3$ heterointerface", *Nature,* **427**, 423 (2004).
36. S. Okamoto, and A. J. Millis, "Electronic reconstruction at an interface between a Mott insulator and a band insulator", *Nature,* **428**, 630 (2004).
37. Q.-Y. Wang, *et al.*, "Interface-Induced High-Temperature Superconductivity in Single Unit-Cell FeSe Films on $SrTiO_3$", *Chinese Physics Letters,* **29**, 037402 (2012).
38. D. Liu, *et al.*, "Electronic origin of high-temperature superconductivity in single-layer FeSe superconductor", *Nat Commun,* **3**, 931 (2012).
39. S. He, *et al.*, "Phase diagram and electronic indication of high-temperature superconductivity at 65 K in single-layer FeSe films", *Nat Mater,* **12**, 605 (2013).
40. S. Tan, *et al.*, "Interface-induced superconductivity and strain-dependent spin density waves in FeSe/$SrTiO_3$ thin films", *Nat Mater,* **12**, 634 (2013).
41. J. J. Lee, *et al.*, "Interfacial mode coupling as the origin of the enhancement of T_c in FeSe films on $SrTiO_3$", *Nature,* **515**, 245 (2014).
42. W. J. Yu, *et al.*, "Vertically stacked multi-heterostructures of layered materials for logic transistors and complementary inverters", *Nat Mater,* **12**, 246 (2013).
43. Y. K. Kim, *et al.*, "Fermi arcs in a doped pseudospin-1/2 Heisenberg antiferromagnet", *Science,* **345**, 187 (2014).
44. V. N. Strocov, *et al.*, "Soft-X-ray ARPES facility at the ADRESS beamline of the SLS: concepts, technical realisation and scientific applications", *Journal of Synchrotron Radiation,* **21**, 32 (2014).

45. S. Suga, and C. Tusche, "Photoelectron spectroscopy in a wide hν region from 6 eV to 8 keV with full momentum and spin resolution", *JESRP,* **200**, 119 (2015).
46. A. X. Gray*, et al.*, "Probing bulk electronic structure with hard X-ray angle-resolved photoemission", *Nat Mater,* **10**, 759 (2011).
47. I. Radu*, et al.*, "Transient ferromagnetic-like state mediating ultrafast reversal of antiferromagnetically coupled spins", *Nature,* **472**, 205 (2011).
48. C. E. Graves*, et al.*, "Nanoscale spin reversal by non-local angular momentum transfer following ultrafast laser excitation in ferrimagnetic GdFeCo", *Nat Mater,* **12**, 293 (2013).
49. J.-W. Kim, M. Vomir, and J.-Y. Bigot, "Ultrafast Magnetoacoustics in Nickel Films", *Phys. Rev. Lett.,* **109**, 166601 (2012).
50. X. S. A. H. Reid, P. Maldonado, T. Chase, E. Jal, P. Granitzka, K. Carva, R. K. Li, J. Li, L. Wu, T. Vecchione, T. Liu, Z. Chen, D.J. Higley, N. Hartmann, R. Coffee, J. Wu, G.L. Dakowski, W. Schlotter, H. Ohldag, Y.K. Takahashi, V. Mehta, O. Hellwig, A. Fry, Y. Zhu, J. Cao, E.E. Fullerton, J. Stöhr, P. M. Oppeneer, X.J. Wang, H.A. Dürr, "Ultrafast spin-lattice coupling in laser-excited FePt nanoparticles", *arXiv:1602.04519,* (2016).
51. T. Henighan*, et al.*, "Generation mechanism of terahertz coherent acoustic phonons in Fe", *Phys. Rev. B,* **93**, 220301 (2016).
52. S. O. Mariager*, et al.*, "Structural and Magnetic Dynamics of a Laser Induced Phase Transition in FeRh", *Phys. Rev. Lett.,* **108**, 087201 (2012).
53. T. Li*, et al.*, "Femtosecond switching of magnetism via strongly correlated spin-charge quantum excitations", *Nature,* **496**, 69 (2013).

4.6 Matter in Extreme Environments

In the field of high-energy-density physics and high-power high-intensity laser-matter interactions, LCLS-II-HE will enable new experiments with high impact. The most important scientific questions are related to the physical and structural properties of extreme states of matter that can be produced only in dynamic experiments lasting a billionth of a second, and in very small quantities. The combination of high repetition rates and hard X-rays from LCLS-II-HE will generate high-resolution spectroscopic and structural information of matter in extreme states that has previously been inaccessible. Although most of these studies are discovery-class science, measurements in the areas of extreme materials will be important for applications related to fusion and fission materials and will lead to important insights into planetary physics and geoscience. Here, high peak brightness combined with high repetition rates and high X-ray energies are required to:

- Penetrate through dynamically heated dense targets and diamond anvil cells (DACs).
- Generate high signal-to-noise data above the self-emission bremsstrahlung background.
- Probe atomic scale lengths at large wavenumbers that reveal structure and material phases.

These studies will further require the coupling of LCLS-II-HE with optical pump lasers. High-repetition-rate lasers with mJ pulse energies that match the repetition rate of the X-ray beam exist for dynamic pump-probe measurements. In addition, LCLS-II-HE will enable experiments that employ X-ray pump and X-ray probe techniques using two-color operation or multiple X-ray pulses with advanced detectors. Use of LCLS-II-HE and the experimental requirements are consistent with:

- Data that exist from LCLS or synchrotron sources that demonstrate that LCLS-II-HE provides sufficient photon flux to achieve the scientific goals.
- Novel target technologies that have been developed and are suitable for producing matter in extreme conditions compatible with high repetition rates.

New developments in target technology include cryogenic jets, gas jets, and dynamic DACs to access dense cryogenic hydrogen, light and heavy liquids including water, and high-Z matter including tungsten or composite steels used in extreme radiation environments. It is especially important to accurately measure the equation of state (EOS), which requires precision data on compression and material phase transitions for which X-ray diffraction enabled by XFELs is the method of choice. These techniques are also suitable for characterizing stacking faults or discovering entirely new materials and material phases. Important examples include metallic phases of hydrogen, high-pressure electride states, nano-diamonds and harder diamonds (londsdaleites).

Besides the discovery and characterization of the material structural properties, LCLS-II-HE will further enable measurements of the physical properties including strength, optical, and transport properties. Inelastic X-ray scattering techniques and angularly resolved X-ray scattering are the techniques of choice and have been demonstrated to provide information about conductivity, electron temperature, density, and the ionization state. Accurate data of super-ionic phases and the conductivity of warm dense matter are especially important for hydrodynamic modeling of fusion plasmas, laboratory astrophysics experiments, and intense laboratory radiation sources.

4.6.1 Structure and equation of state of matter at megabar pressures

Dense hydrogen

Hydrogen is the simplest and most abundant of all the elements, and yet its behavior at high density is extremely complicated and still not well understood. It has long been theorized that under sufficient compression the hydrogen molecule will dissociate, resulting in an atomic form [1]. This atomic form has been predicted to have a liquid ground state [2] with exotic properties such as superconductivity and superfluidity [3].

Hydrogen also exhibits several other unusual behaviors at high density, such as an extremely pronounced temperature minimum in the melting point of the molecular solid above 250 GPa [4]. This minimum is also a feature of the alkali metals such as lithium [5], and, as is the case in the alkali metals, is accompanied by the emergence of several complex solid phases near the minimum [6].

There is also a proposed liquid-liquid insulator-metal transition (LL-IMT) in hot liquid hydrogen, attributed to the transformation from a molecular to an atomic liquid. The exact condition under which this transition occurs is disputed both in theory and experiment [7, 8].

There is very little structural information available on hydrogen, and none outside the three hexagonal close-packed-like phases I, II and III [9, 10]. This is due to the very low X-ray scattering intensity of hydrogen, such that even with the best modern synchrotrons it is very difficult to obtain an acceptable signal. The high brightness of LCLS-II-HE will open the way to many novel experiments for revealing the nature of dense hydrogen, in addition to other low-Z materials such as deuterium, lithium, lithium hydride, and helium. Here, a laser-pulsed DAC will be invaluable for probing this element at elevated temperature.

The fundamental understanding of hydrogen is also important for applications. Examples include planetary physics and inertial confinement fusion. Peculiar liquid-liquid and metallic transformations might occur inside giant gas planets like Jupiter, whose interior is comprised largely of liquid hydrogen. At high pressure and temperature, this material switches from its normal electrically insulating state into a conducting (metallic) phase. Experiments will need to rapidly heat a compressed sample of liquid deuterium and use LCLS-II-HE X-rays to probe the subsequent structural changes.

Figure 4.6.1. An artist's conception shows the Juno spacecraft arrival at Jupiter. LCLS-II-HE experiments on the structure of dense hydrogen will accurately determine the equation of state, the material phases, and phase transition regions. The data are expected to characterize the much-contested metallic state and help determine if Jupiter has a solid core. The latter question is important for our understanding of the evolution of the planetary system.

The dense hydrogen properties of Jupiter play an important role in determining the evolution of our planetary system. The goal of the Juno mission (the Juno spacecraft arrived at Jupiter in July 2016) is to perform precision measurements of the magnetic field and the interior mass distribution of Jupiter. An accurate EOS will then be needed to make estimates of Jupiter's core. A solid core would indicate that a rocky planet swept up the initial hydrogen in our planetary system. On the other hand, a non-rocky core would indicate that the giant gas planets were formed due to gravitational instabilities.

The phase diagram of dense hydrogen shows that there is wide disagreement about the conditions under which dense liquid hydrogen will dissociate in the LL-IMT. Both experiment and theory indicate different conditions. Furthermore, there is complete lack of structural data on phase IV and any higher phases, and only very limited data on phase III. The existence of phase I is suggested by changes in the behavior of the vibron in phase I above 200 GPa, but structural data is needed to understand this phase.

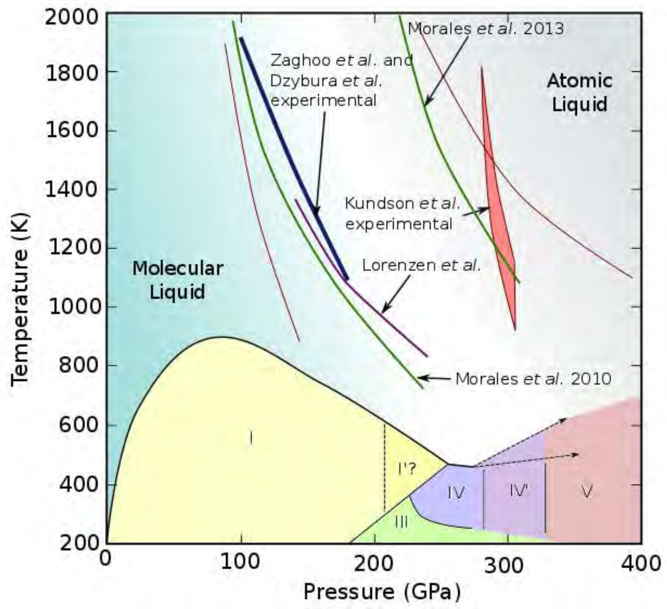

Figure 4.6.2. Phase diagram of hydrogen. Solid phases and melting curve are from [4, 6]. Curves in liquid conditions show the proposed LL-IMT transitions. Blue shows the experimental results from [7, 11], red region shows experimental results from [8] with thin red lines showing the two extremes of the range of the transition curves calculated in that study. Green curves are calculations by Morales *et al.*[12, 13]. Purple curve is calculated in [14].

LCLS-II-HE will enable the structural investigation of the dense hydrogen phase diagram. The high peak brightness combined with high photon flux will allow data collection from small hydrogen samples. Tight focusing is particularly important, as the DAC gasket in the cell is made from rhenium which scatters over 5600 times more intensely than hydrogen. It is therefore vital that the X-rays be well-focused on the sample and not impinge on the gasket. Smaller samples allow access to higher pressure and high temperature, where gasket stability and containment are more difficult.

It should be noted that due to absorption in the diamond anvils and the limited observable range of scattering angles, 2θ, (due to the aperture of the cell) hard X-rays above 10 keV are required for DAC studies.

The new LCLS-II-HE capabilities will allow probing of hydrogen at and above room temperature at pressures up to 200 GPa. This covers a region where a change in the sign and magnitude of $\partial \nu / \partial P$, the rate of change of vibron frequency with pressure, is observed in the solid phase I [4], and where at high temperature the LL-IMT may be observed [7]. It is also important to pursue the first-ever diffraction data on hydrogen phase IV above 220 GPa at room temperature. Phase IV is predicted to have an unusual layered structure which appears to be a prelude to metallization [15-17]. Such data is much needed to confirm or disprove theoretical models of this phase.

The pulsed nature of LCLS-II-HE is also useful for high-temperature experiments in which the containment of hydrogen and integrity of the diamond anvils are both problematic. By using pulsed laser heating, the sample can be briefly brought to high temperature to coincide with the X-ray pulses from LCLS-II-HE, thus allowing measurement of hydrogen at high *P*-*T* conditions without losing the sample from diffusion or containment failure. Such pulsed laser heating of DACs has been described elsewhere, including for use with hydrogen [11, 18, 19].

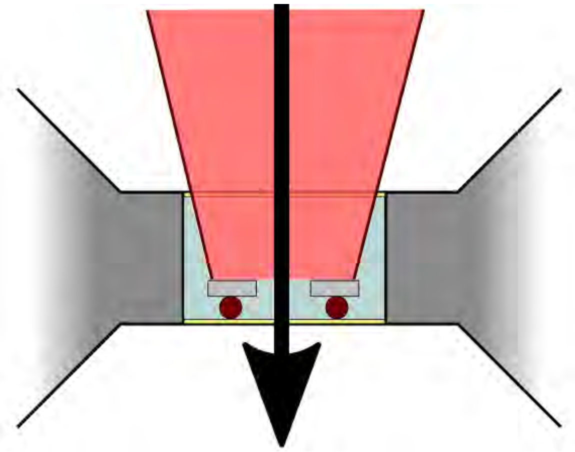

Figure 4.6.3. DAC setup with diamond anvils (white), rhenium gasket (dark grey), hydrogen-proof diamond protection (yellow), and loaded with a hydrogen sample (blue). Before loading, an annular thin metal foil (light grey) is placed in the sample chamber suspended on ruby spheres (dark red) which allow measurement of pressure. A pulsed laser (pale red) is focused onto the coupler to isochorically heat the sample. Hydrogen in the central section of the ring is heated from all sides while the hole allows the X-ray pulse (black arrow) to pass through hot dense hydrogen without diffraction from the coupler.

To date, no direct measurement has been made on hydrogen over the LL-IMT. Rather, studies have used VISAR [8] or the temperature of a laser coupler [7, 11]. A direct measure would be an important advancement in hydrogen physics and could reveal more of the nature of this transition, which would settle the many disagreements in experiment and theory. A cross section schematic of a diamond anvil cell suited to this experiment is shown in Figure 4.6.3.

Liquid jets

Cryogenic liquid jet targets are a new source that is now becoming available for high-repetition rate experiments that require high photon flux and integrate over many pulses. In particular, hydrogen micro-jets have recently been shown to provide excellent targets to study extreme material states. In addition to hydrogen jets, deuterium, methane, neon and argon jets have recently become available. These jets offer great opportunities for X-ray pump and X-ray or optical probe studies of isochorically-heated matter (see Figure 4.6.4).

Moreover, these jets provide a new way to access non-equilibrium states. Micrometer hydrogen jets operate by shooting a stream of liquid hydrogen several micrometers in diameter into a vacuum, at which point evaporative cooling from the surface rapidly crystallizes the jet. Raman scattering studies indicate that the rapidly crystallized hydrogen includes a significant fraction of face-centered cubic (fcc) crystallites in addition to hexagonally close-packed (hcp) ones. Intriguingly, it appears that the fcc fraction that is visible in the Raman spectrum may be due to a high concentration of stacking defects in the hcp lattice. The high thermal expansion coefficient of hydrogen may also build up strain in the hcp lattice, causing similar effects.

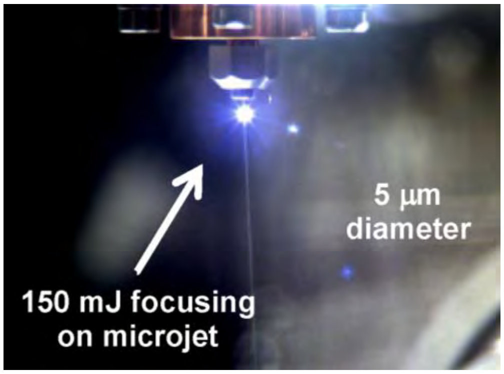

Figure 4.6.4. A continuously flowing cryogenic hydrogen jet is shown. The jet expands into the vacuum at 100 m/s, suitable for high-repetition rate pump-probe experiments. The image shows blue emission from hydrogen that was heated by a 40 fs short-pulse laser a few millimeters under the nozzle.

X-ray extension to high-Z dense matter physics

The high flux available at LCLS-II-HE is also well suited to investigate other light elements, *e.g.* Li and He, and light compounds such as LiH. Lithium exhibits cold melting under pressure [5], much like hydrogen. It is observed to melt on isothermal compression from a close-packed fcc structure, showing a massive failing of the hard spheres model. With the increased flux of LCLS-II-HE it may be possible to obtain liquid diffraction data from lithium to see if there is a change in the liquid structure over the melting maxima – the flux of current synchrotron sources does not allow this measurement to be made. It will also be possible to explore the high-pressure and high-temperature region of the phase diagram, which is as yet unknown. The phase diagram of lithium is shown in Figure 4.6.5.

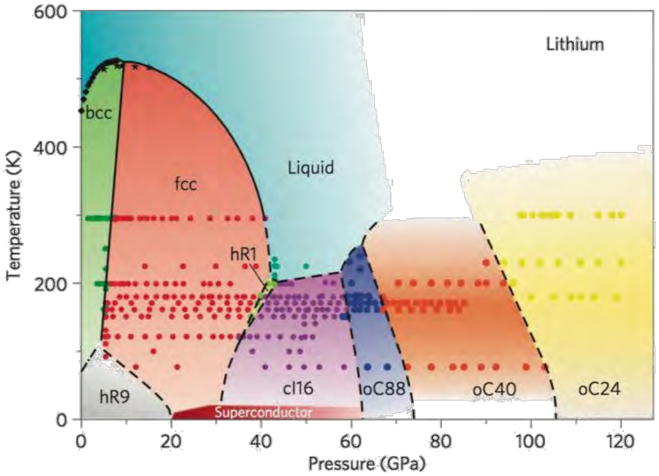

Figure 4.6.5. The phase diagram of lithium [5]. The dots indicate diffraction data mostly in the solid phases. No data currently exist in the high temperature regimes because they require smaller samples and pulsed heating due to containment issues. Further, measuring liquid diffraction structure factors will require much larger X-ray flux than currently available.

The short pulse duration of LCLS-II-HE may enable following phase transitions in real time. By using a dynamic DAC, in which a piezoelectric element is included to provide additional load on the cell, pressure can be rapidly cycled or increased at very high rates (~500GPa/s). Such devices are described elsewhere [20]. By tuning the pressure such that a phase transition of interest is repeatedly crossed it may be possible to observe the mechanisms of pressure driven phase transitions in real time [21].

4.6.2 Physical properties of matter in extreme conditions

LCLS-II-HE will provide the capability to accurately probe the dynamic structure factor of warm dense matter with unprecedented precision. These studies are important to understand the intrinsic properties of radiation hydrodynamics. Accurate data on radiation transport, opacity, electrical conductivity, and thermal conductivity are all of high interest and urgently needed for modeling of matter in extreme conditions. In recent years, density functional theory has been successfully applied to warm dense matter studies, but experiments are needed to determine the functional and to develop physics models that can be applied in this difficult regime.

Structure factor

The structure factor is a central quantity for calculations of particle and radiation transport coefficients. Moreover, electron-ion collisions and the ion excess pressure are directly related to the structure factor. Thus, calculations of the equation of state, spectral line-broadening and particle stopping powers depend on our knowledge of this quantity. LCLS-II-HE will further develop angularly-resolved X-ray scattering techniques that have previously been used to directly measure the structure factor in warm dense matter [22].

In particular, the high repetition rates will allow measurements on states of warm dense matter, such as warm dense hydrogen, that provide only small scattering signals. Figure 4.6.6 shows predictions from density functional theory for X-ray scattering measurements, comparing the signal from correlated molecules, partially dissociated hydrogen, and a metallic hydrogen state. The figure illustrates that these measurements will provide a unique signature of the material state and will allow inference of the physical properties.

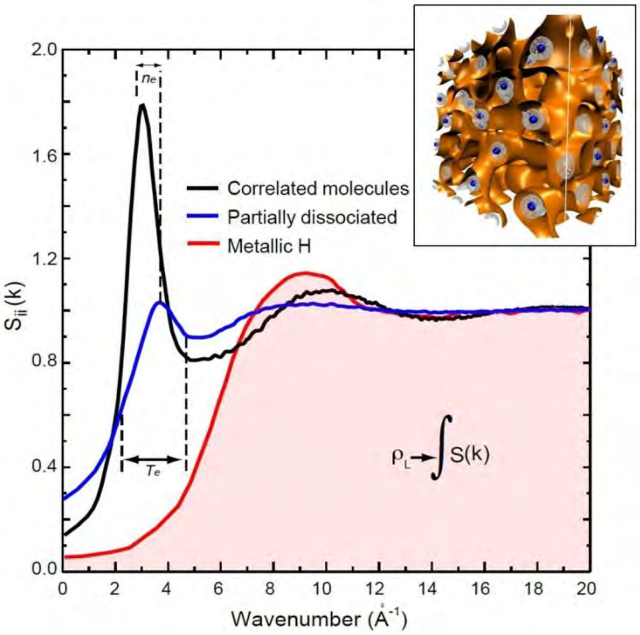

Figure 4.6.6. Ion-ion structure factor for compressed liquid hydrogen as a function of shock conditions along the Hugoniot as modeled using DFTMD. The black line is the structure factor from molecular hydrogen demonstrating a strong H-H correlation. The blue line is from a partially dissociated plasma with some quasi metallic and insulating properties. The red line is from a correlated metallic plasma indicative of total dissociation. Inset: Simulation example from density functional theory. The golden iso-contours show the electron state in warm dense matter that give rise to strong correlation peaks in the structure factor.

It is important to note that in recent years several theories have been developed to estimate structure factors for use in simulations codes. Experiments have shown that simple estimates based on Thomas-Fermi functionals are not accurate and only Kohn-Sham functionals with detailed configuration accounting provides correct estimates [23]. However, such calculations need large computing resources and can only be performed for specific experimental data points. Consequently, accurate experimental data that test efficient theoretical approximations in this regime are needed to develop the modeling tools for warm dense matter.

Plasmon scattering

Spectrally-resolved X-ray scattering techniques have recently been demonstrated at LCLS to directly measure plasmons [24]. This capability exists for isochorically-heated matter either using single X-ray pulses, two-color operations, or X-ray bursts. The capabilities of LCLS-II-HE will enable plasmon measurements to determine the correct functionals for density functional theory coupled to molecular dynamics (DFT-MD) simulations of warm dense matter. These studies require X-ray scattering data with sufficiently low noise to distinguish subtle differences in plasmon damping predicted for conditions that can be accessed by LCLS-II-HE. Figure 4.6.7 shows results for the conductivity of warm dense aluminum. The calculations indicate the sensitivity of plasmon damping on non-Drude dissipative processes that cannot be treated with perturbation theory. Such findings will be important for the study of strongly coupled plasmas.

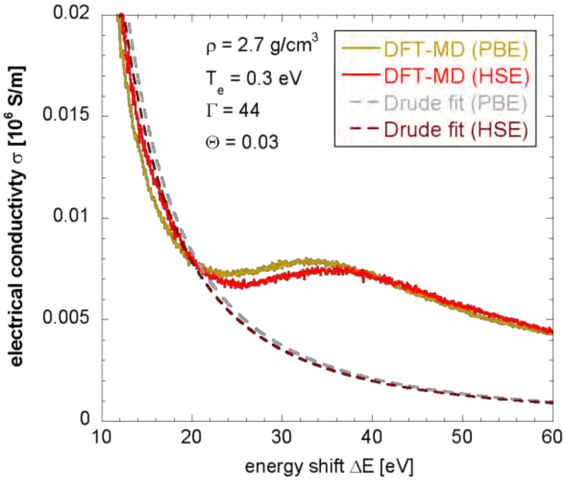

Figure 4.6.7. The dynamical electrical conductivity is shown for warm dense aluminum. The calculations use DFT-MD simulations, applying the PBE functional after Perdew, Burke, and Ernzerhof [25] and HSE functional after Heyd, Scuseria and Ernzerhof [26] at a temperature of T = 0.5 eV. The non-Drude-like behavior of aluminum for $\Delta E > 20$ eV is evident by the deviations from the Drude fits to the simulations. Testing these theories will require highly accurate measurements with high photon flux that precisely determine the plasmon spectrum and damping.

Ion acoustic waves

Understanding the state and the evolution of planetary cores, brown dwarfs, and neutron star crusts requires accurate measurements of microscopic properties, such as viscosity and thermal conductivity, of the dense matter of which such systems are made. Due to the inherent difficulties in modeling strongly coupled plasmas, where classical long-range Coulomb forces dominate interactions between ions, current predictions of transport coefficients differ by many orders of magnitude. Here, LCLS-II-HE will deliver the photon flux to measure the ion collective modes, either electrostatic or acoustic waves [27, 28], that serve as an important tool to determine transport coefficient and to validate theoretical predictions. Until recently, only electron modes (plasmons) could be measured experimentally. LCLS-II-HE will provide X-rays with small enough bandwidth to allow the investigation of the low-frequency ion modes in dense matter as well. Recent experiments at LCLS have demonstrated proof-of-principle measurements of ion-acoustic waves, but less than five spectra could be measured with current repetition rates during one beam time. A thorough investigation of the warm dense matter phase space with high repetition rates will have profound consequences for the understanding of transport coefficients in dense plasmas. In particular, a strong diffusive mode around zero frequency has been predicted allowing novel measurements of friction.

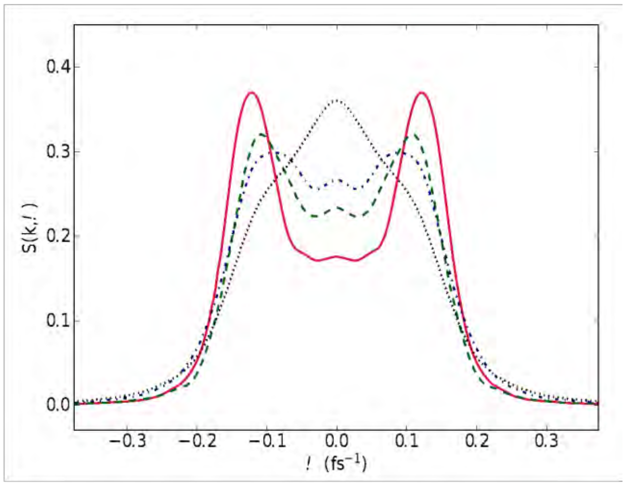

Figure 4.6.8. The sensitivity of the dynamic ion-ion structure factor to various friction parameters is shown. A value of 4x10^{13} s^{-1} results in two pronounced ion acoustic peaks (red curve) while 10^{14} s^{-1} provides a central peak (dashed black dotted curve). The sensitivity of the central peak indicates that LCS-II-HE will allow us, for the first time, to determine friction in the strongly coupled plasma state.

References

1. E. Wigner, and H. B. Huntington, "On the Possibility of a Metallic Modification of Hydrogen", *The Journal of Chemical Physics,* **3**, 764 (1935).
2. S. A. Bonev*, et al.*, "A quantum fluid of metallic hydrogen suggested by first-principles calculations", *Nature,* **431**, 669 (2004).
3. E. Babaev, A. Sudbo, and N. W. Ashcroft, "A superconductor to superfluid phase transition in liquid metallic hydrogen", *Nature,* **431**, 666 (2004).
4. R. T. Howie, P. Dalladay-Simpson, and E. Gregoryanz, "Raman spectroscopy of hot hydrogen above 200 GPa", *Nat Mater,* **14**, 495 (2015).
5. C. L. Guillaume*, et al.*, "Cold melting and solid structures of dense lithium", *Nat Phys,* **7**, 211 (2011).
6. P. Dalladay-Simpson, R. T. Howie, and E. Gregoryanz, "Evidence for a new phase of dense hydrogen above 325 gigapascals", *Nature,* **529**, 63 (2016).
7. V. Dzyabura, M. Zaghoo, and I. F. Silvera, "Evidence of a liquid–liquid phase transition in hot dense hydrogen", *PNAS,* **110**, 8040 (2013).
8. M. D. Knudson*, et al.*, "Direct observation of an abrupt insulator-to-metal transition in dense liquid deuterium", *Science,* **348**, 1455 (2015).
9. P. Loubeyre*, et al.*, "X-ray diffraction and equation of state of hydrogen at megabar pressures", *Nature,* **383**, 702 (1996).
10. Y. Akahama*, et al.*, "Evidence from x-ray diffraction of orientational ordering in phase III of solid hydrogen at pressures up to 183 GPa", *Phys. Rev. B,* **82**, 060101 (2010).
11. M. Zaghoo, A. Salamat, and I. F. Silvera, "Evidence of a first-order phase transition to metallic hydrogen", *Phys. Rev. B,* **93**, 155128 (2016).
12. M. A. Morales*, et al.*, "Evidence for a first-order liquid-liquid transition in high-pressure hydrogen from ab initio simulations", *PNAS,* **107**, 12799 (2010).
13. M. A. Morales*, et al.*, "Nuclear Quantum Effects and Nonlocal Exchange-Correlation Functionals Applied to Liquid Hydrogen at High Pressure", *Phys. Rev. Lett.,* **110**, 065702 (2013).
14. W. Lorenzen, B. Holst, and R. Redmer, "First-order liquid-liquid phase transition in dense hydrogen", *Phys. Rev. B,* **82**, 195107 (2010).
15. M. I. Eremets, and I. A. Troyan, "Conductive dense hydrogen", *Nat Mater,* **10**, 927 (2011).
16. C.-s. Zha*, et al.*, "High-Pressure Measurements of Hydrogen Phase IV Using Synchrotron Infrared Spectroscopy", *Phys. Rev. Lett.,* **110**, 217402 (2013).
17. C. J. Pickard, M. Martinez-Canales, and R. J. Needs, "Density functional theory study of phase IV of solid hydrogen", *Phys. Rev. B,* **85**, 214114 (2012).
18. Y. Meng*, et al.*, "New developments in laser-heated diamond anvil cell with in situ synchrotron x-ray diffraction at High Pressure Collaborative Access Team", *Rev. Sci. Instrum.,* **86**, 072201 (2015).
19. I. Kupenko*, et al.*, "Time differentiated nuclear resonance spectroscopy coupled with pulsed laser heating in diamond anvil cells", *Rev. Sci. Instrum.,* **86**, 114501 (2015).

20. W. J. Evans*, et al.*, "Dynamic diamond anvil cell (dDAC): A novel device for studying the dynamic-pressure properties of materials", *Rev. Sci. Instrum.,* **78**, 073904 (2007).
21. E. McBride*, et al.*, "Investigating Phase Transition Kinetics of Planetary Bodies: Plans for Using the Dynamic Diamond Anvil Cell at the European XFEL," in *Joint Workshop on High Pressure, Planetary and Plasma Physics*(DESY, 2013).
22. L. B. Fletcher*, et al.*, "Ultrabright X-ray laser scattering for dynamic warm dense matter physics", *Nat Photon,* **9**, 274 (2015).
23. C. E. Starrett, and D. Saumon, "Models of the elastic x-ray scattering feature for warm dense aluminum", *Phys. Rev. E,* **92**, 033101 (2015).
24. P. Sperling*, et al.*, "Free-Electron X-Ray Laser Measurements of Collisional-Damped Plasmons in Isochorically Heated Warm Dense Matter", *Phys. Rev. Lett.,* **115**, 115001 (2015).
25. J. P. Perdew, K. Burke, and M. Ernzerhof, "Generalized Gradient Approximation Made Simple", *Phys. Rev. Lett.,* **77**, 3865 (1996).
26. J. Heyd, G. E. Scuseria, and M. Ernzerhof, "Hybrid functionals based on a screened Coulomb potential", *The Journal of Chemical Physics,* **118**, 8207 (2003).
27. D. O. Gericke*, et al.*, "Screening of ionic cores in partially ionized plasmas within linear response", *Phys. Rev. E,* **81**, 065401 (2010).
28. H. R. Rüter, and R. Redmer, "*Ab Initio* Simulations for the Ion-Ion Structure Factor of Warm Dense Aluminum", *Phys. Rev. Lett.,* **112**, 145007 (2014).

4.7 Nonlinear Hard X-ray-Matter Interactions

With the advent of optical lasers in 1960, nonlinear optical interactions with matter became immediately accessible to a large number of researchers. Early fundamental studies involving parametric frequency conversion, phase-conjugation, stimulated Raman scattering, four-wave mixing and other phenomena have given rise to myriad applications, including coherent anti-Stokes Raman spectroscopy, multi-dimensional spectroscopy, attosecond pulse generation, and Nobel Prize-winning applications such as frequency comb metrology and super-resolution imaging. While spontaneous down conversion was observed in the 1970s using an X-ray tube, [1] X-ray nonlinearities that are multi-photon in the incident fields have remained elusive due to the vanishingly small susceptibilities at high frequencies and small intensities even from the brightest storage ring-based sources.

Almost fifty years after the first ruby laser, LCLS became the world's first hard X-ray laser. This represented a revolutionary 10^9-fold increase in the peak brightness of hard X-ray sources with focused intensities approaching the most intense optical sources. The peak X-ray brightness of LCLS is sufficient to saturate inner-shell cross-sections of all but the lightest atoms within a few femtoseconds and yield coherent X-ray scattering images with atomic-resolution from small crystals in so-called diffract-before-destroy mode. Nonetheless most experiments still rely on single photon interactions in the incident field. At high enough intensities, linear X-ray–matter interactions break down, even for non-resonant conditions. A few seminal experiments on the first generation of X-ray free-electron lasers, LCLS and SACLA, have demonstrated fundamental nonlinear X-ray–matter interactions at hard X-ray wavelengths including: coherent two-photon absorption [2], phase-matched sum frequency generation [3], second harmonic generation [4], and two-photon Compton scattering [5].

The combination of high repetition rate and high peak intensity pulses from LCLS-II-HE in the hard X-ray regime will allow us to transition from demonstration experiments to measurements of real-world systems that utilize the nonlinear interactions for photon-in/photon-out studies to simultaneously access transient atomic and electronic structural dynamics of materials. While nonlinear X-ray optics is still in the discovery-based science phase, advances in our understanding of these fundamental interactions will certainly lead to new tools for atomic and molecular physics, chemistry, materials science, and biology where the structure and dynamics of matter at the level of electrons and atoms is essential.

As described in the LCLS-II science opportunities document [6], the high repetition rate of LCLS-II will enable powerful new nonlinear, multidimensional, and coherent soft X-ray methods to capture rare chemical events, characterize fluctuating heterogeneous complexes, and reveal underlying quantum phenomena in matter. As a MHz X-ray laser, the soft X-rays of LCLS-II will open the entirely new fields of nonlinear X-ray science and multidimensional X-ray spectroscopy with the potential to map quantum coherences in an element specific way. For example, stimulated soft X-ray Raman scattering can be used to create and track valence electronic wavepackets that are initially localized on specific atoms.

New experimental methods exploiting nonlinear hard X-ray interactions will be complementary to those envisioned for the soft X-ray range, but will also be applicable in bulk materials and solution phase where softer X-rays cannot penetrate. In particular, they offer tremendous potential to reveal the dynamics of valence charge density (*i.e.* bonding electrons) in bulk materials with angstrom resolution on the attosecond to femtosecond time-scale of valence electron motion. Such methods to obtain simultaneous chemical and structural sensitivity in dense materials will be unique to LCLS-II-HE. For example, in the hard X-ray range, X-ray Raman scattering can provide similar chemical information to near-edge absorption spectroscopy, but for dense media, as described in Section 4.1. One challenge is that cross-sections for spontaneous X-ray Raman scattering are low. Stimulated processes have the potential to increase the signal by orders of magnitude. Even without the presence of gain, coherent spectroscopies such as four-wave mixing and Fourier transform multidimensional spectroscopy can provide a directed signal that can be effectively separated from the background. This is especially important for non-resonant nonlinear process. The combination of high peak power and high repetition rate is crucial for exploiting X-ray nonlinearities as this allows for control of the nonlinear interaction (*e.g.* moderation of peak intensity for interpretable results) while still maintaining detectable signal levels due to the high repetition rate.

4.7.1 Imaging optically induced charges

Non-resonant coherent X-ray scattering is sensitive to the spatial arrangement of charge density. Most X-ray scattering experiments to date at XFELs take advantage of the high temporal resolution to follow the nuclear dynamics (motion of core charge density) in materials. The capabilities of LCLS-II-HE will provide a dramatic advance for these applications across many areas of science (as outlined in Sections 4.1 through 4.6). However, while core charges are generally the dominant contribution to non-resonant X-ray scattering, the bonding forces of matter result from the valence electrons, and direct sensitivity to the fundamental motion of valence charges at the atomic scale will enable qualitative advances across broad areas of chemistry and materials science.

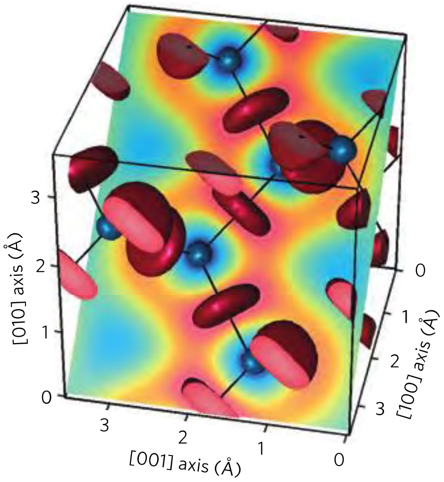

Figure 4.7.1. Atomic-scale optical response to XUV radiation of valence and core electrons in diamond measured with λ/380 resolution using the second-order nonlinear susceptibility for spontaneous parametric down conversion. A model consisting of two Lorenz oscillators was used to reconstruct the phase. In this case blue represents in-phase and red out-of phase (from reference 7).

Photon-based spectroscopies typically measure the instantaneous optical response of materials. This involves the motion of charges on the atomic scale, the microscopic details of which are largely unknown for wavelengths spanning the optical to soft-X-ray regime, even in the linear regime. Models based on the macroscopic dielectric response are insufficient for describing the local fields that vary on the atomic scale. In a recent pioneering experiment, Tamasaku and co-workers measured the local optical response of diamond (Figure 4.7.1) in the extreme ultraviolet spectral range by studying the spontaneous parametric down-conversion (PDC) of a 11.107 keV pump beam in diamond into a high energy signal photon and a low energy idler photon $\omega_I = \omega_p - \omega_s$ ranging from 60-120 eV [7]. The down-conversion process is weak, but can be enhanced by phase matching in a periodic solid with the help of a reciprocal lattice vector, $\vec{k}_p + \vec{G} = \vec{k}_s + \vec{k}_i$. By measuring the down-converted, but still high-energy signal photons as a function of offset from the Bragg condition for several sets of lattice planes, they were able to reconstruct the linear optical susceptibility due to the idler at energies below the C K-edge and above the

L-edge with resolution of up to λ/380 (Figure 4.7.1). In these experiments only the signal photon is measured, as the idler is strongly absorbed in the material.

This example illustrates one of the most compelling reasons for the development of hard X-ray nonlinear optics: the ability to probe the low energy optical response at the atomic scale in strongly absorbing materials. In this case, the idler response is encoded on the signal and can be inferred by measuring the energy loss. Because spontaneous PDC utilizes vacuum fluctuations, the experiments, while difficult, are nonetheless possible on storage rings. LCLS-II-HE will enable us to extend these studies to coherently driven systems including those far from equilibrium using stimulated X-ray-matter interactions.

This idea can be illustrated by considering a conceptually related experiment on X-ray sum-frequency generation (SFG). Here Glover *et al.*, measured the optical response in diamond to an applied electric field in the optical regime using SFG between an 8 keV probe and a 1.5eV pump [3] (Figure 4.7.2). The effect was first proposed by Eisenberger and McCall in 1971[8] and is bilinear in the applied fields potentially allowing for larger nonlinear response than all X-ray nonlinearities. In the Glover experiment the mixing signal between the applied optical and X-ray photons stimulates the SFG at 8.0015 keV under phase-matching conditions and is present only when the X-ray and optical beams overlap in both space and time.

Similar to PDC, the local polarization can be measured for different lattice planes (Fourier components) and in principle can be inverted to yield the spatial polarizability. However, unlike spontaneous PDC, where the idler can be emitted in many directions, the optical field is applied in a well-defined direction and in ultrashort pulses to achieve sufficient intensity to measure the stimulated effect. Even with the high brightness and ultrafast pulses of the LCLS, an efficiency of only 3×10^{-7} was observed for a 15 GW/cm^2 optical pulse, limiting the experiments to measure only the (111) component of the induced charge density at optical frequencies. The high average brightness of the LCLS-II-HE will allow much more detailed measurements, including the optical response from strongly driven and nonequilibrium systems as well as the equilibrium response in non-periodic systems – both for the first time.

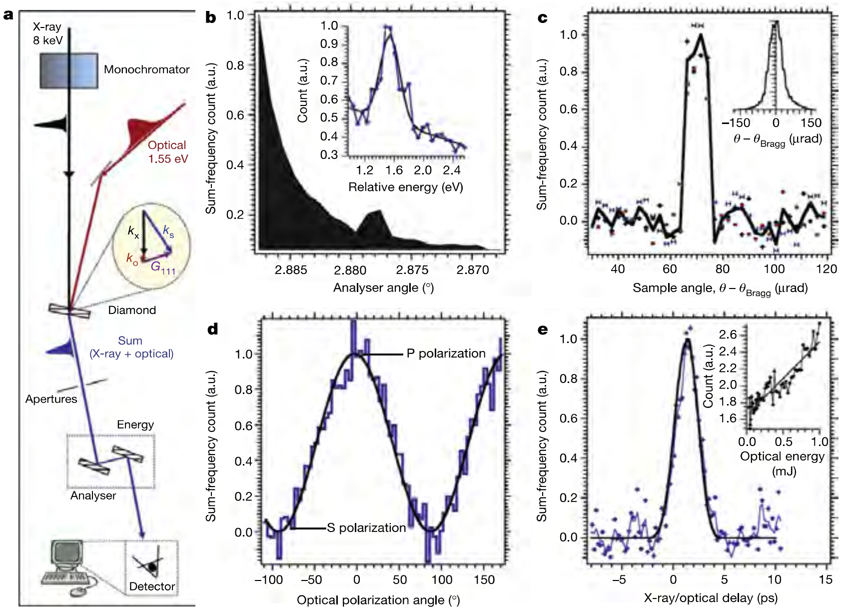

Figure 4.7.2. The first stimulated X-ray and optical mixing experiment was performed using 8 keV X-ray and 1.5 eV optical laser beams in a single crystal diamond sample [3].

4.7.2 Multi-photon Compton scattering

Whereas coherent scattering is used to measure charge density and thus atomic structure, Compton scattering measures the electron momentum distribution of the loosely bound valence and conduction electrons in materials. It is essentially spontaneous X-ray Raman scattering where the final state involves a free electron. In the limit that the energy loss is large compared to the binding energy (impulse-approximation), the initial-state electrons look quasi-free and the scattering occurs as if the emitted electron had an initial energy corresponding to a free electron with the same momentum.

The usefulness of Compton scattering as a spectroscopic probe has been limited by the need for very high brightness and high resolution to measure subtle differences – for example, to recover subtleties in the electronic band-structure [9]. However, it is still widely used as a plasma diagnostic for matter in extreme conditions [10] (where it is typically referred to as Thomson scattering). It is even exploited in the hard X-ray beamline intensity and position monitors at LCLS and other XFELs.

Compton scattering is typically thought of as an incoherent process and an unwanted (and nearly structureless) background in crystallography. As the photon energy increases, more of the inner-shell electrons become accessible to Compton scattering, the elastic cross-section is reduced, and energy is more efficiently transferred to the electronic system. The unique properties of LCLS-II-HE and their relevance for high resolution inelastic X-ray scattering will likely drive a resurgence in the measurement of high resolution Compton profiles. This could open up this method for time-domain studies of nonequilibrium momentum distributions, including through the use of X-ray Fourier transform techniques [11].

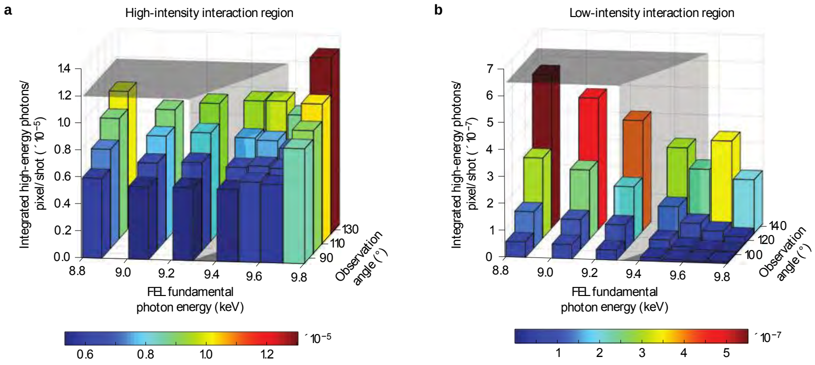

Figure 4.7.3. Measured two-photon Compton scattering in Be in comparison with the linear Compton scattering from the FEL second harmonic (from reference 5).

Recently, Fuchs *et al.*, measured for the first time the simultaneous scattering of two X-ray photons from a single electron in a bulk Be target [5] at hard X-ray wavelengths well above the binding energy for a 1*s* electron in Be. From the point of view of the nonlinear X-ray scattering, the expectation was that the target would look like an initially cold free-electron plasma in the impulse approximation. Multiphoton Compton scattering from a free-electron is a fundamental process in QED [12] and had been previously observed in the collision of a TW optical laser with the 50 GeV electron beam at SLAC [13], where in the center of momentum frame the intensity approached the QED critical value.

While the X-ray intensity in the Fuchs experiment (~10^{20} W/cm^2) is orders of magnitude above the atomic limit, it is nevertheless well below the QED limit. In this regime, the process is expected to be perturbative. As expected for a second-order nonlinear interaction, the nonlinear scattered radiation followed a quadratic dependence on intensity. However, the angular distribution and spectrum deviated from that predicted based on the impulse approximation. Figure 4.7.3 shows the measured X-ray flux around 18 keV as a function of both angle and incident X-ray energy for both the nonlinear Compton signal and linear Compton background of the second harmonic. The authors measured an anomalous redshift in the nonlinear signal of hundreds of eV, which they argue is due to an enhanced sensitivity of two-photon Compton scattering from bound electrons and a new scattering mechanism involving both photoionization and scattering matrix elements.

If correct, this new observation indicates that nonlinear Compton scattering is sensitive to the bound electronic structure in a way that linear Compton scattering is not. It would therefore allow combined electron momentum measurements with atomic specificity. This is the natural extension of the results of the previous sections to dynamic processes, where it is important to know not only where the charges are, but also how they are moving. It would further allow for instantaneous probes of plasma dynamics in MEC conditions (see Section 4.6). LCLS-II-HE will allow for precision measurements of both the linear and nonlinear X-ray form factors, especially in atomic and molecular systems where the high repetition rate is essential to overcome the low density. This will further enable a complete reconstruction of the scattering events by coincidence measurements of the emitted electron and the recoiled ion and emitted photon.

References

1. P. Eisenberger, and S. L. McCall, "X-Ray parametric conversion", *Phys. Rev. Lett.,* **26**, 684 (1971).
2. K. Tamasaku*, et al.*, "X-ray two-photon absorption competing against single and sequential multiphoton processes", *Nat Photon,* **8**, 313 (2014).
3. T. E. Glover*, et al.*, "X-ray and optical wave mixing", *Nature,* **488**, 603 (2012).
4. S. Shwartz*, et al.*, "X-Ray Second Harmonic Generation", *Phys. Rev. Lett.,* **112**, 163901 (2014).
5. M. Fuchs*, et al.*, "Anomalous nonlinear X-ray Compton scattering", *Nat Phys,* **11**, 964 (2015).
6. New Science Opportunities enabled by LCLS-II X-ray Lasers, SLAC-R-1053 https://portal.slac.stanford.edu/sites/lcls_public/Documents/LCLS-IIScienceOpportunities_final.pdf
7. K. Tamasaku*, et al.*, "Visualizing the local optical response to extreme-ultraviolet radiation with a resolution of λ/380", *Nat Phys,* **7**, 705 (2011).
8. P. M. Eisenberger, and S. L. McCall, "Mixing of x-ray and optical photons", *Phys. Rev. A,* **3**, 1145 (1971).
9. K. Hämäläinen*, et al.*, "High resolution Compton scattering study of Be", *Phys. Rev. B,* **54**, 5453 (1996).
10. S. H. Glenzer, and R. Redmer, "X-ray Thomson scattering in high energy density plasmas", *Reviews of Modern Physics,* **81**, 1625 (2009).
11. M. Trigo*, et al.*, "Fourier-transform inelastic X-ray scattering from time- and momentum-dependent phonon-phonon correlations", *Nat Phys,* **9**, 790 (2013).
12. L. S. Brown, and T. W. B. Kibble, "Interaction of Intense Laser Beams with Electrons", *Physical Review,* **133**, A705 (1964).
13. C. Bula*, et al.*, "Observation of nonlinear effects in compton scattering", *Phys. Rev. Lett.,* **76**, 3116 (1996).

Appendix 1: Key performance parameters and operating modes

Key performance parameters

The Key Performance Parameters (KPPs), both “Threshold” and “Objective” levels, for the LCLS-II-HE project are listed in Table 1.

Table 1: Key Performance Parameters (KPPs) for the LCLS-II-HE upgrade.

Performance Measure	**Threshold**	**Objective**
Superconducting linac electron energy	7 GeV	≥ 8 GeV
Electron bunch repetition rate in linac	93 kHz	929 kHz
Charge per bunch in SC- linac	0.02 nC	≥ 0.1 nC
Photon energy range	8000 eV	250 to ≥ 12800 eV
High rep-rate-capable HXR end stations	≥ 2	≥ 5
FEL photon quantity (10^{-3} BW)	1×10^{7} (10× spont. @ 8 keV)	> 10^{11} @ 8 keV (200 μJ), > 10^{10} @ 12.8 keV (20 μJ)

Operating modes

LCLS-II-HE will incorporate a new 3.6-GeV bypass line with a kicker magnet at the end of the L3-linac section (see Figure 6.1). This long beam line (~2.4 km) terminates into a DC bend magnet just upstream of the SXR undulator (see gray-dashed line in Figure 6.1). This configuration allows at least six simultaneous running modes as described in Table 2, where the HXR can be run simultaneously with the SXR. The SXR is also connected to the 120-Hz Cu-linac through another kicker-based short beamline, allowing many simultaneously operating modes, choices of electron energy, and options for bunch repetition rate in the two XFELs.

Table 2: Simultaneous operating modes for the two XFELs and three electron lines. After choosing one of the three SXR modes (left column), the user then selects one of two HXR modes at right (SC-Linac or Cu-linac options). X-rays performance is quantified in terms of energy per pulse when operating at 120 Hz, and average X-ray power when operating at high repetition rate.

SXR-FEL Choice	**HXR-FEL, SC-Linac Option**	**or**	**HXR-FEL, Cu-Linac Option**
3 - 3.6 GeV **SC-Linac** (< 1 MHz) 0.1-1.3 keV with >> 20 W	3.3 - 8 GeV **SC-linac** (< 1 MHz) 1-13 keV with >20 W	or	3 - 15 GeV **Cu-Linac** (≤ 120Hz) 1-25 keV with mJ pulses
3.3 - 8 GeV **SC-Linac** (< 1 MHz) 0.2-5 keV with >> 20 W	3.3 - 8 GeV (sync’d to SXR) **SC-Linac** (< 1 MHz) 1-13 keV with >20 W	or	3 - 15 GeV **Cu-Linac** (≤ 120Hz) 1-25 keV with mJ pulses
3 - 10 GeV **Cu-Linac** (≤ 120Hz) 0.1-16 keV with mJ pulses	3.3 - 8 GeV **SC-Linac** (< 1 MHz) 1-13 keV with >20 W	or	3 - 15 GeV (sync’d to SXR) **Cu-Linac** (≤ 120Hz) 1-25 keV with mJ pulses

Appendix 2: Workshops

LCLS-II New Instruments Workshop

March 19-22, 2012 SLAC National Accelerator Laboratory

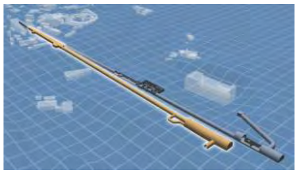

Report: SLAC-R-93

The goal of the original LCLS-II workshop was to identify the most exciting science and corresponding parameters which to help define the LCLS-II instrumentation. Scientists from around the world provided short descriptions of the scientific opportunities they envisioned at LCLS-II. The workshops focused on four broadly defined science areas: biology, materials sciences, chemistry and atomic, molecular and optical physics (AMO).

LCLS-II Scientific Opportunities Workshops

February 9-13, 2015 SLAC National Accelerator Laboratory

The LCLS-II Scientific Opportunities Workshop series was organized to advance the scientific opportunities of this new facility, and refine the technical requirements to ensure maximum impact during early operations and into the future. The series comprised four sequential meetings focused on: Materials Physics, Life Sciences, Chemistry, and Materials in Extreme Conditions. More than 400 participants from around the world attended these workshops and contributed to the workshop report. The results of these workshops feed directly in to the science strategy for LCLS; to help guide the design, commissioning and ultimate operation of the upgraded facility; and further inform the R&D roadmap for instrumentation and machine performance.

Report: SLAC-R-1053

Research Opportunities in Photochemistry, Solar Energy & Advanced X-ray Methods

June 16-17, 2016 SLAC National Accelerator Laboratory

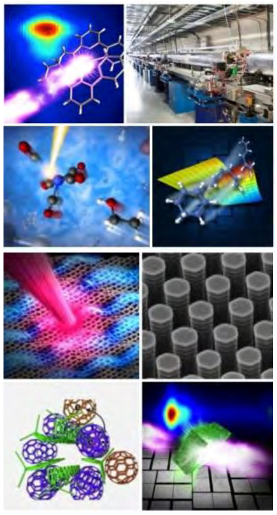

This workshop was jointly organized by LCLS and SSRL and focused on fundamental questions in solar energy conversion and opportunities where advanced X-ray methods will have a significant impact. The workshop goals were to: (i) facilitate the exchange of ideas and foster collaborations between scientists focused on solar energy conversion and researchers with expertise in time-resolved X-ray science, (ii) identify challenges and opportunities for time-resolved X-ray methods for addressing problems in basic energy science, and (iii) propose development paths for the most compelling science areas. More than 140 participants attended, and there were three breakout sessions on:

1. Nano- and solid state materials for solar energy conversion
2. Molecular materials for solar energy conversion
3. Fundamental chemistry and physics of light driven phenomena

XFELO Science Workshop

June 29-July 1, 2016   SLAC National Accelerator Laboratory

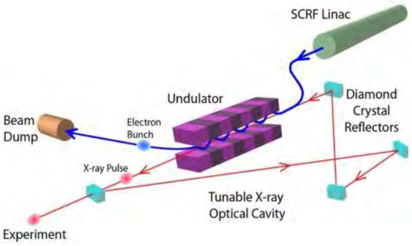

This workshop comprised two and half days of in-depth discussion from international participants of various scientific opportunities that might be uniquely enabled by an XFEL oscillator (XFELO).

High-gain free electron lasers at the LCLS at SLAC and other laboratories around the world have demonstrated the power of FELs for X-rays. An oscillator-type FEL is also feasible for the hard X-ray spectral region producing fully coherent, intense X-ray pulses of high spectral purity with MHz repetition rate. It appears that an XFELO is within the reach of current technology and, furthermore, the 4 GeV CW-SCRF linac under construction for the LCLS-II is a suitable driver a practical XFELO.

Scientific Opportunities for Ultrafast Hard X-rays at High Repetition Rate: An Energy Upgrade of LCLS-II

September 26-27, 2016   SLAC National Accelerator Laboratory

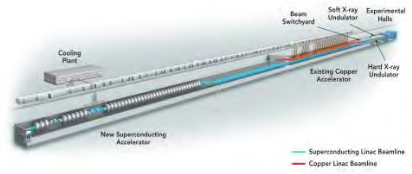

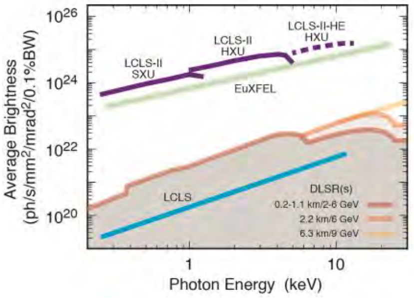

The proposed energy upgrade of LCLS-II to 8 GeV (LCLS-II-HE) promises to open entirely new areas of science by providing X-ray energies extending beyond 12 keV to enable high repetition-rate studies of atomic, electronic, and chemical dynamics at the atomic scale.

The objective of this workshop is to further develop the science case for this proposed upgrade, and refine the technical requirements to ensure maximum scientific impact. The results of this workshop will will help guide the design and performance capabilities of the upgraded facility; and will inform the planning for new future scientific instrumentation.

Appendix 3: RIXS/IXS comparison and sample considerations

Table 1 shows a comparison of the projected performance for IXS and RIXS at LCLS-II-HE versus existing instruments at synchrotron facilities.

Table 1. Comparison of projected LCLS-II-HE performance for RIXS and IXS (based on data in reference 1).

	Hard X-ray Flux on Sample		
Resolution	~100 meV	**10 meV**	**~1 meV**
LCLS-II-HE (seeded)		**~10^{14} ph/s**	**~10^{13} ph/s**
LCLS-II-HE (SASE)		**~10^{13} ph/s**	**~10^{12} ph/s**
ESRF	~10^{13} ph/s (UPBL6)	~10^{11} ph/s (ID28)	~10^{10} ph/s (ID28)
SPring-8		~10^{12} ph/s	~10^{10} ph/s
APS	~10^{12} ph/s (MERIX)	~10^{11} ph/s	~10^{10} ph/s ~10^{9} ph/s (UHRIXS)
NSLS-II			~10^{10} ph/s

Consideration of limitations on usable X-ray flux

The tolerable X-ray flux on a sample may be limited by detrimental effects such as nonlinear X-ray interactions and sample heating. In the case of the former, such limits may be estimated by consideration of the atomic absorption cross-section: ~10^{-19} cm^2 (*e.g.* at the Fe K-edge). Nonlinear effects are expected to become important at energy densities exceeding ~0.1 eV/atom, which corresponds to ~10^{14} ph/cm^2 at 10 keV (~160 mJ/cm^2). This is consistent recent with observations of nonlinear effects in the soft X-ray range, accounting for the differences in absorption cross-section: $\sigma_{\text{soft X-ray}} \sim 100\sigma_{\text{hard X-ray}}$. This corresponds to ~$10^9$ ph/pulse in a focus of 10 μm × 100 μm, or ~10^{14} ph/s at 100 kHz (or an average power on sample of ~160 mW).

Further consideration must of course be given to sample heating and long-term survival, which can impose strict limits on the average power that can be used. The highest powers of LCLS-II-HE will be readily useable for flowing liquid or gas based samples in which the excitation volume is replaced between X-ray pulses. For solid-state samples, the uniform pulse spacing provides enhanced experimental utility compared to the pulsed European XFEL source through the use of pulse-to-pulse sample replacement, recovery and rastering techniques. For more delicate samples, this uniform pulse spacing also allows ~30x lower peak power per pulse than the European XFEL for the same average power (due to the latter's burst mode at an effective rate of 28 kHz).

Figure 1 and Table 2 present estimates of average sample heating effects for an incident X-ray flux of ~10^{13} ph/s at 11 keV (~20 mW average power or 10^8 ph/pulse at 100 kHz). For a 100 μm thick sample with a thermal conductivity of 20 W/K•m a surface temperature rise of only 2.6 K is predicted. This illustrates the potential to exploit the full capability of LCLS-II-HE (*e.g.* 1 meV resolution with ~10^{13} ph/s on the sample) – depending of course on the details of the particular sample and experimental geometry.

As indicated in Table 1, even clamping the average X-ray flux to levels currently used in synchrotron studies will permit up to a 100-fold increase in energy resolution (or, conversely, a 100-fold to 1,000-fold increase in flux for the highest resolution studies).

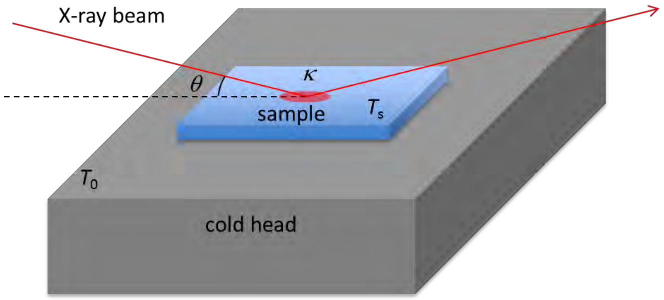

Figure 1. Sample illumination geometry.

Table 2. Predicted change in sample surface temperature due to average X-ray heating for the geometry shown in Figure 1. Absorption cross-section for Sr_2IrO_2 is assumed, with incident X-rays at the Ir L_3-edge (11.18 keV).

Average beam power	**20**	**20**	**mW**
X-ray beam incidence angle (θ)	20	20	deg.
X-ray beam size (vert.×horiz.)	20×500	20×500	μm
Sample thickness	10	100	μm
Sample size (vert.×horiz.)	1×1	1×1	mm^2
Sample thermal conductivity	20	20	W/K•m
Cold-head base temperature	100	100	K
Sample Surface Temperature Excursion ΔT	**0.06**	**2.6**	**K**

References

1. A. Q. R. Baron, "High-Resolution Inelastic X-Ray Scattering II: Scattering Theory, Harmonic Phonons, and Calculations," in *Synchrotron Light Sources and Free-Electron Lasers: Accelerator Physics, Instrumentation and Science Applications*, E. Jaeschke, S. Khan, J. R. Schneider, and J. B. Hastings, eds. (Springer International Publishing, Cham, 2014), pp. 1.